# TIME-RESOLVED CHARACTERIZATION OF THERMAL AND FLOW DYNAMICS DURING MICROCHANNEL FLOW BOILING

by

**Todd A. Kingston**

**A Dissertation**

*Submitted to the Faculty of Purdue University*

*In Partial Fulfillment of the Requirements for the degree of*

**Doctor of Philosophy**
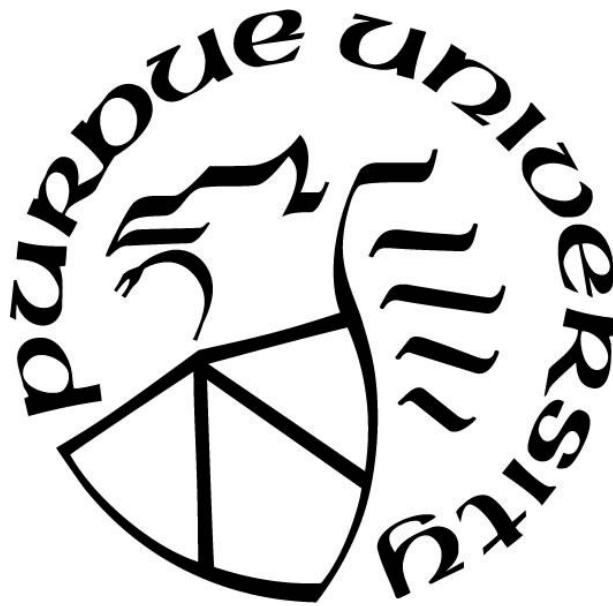


School of Mechanical Engineering

West Lafayette, Indiana

May 2019

# THE PURDUE UNIVERSITY GRADUATE SCHOOL
# STATEMENT OF COMMITTEE APPROVAL

Dr. Suresh V. Garimella, Co-Chair

School of Mechanical Engineering

Dr. Justin A. Weibel, Co-Chair

School of Mechanical Engineering

Dr. Xiulin Ruan

School of Mechanical Engineering

Dr. Steven H. Collicott

School of Aeronautics and Astronautics

**Approved by:**

Dr. Jay P. Gore

Head of the Graduate Program

*To Jessica and Landrie*

# ACKNOWLEDGMENTS

I want to first thank my advisors, Prof. Suresh Garimella and Prof. Justin Weibel, for their mentorship throughout my graduate studies at Purdue University. Their guidance has been invaluable to my education and professional development. I am truly grateful to have had the opportunity to learn from them both.

I want to thank Dr. Brian Olson from Naval Surface Warfare Center Crane Division (NSWC Crane) for his collaboration and technical advice on our project funded by the Naval Engineering Education Consortium (NEEC). I also want to thank Dr. Olson and Mr. Charles Walker for allowing me to intern in the Solid State and Power Engineering Branch at NSWC Crane. It was a wonderful experience and greatly benefited my professional career.

I want to thank Prof. Xiulin Ruan and Prof. Steven Collicott for serving on my advisory committee.

Thank you to my labmates, past and present, whose friendship and help were invaluable over the years. Special thanks to Dr. Kevin Drummond, Prof. Matthew Rau, and Prof. Zhenhai Pan.

A special thanks to Jessica, Landrie, and the rest of my family and friends for their love and support.

# TABLE OF CONTENTS

# LIST OF TABLES

# LIST OF FIGURES

# NOMENCLATURE

| | |
|---|---|
| $A_s$ | inside surface area of the microchannel |
| Bo | Bond number, $(\rho_l - \rho_v)gD^2/\sigma_l$ |
| $c_p$ | specific heat |
| $D$ | microchannel inside diameter |
| $D_b$ | vapor bubble diameter |
| $f$ | characteristic oscillation frequency |
| $g$ | gravitational acceleration constant |
| $G$ | mass flux |
| $G_{1\phi}$ | nominal single-phase mass flux |
| $\Delta\widetilde{G}_{osc,amp}$ | mass flux oscillation amplitude |
| $h$ | heat transfer coefficient |
| $h_{fg}$ | heat of vaporization |
| $k$ | thermal conductivity |
| $\Delta p$ | pressure drop across the microchannel |
| $p_{in}$ | inlet pressure |
| $\Delta\widetilde{p}_{osc,amp}$ | pressure drop oscillation amplitude |
| $p_{out}$ | outlet pressure |
| $p_{sat}$ | saturation pressure of the fluid |
| $P$ | total power |
| $P_{in}$ | power into the microchannel |
| $P_{loss}$ | power loss to ambient |
| $P_{total}$ | total power applied |
| $L$ | microchannel length |
| $L_b$ | vapor bubble length |
| $L_{heated}$ | microchannel heated length |
| $L_s$ | liquid slug length |
| $L_0$ | initial vapor bubble/liquid slug length |
| $Re_D$ | Reynolds number, $V_b D/v_l$ |
| $t$ | time |
| $t_w$ | microchannel wall thickness |
| $T$ | temperature |
| $T_{in}$ | inlet fluid temperature |
| $\widetilde{T}_{osc,amp}$ | wall temperature oscillation amplitude |
| $T_{out}$ | outlet fluid temperature |
| $T_{ref}$ | reference temperature |
| $T_{sat}$ | fluid saturation temperature |
| $T_{sat,out}$ | fluid saturation temperature corresponding to outlet pressure |

| | |
|---|---|
| $\Delta T_{sub}$ | inlet liquid subcooling relative to outlet saturation temperature |
| $T_{wall}$ | microchannel outside wall temperature |
| $\Delta T_{wall,sup}$ | wall superheat relative to reference temperature |
| $V$ | voltage |
| $V_b$ | vapor bubble velocity |
| $I$ | electric current |
| $Q$ | volumetric flow rate |
| $q_{in}$ | net heat flux into the microchannel |
| $x$ | transverse position relative to microchannel centerline |
| $y$ | axial position relative to T-junction center |
| $y'$ | axial position relative to camera field of view |
| $z$ | vertical position relative to microchannel centerline |

*Greek Letters*

| | |
|---|---|
| $\delta$ | liquid film thickness |
| $\theta$ | angle between normal and incident/refracted light |
| $\mu$ | dynamic viscosity |
| $v_l$ | liquid kinematic viscosity |
| $\rho$ | density |
| $\rho_l$ | liquid density |
| $\rho_v$ | vapor density |
| $\sigma$ | surface tension |
| $\sigma_l$ | liquid surface tension |

*Subscripts*

| | |
|---|---|
| *5* | $5^{th}$ percentile |
| *95* | $95^{th}$ percentile |
| *avg* | time-averaged |
| *in* | inlet |
| *out* | outlet |

# ABSTRACT

Author:  Kingston, Todd A., Ph.D.
Institution:  Purdue University
Degree Received:  May 2019
Title:  Time-Resolved Characterization of Thermal and Flow Dynamics During Microchannel Flow Boiling
Major Professors:  Suresh V. Garimella and Justin A. Weibel

The continued miniaturization and demand for improved performance of electronic devices has resulted in the need for transformative thermal management strategies.  Flow boiling is an attractive approach for the thermal management of devices generating high heat fluxes. However, designing heat sinks for two-phase operation and predicting their performance is difficult because of, in part, commonly encountered flow boiling instabilities and a lack of experimentally validated physics-based phase change models.  This work aims to advance the state of the art by furthering our understanding of flow boiling instabilities and their implications on the operating characteristics of electronic devices.  This is of particular interest under transient and non-uniform heating conditions because of recent advancements in embedded cooling techniques, which exacerbate spatial non-uniformities, and the demand for cooling solutions for next-generation electronic devices.  Additionally, this work aims to provide a high-fidelity experimental characterization technique for slug flow boiling to enable the validation of physics-based phase change models.

To provide a foundation for which the effects of transient and non-uniform heating can be studied, flow boiling instabilities are first studied experimentally in a single, 500 μm-diameter borosilicate glass microchannel.  A thin layer of optically transparent and electrically conductive indium tin oxide coated on the outside surface of the microchannel provides a spatially uniform and temporally constant heat flux via Joule heating. The working fluid is degassed, dielectric

HFE-7100. Simultaneous high-frequency measurement of reservoir, inlet, and outlet pressures, pressure drop, mass flux, inlet and outlet fluid temperatures, and wall temperature is synchronized to high-speed flow visualizations enabling transient characterization of the thermal-fluidic behavior.

The effect of flow inertia and inlet liquid subcooling on the rapid-bubble-growth instability at the onset of boiling is assessed first. The mechanisms underlying the rapid-bubble-growth instability, namely, a large liquid superheat and a large pressure spike, are quantified. This instability is shown to cause flow reversal and can result in large temperature spikes due to starving the heated channel of liquid, which is especially severe at low flow inertia.

Next, the effect of flow inertia, inlet liquid subcooling, and heat flux on the hydrodynamic and thermal oscillations and time-averaged performance is assessed. Two predominant dynamic instabilities are observed: a time-periodic series of rapid-bubble-growth instabilities and the pressure drop instability. The heat flux, ratio of flow inertia to upstream compressibility, and degree of inlet liquid subcooling significantly affect the thermal-fluidic characteristics. High inlet liquid subcoolings and low heat fluxes result in time-periodic transitions between single-phase flow and flow boiling that cause large-amplitude wall temperature oscillations and a time-periodic series of rapid-bubble-growth instabilities. Low inlet liquid subcoolings result in small-amplitude thermal-fluidic oscillations and the pressure drop instability. Low flow inertia exacerbates the pressure drop instability and results in large-amplitude thermal-fluidic oscillations whereas high flow inertia reduces their severity.

Flow boiling experiments are then performed in a parallel channel test section consisting of two thermally isolated, heated microchannels to study the Ledinegg instability. When the flow in both channels is in the single-phase regime, they have equal wall temperatures due to

evenly distributed mass flux delivered to each channel. Boiling incipience in one of the channels triggers the Ledinegg instability which induces a temperature difference between the two channels due to flow maldistribution. The temperature difference between the two channels grows with increasing power. The experimentally observed temperature excursion between the channels due to the Ledinegg instability is reported here for the first time.

Time-resolved characterization of flow boiling in a single microchannel is then performed during transient heating conditions. For transient heating tests, three different heat flux levels are selected that exhibit highly contrasting flow behavior during constant heating conditions: a low heat flux corresponding to single-phase flow ($15 \, \text{kW/m}^2$), an intermediate heat flux corresponding to continuous flow boiling ($75 \, \text{kW/m}^2$), and a very high heat flux which would cause critical heat flux if operated at this heat flux continuously ($150 \, \text{kW/m}^2$). Transient testing is first conducted using a single heat flux pulse between these heat flux levels and varying the pulse time. It is observed that any step up/down in the heat flux level that induces/ceases boiling, causes the temperature to temporarily over/under-shoot the eventual steady temperature. Following the single heat flux pulse experiments, a time-periodic series of heat flux pulses is applied. A square wave heating profile is used with pulse frequencies ranging from 0.1 to 100 Hz and three different heat fluxes levels (15, 75, and $150 \, \text{kW/m}^2$). Three different time-periodic flow boiling fluctuations are observed: flow regime transitions, pressure drop oscillations, and heating pulse propagation. For heating pulse frequencies between approximately 1 and 10 Hz, the thermal and flow fluctuations are heavily coupled to the heating characteristics, forcing the pressure drop instability frequency to match the heating frequency. For heating pulse frequencies above 25 Hz, the microchannel wall attenuates the transient heating profile and the fluid essentially experiences a constant heat flux.

To improve our ability to predict the performance of heat sinks for two-phase operation, high-fidelity characterization of key hydrodynamic and heat transfer parameters during microchannel slug flow boiling is performed using a novel experimental test facility that generates an archetypal flow regime, devoid of flow instabilities and flow regime transitions. High-speed flow visualization images are analyzed to quantify the uniformity of the vapor bubbles and liquid slugs generated, as well as the growth of vapor bubbles over a range of heat fluxes. A method is demonstrated for measuring liquid film thickness from the visualizations using a ray-tracing procedure to correct for optical distortions. Characterization of the slug flow boiling regime that is generated demonstrates the unique ability of the facility to precisely control and quantify hydrodynamic and heat transfer characteristics.

This work has advanced state-of-the-art technologies for the thermal management of high-heat-flux-dissipation devices by providing an improved understanding on the effects of transient and non-uniform heating on flow boiling and an experimental method for the validation of physics-based flow boiling modeling.

# 1  INTRODUCTION

## 1.1  Background

The continued miniaturization and demand for improved performance of electronic devices has resulted in the need for transformative thermal management strategies.  While conventional cooling strategies (*e.g.*, active air cooling) have served well in the past, a straightforward extension is no longer possible [1], and next-generation cooling strategies capable of dissipating high heat fluxes need to be developed [1-4].

One approach to enabling higher heat flux dissipation is to replace conventional flow passages with microscale flow passages (*i.e.*, microchannels).  In 1981, Tuckerman and Pease [5] pioneered the use of high-aspect-ratio microchannels to dissipate heat fluxes up to 790 W/cm$^2$ using single-phase water flow.  The small channel dimensions and high surface area-to-volume ratios found in microchannel heat sinks aid in heat transfer.  This work sparked a surge in the study of microscale cooling for decades with the goal of maximizing the heat flux dissipation capabilities while minimizing the pumping power requirements and improving the predictive capabilities.  Today, single-phase flow can be accurately predicted using available modeling tools, making evaluation of heat sink designs straightforward when operated under single-phase flow conditions.  However, single-phase liquid cooling inherently suffers from relatively large increases in coolant temperature across the flow length and relies on large pumping powers, particularly when flowing through small channels.

Two-phase cooling strategies, which allow liquid coolant to boil during the heat removal processes, overcome these limitations by enabling lower pumping power at a given heat removal rate and feature relatively uniform coolant temperatures due to the isothermal phase change

process. Moreover, two-phase cooling strategies, in general, feature higher heat transfer coefficients than single-phase cooling strategies [6]. Microchannel flow boiling is one promising two-phase cooling strategy. However, designing heat sinks for two-phase operation and predicting their performance is difficult, in part because of (i) commonly encountered flow boiling instabilities, (ii) the reliance on empirical-based flow boiling correlations, (iii) the lack of validated physics-based phase change models, (iv) the need to reliably integrate liquid cooling into electronic devices, (v) the lack of accurate critical heat flux prediction tools, and (vi) robust thermal packaging solutions that minimize thermomechanical stresses, to name a few.

## 1.2    Goal and Objective

The overall goal of this work is to advance the state of the art of microchannel flow boiling technologies for the thermal management of electronic devices requiring high-heat-flux dissipation. This goal will be realized by furthering the understanding of flow boiling instabilities and their implications on the operating characteristics of electronics devices. Emphasis will be placed on the behavior of these instabilities when the flow boiling system is subjected to transient and non-uniform heating conditions, due to the recent advancements in embedded cooling techniques and the need to cool time-dependent electronic components. Additionally, the ability to predict the performance of heat sinks operating under flow boiling conditions will be advanced by the development of an experimental technique to provide high-fidelity characterization of slug flow boiling to enable the validation of physics-based phase change models.

## 1.3    Objectives

The first objective of this work is to investigate the effect of flow inertia and inlet liquid subcooling on the rapid-bubble-growth instability at the onset of boiling.  The mechanisms underlying the rapid-bubble-growth instability, namely, a large liquid superheat and a large pressure spike, are also quantified using simultaneous high-frequency measurement of the thermal-fluidic signatures synchronized to high-speed flow visualizations.  Next, the impact of operating conditions on the instability type and the resulting time-periodic hydrodynamic and thermal oscillations is investigated.  These oscillations, which occur after the initial boiling incipience event, are assessed under spatially uniform and temporally steady heating conditions and set the framework for future studies which incorporate transient and non-uniform heating. The effect of flow inertia, inlet liquid subcooling, and heat flux on the hydrodynamic and thermal oscillations and time-averaged performance is assessed.  A spectral analysis of the time-periodic data is performed to determine the characteristic oscillation frequencies.

Having studied flow instabilities in a single-channel configuration, the next objective is to study instabilities that arise in parallel channel systems, such as the Ledinegg (flow excursion) instability and the parallel channel instability.  The previously used single-channel test section is replaced by two thermally isolated, hydrodynamically coupled parallel microchannels.  Time-resolved thermal-fluid measurements enable the parallel channel instability to be assessed while time-averaged data quantifies the effects of the Ledinegg instability.

All prior investigations of flow boiling instabilities in this work have been under constant heating conditions.  The next objective is to assess the impact of transient heating conditions on heat transfer performance and flow boiling instabilities.  The single-channel test section is subjected to a time-varying heat flux boundary condition.  Time-resolved thermal-fluid

measurements are again be used to assess the dominant heat transfer mechanisms and identify the effects of different heat flux levels and pulse durations and frequencies.

The final objective is to provide high-fidelity characterization of key hydrodynamic and heat transfer parameters during microchannel slug flow boiling. This is accomplished using a novel experimental test facility that generates an archetypal slug flow regime by independently injecting vapor and liquid phases of the dielectric fluid HFE-7100 T-junction to create a saturated two-phase slug flow, thereby eliminating the flow instabilities and flow-regime transitions that would otherwise result from stochastic generation of vapor bubbles. High-speed flow visualization images are analyzed to quantify the uniformity of the vapor bubbles and liquid slugs generated, as well as the growth of vapor bubbles under a range of heat fluxes. A method is also demonstrated for measuring liquid film thickness from the visualizations using a ray-tracing procedure to correct for optical distortions.

## 1.4    Document Organization

The work presented in this preliminary thesis is organized into nine chapters.  Chapter 1 provides an introduction and motivation for the current study, and outlines the goal and objectives of the work.  Chapter 2 reviews the relevant literature.  Chapters 3 and 4 present an experimental investigation of dynamic microchannel flow boiling instabilities in a single channel, with Chapter 3 focusing on the rapid-bubble-growth instability at the onset of boiling and Chapter 4 focusing on the impact of operating conditions on instability type and severity. Chapter 5 illustrates the impact of Ledinegg-instability induced thermal excursions in parallel, heated channels.  Chapters 6 and 7 demonstrate the effects of transient heating conditions on heat transfer performance and flow boiling instabilities, with Chapter 6 focusing on the dynamic response to a single heat flux pulse and Chapter 7 focusing on the dynamic response to a time-periodic series of heat flux pulses.  Chapter 8 presents the development of an experimental method for controlled generation and characterization of microchannel slug flow boiling. Finally, Chapter 9 discusses important conclusions from this work and proposes future investigations.

# 2   LITERATURE REVIEW

Two-phase flows are commonly encountered in nuclear, power generation, petroleum, and other industries.  In general, two-phase flows can be classified according to whether phase change is occurring, which leads to strong differences in the underlying physics.  Flows not undergoing phase change involve two different immiscible chemical components, and are sometimes referred to as two-component, two-phase flows (*e.g.*, nitrogen-water flow) [7].  Phase-change flows contain a single component but comprise two different phases separated by an interface; steam-water flow is an example of a single-component, two-phase flow.  Phase-change flows can be either condensing (flow condensation) or evaporating (flow boiling).

## 2.1   Flow Boiling Instabilities

Flow instabilities are undesired phenomenon commonly observed in systems with flow undergoing phase change.  These instabilities can lead to premature critical heat flux relative to the conventional dryout mechanism [8].  In an effort to better understand these instabilities and their implications, flow boiling instabilities have received significant attention through experimental and theoretical analyses, as well as a number of reviews on the subject [9-12].  Two classes of flow instabilities have been widely recognized in the literature, dynamic and static.  The types of instabilties depend on the system configuration and size.  The five most commonly observed flow boiling instabilities at the microscale and their corresponding class are listed in Table 2.1 and discussed in detail in the following paragraphs.

Table 2.1 Common microscale flow boiling instabilities.

| Instability Type | Class |
|---|---|
| Rapid-Bubble-Growth Instability | Dynamic Instability |
| Pressure Drop Instability | Dynamic Instability |
| Parallel Channel Instability | Dynamic Instability |
| Ledinegg Instability | Static Instability |
| Critical Heat Flux | Static Instability |

## 2.1.1   Dynamic Instability

Flow is subjected to a dynamic instability when there is sufficient interaction between the inertia of the flow and the compressibility of the system, leading to delayed feedback [10]. Dynamic flow instabilities commonly encountered in microscale applications include the rapid-bubble-growth instability, pressure drop instability (sometimes referred to as the upstream compressible volume instability), and parallel channel instability [13].

## 2.1.1.1   Rapid-Bubble-Growth Instability

The one dynamic instability that is unique to microscale flow boiling and not observed in macroscale systems is the rapid-bubble-growth instability [14]. The small characteristic channel sizes confine vapor bubbles formed during boiling, causing the bubbles to significantly influence the operating characteristics of the system. This confinement causes the bubbles to significantly influence the operating characteristics of the system, and can cause pressure fluctuations and flow reversal [15]; under certain operating conditions, this can lead to large wall temperature excursions at the onset of boiling [16]. Two underlying mechanisms contribute to the rapid-bubble-growth instability, *viz.*, the large liquid superheat needed to induce vapor bubble nucleation and the large pressure spike generated within a microchannel that propagates through the surrounding liquid due to rapid growth of a confined bubble [14].

### 2.1.1.2 Pressure Drop Instability

The pressure drop instability is attributed to the interaction between the vapor within the heated channel and the compressibility in the flow path upstream of the channel [17]. As the amount of vapor within the channel increases, the flow resistance increases. If a compressible upstream volume is present, the liquid flow rate through the channel will decrease and in turn, cause additional vapor generation within the channel. For a constant system flow rate, this momentary reduction in flow rate is confined to the channel and the increased flow resistance within the channel is accompanied by an increase in the inlet pressure of the channel. Once a critical inlet pressure is reached, liquid is forced through the channel and flushes out most of the vapor, thereby reducing the flow resistance and inlet pressure. This highly transient cyclical process is often time-periodic and is classified as the pressure drop instability. The underlying mechanism responsible for the pressure drop oscillations is the cyclical compression and expansion of the upstream compressible volume and its interaction with the vapor within the channel. The pressure drop instability can cause premature critical heat flux when entry of liquid into the heated channel is delayed and vapor occupies most of the channel for a relatively extended period of time.

### 2.1.1.3 Parallel Channel Instability

Like the pressure drop instability, the parallel channel instability is attributed to interaction between the vapor within the heated channel and the compressibility of the system. In addition to the upstream compressible volume, the introduction of parallel channels adds an additional compressible volume, resulting in feedback between channels. In systems consisting of two parallel channels, the flow oscillations resulting from the parallel channel instability are

typically out of phase with each other [9] and are typically less severe than those caused by the pressure drop instability [17].

### 2.1.2   Static Instability

Flow is subjected to a static instability if, when disturbed, its new operating conditions tend asymptotically toward operating conditions that differ from the initial ones [10].  The threshold of operating conditions at which static instabilities are observed can be predicted using steady-state laws [9, 18, 19].  The most common static flow instabilities encountered in microscale flow boiling applications are the Ledinegg (flow excursion) instability and critical heat flux.

### 2.1.2.1   Ledinegg (Flow Excursion) Instability

The Ledinegg, or flow excursion, instability is said to occur when there is a sudden reduction in the flow rate through a channel [9].  The Ledinegg instability (named after Ledinegg for his pioneering work [20]) occurs when the slope of the channel demand (internal characteristic) curve, defined as the pressure drop versus mass flux curve, becomes algebraically smaller than the supply (external characteristic) curve: $(\partial \Delta p / \partial G)_{int} < (\partial \Delta p / \partial G)_{ext}$.

### 2.1.2.2   Critical Heat Flux

Critical heat flux indicates a transition from a very effective heat transfer process to a very ineffective process and is usually accompanied with a sudden increase in the surface temperature [8].  During flow boiling, it is desirable to have the heated surface primarily covered in liquid because the liquid phase has significantly better heat transfer properties (*e.g.*, thermal conductivity) than the vapor phase.  When the heated surface becomes temporarily or

permanently covered by the vapor phase, the critical heat flux is reached and the surface

temperature rises quickly, often resulting in device failure.

### 2.1.3   Isolation of Instability Types

Several studies that investigated flow boiling instabilities with parallel microchannel

configurations reported coupled effects of multiple instability types [13, 14, 17, 21].  For

example, Qu and Mudawar [17] investigated the pressure drop instability and the parallel

channel instability in a microchannel heat sink with 21 parallel channels using water as the

working fluid.  The addition of a throttling valve upstream of the heat sink suppressed the large-

amplitude, periodic pressure drop oscillations which enabled the parallel channel instability to be

recognized.  The throttling valve stiffens the system and minimizes the effects of upstream

compressibility, but increases system pressure drop.

One approach to isolate individual instability types and identify their underlying

mechanisms is to investigate a single-channel configuration in which individual mechanisms can

be more easily observed.  Huh *et al.* [22] used high-speed imaging to qualitatively observe flow

reversal in a single microchannel due to the flow regime transition instability which resulted in

the growth of elongated bubbles.  This instability was quantified using a relatively low-frequency

sensor, and high-frequency flow oscillations associated with individual bubble growth events

could not be quantitatively resolved.  Wang and Cheng [23] used a single microchannel with 15

heaters and resistance temperature detectors positioned along its axial length to measure the

time-resolved wall temperature and pressure drop during flow boiling with deionized water.

They demonstrated that a critical exit vapor quality cutoff separated stable and unstable flow

boiling, wherein the stability was judged based on the absence or presence of pressure and

temperature fluctuations.  Barber *et al.* [15] used pressure and temperature measurements,

synchronized with high-speed flow visualization, to observe the rapid-bubble-growth instability during microchannel flow boiling. A syringe pump was used to deliver a constant mass flux in the experiments.

However, extrapolating the results of single-channel flow instability studies to behavior in parallel microchannel heat sinks is difficult because of potential differences in the hydrodynamic boundary conditions. The constant mass flux used in many single-channel studies [15, 23, 24] is different from conditions in an individual channel that is part of a parallel-channel system. The behavior of a single channel in a parallel-channel system does not significantly influence the full set of channels thus resulting in a hydrodynamic boundary condition similar to that of a constant pressure drop. In this parallel-channel configuration, the flow rate through an individual channel can fluctuate significantly, resulting in severe thermal oscillations.

## 2.2    Microscale Flow Boiling Regimes

Two-phase mixtures can form a wide range of morphological flow configurations and it has been shown experimentally that the heat transfer performance and dominant heat transfer mechanisms depend heavily on the flow morphology [25-27]. These flow regimes depend on several factors, including fluid properties, operating conditions, system configuration/orientation, and system size, to name a few. Significant efforts has been directed toward predicting and characterizing the flow regimes under a wide range of these factors. At the microscale, commonly observed flow regimes are bubble, slug, churn, and annular flow [28]. During flow boiling in microchannels, nucleation and departure of vapor bubbles from the channel wall almost immediately leads to a slug flow regime for channel sizes below a critical value, due to the influence of surface tension and vapor confinement [29]. At high vapor qualities, the slug regime transitions to the annular regime, making these two regimes the most commonly observed

flow regimes at the microscale. The slug flow boiling regime, schematically illustrated in Figure 2.1a, is characterized by elongated vapor bubbles that are circumferentially confined and partitioned in the streamwise direction by liquid slugs. A thin liquid film separates the vapor bubbles from the channel wall. The annular flow regime, schematically illustrated in Figure 2.1b, is characterized by a continuous vapor core with a thin liquid film that separates it from the channel wall. In both the slug and annular regimes, evaporation in the thin liquid film has been shown to be the dominant heat transfer mechanism [30].

**(a) Slug Flow**

Vapor Bubble  Liquid Slug  Liquid Film  Channel Wall

**(b) Annular Flow**

Vapor Core  Liquid Film  Channel Wall
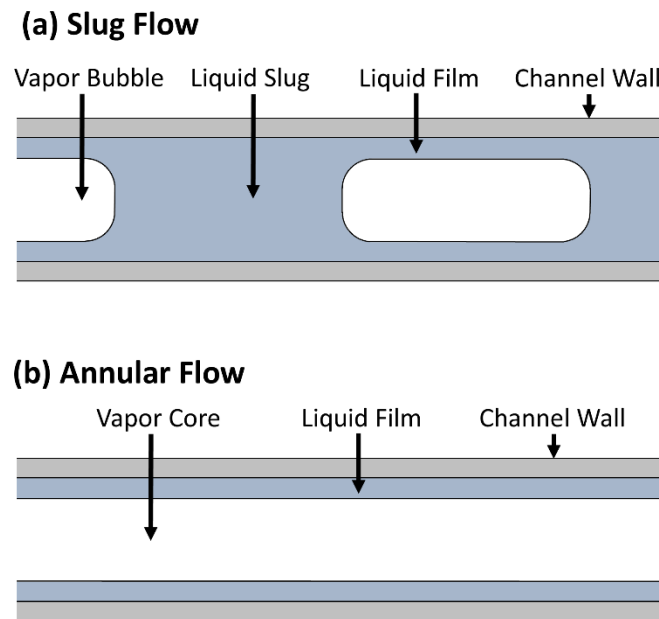
Figure 2.1. Schematic diagram illustrating the (a) slug and (b) annular flow boiling regimes.

## 2.3   Development of Physics-Based Flow Boiling Models

Several mechanistic flow boiling models of increasing complexity have been proposed for slug and annular flow because they feature relatively simple geometric features and are observed across a wide range of operating conditions [27, 31-33]. Peles *et al.* [34] developed a one-dimensional model featuring distinct liquid and vapor regions partitioned by an evaporating interface. Jacobi and Thome [35] proposed a 'two-zone' model consisting of an evaporating

vapor bubble region surrounded circumferentially by a thin liquid film, with successive bubbles partitioned by a liquid slug region. A model for the conduction resistance of the thin liquid film was used to describe the effective evaporative heat transfer coefficient. A 'three-zone' model was presented by Thome *et al.* [30] by including an additional vapor slug region, where no liquid film exists, and a method for prediction of the liquid film thickness. This model was later adapted by Harirchian and Garimella [27] to include a correlation for the liquid film thickness specific to microchannel length scales. While the aforementioned two- and three-zone models were strictly developed for circular microchannels, a 'four-zone' model was developed by Wang *et al.* [36] to account for a partial dryout region resulting from corner effects in microchannels of rectangular cross-section.

Several recent studies have developed multiphase numerical models for flow boiling that account for complex vapor-liquid interfacial transport phenomena [37-41]. For example, Pan *et al.* [40] demonstrated a cost-effective approach for modeling microchannel flow boiling using a volume-of-fluid (VOF) approach coupled with a saturated-interface-volume phase change model and a moving-reference-frame method that suppresses spurious currents [42]. The growth of single, evaporating vapor bubbles flowing in heated microchannels was simulated. While this was an important step toward the ultimate goal of a comprehensive numerical simulation of the complete flow boiling problem, a continuous stream of vapor bubbles is more representative of two-phase flows and poses additional challenges for modeling due to the hydrodynamic and thermal interaction between successive vapor bubbles [43]. Magnini and Thome [44] computationally investigated the hydrodynamics and heat transfer characteristics of microchannel slug flow under saturated flow boiling conditions using a continuous stream of artificially generated vapor bubbles. The first vapor bubble entering a fully developed liquid-

phase flow and temperature profile had a significantly higher evaporation rate relative to successive vapor bubbles due to the large amount of sensible heat available in the superheated liquid regions; time-periodic behavior was observed after approximately five vapor bubbles.

Despite the recent significant advances in modeling, these state-of-the-art techniques are still validated using test problems for which simplistic analytical solutions are available [38, 40, 41, 45, 46], comparison to temporally and spatially averaged transport quantities that can be easily measured experimentally [39], or cross-comparison between the different numerical modeling approaches [40]. There is a clear need for high-fidelity benchmark experimental data that can be used as a common basis for validation of sophisticated flow boiling models.

## 2.4    Controlled Experimental Generation of Flow Boiling Regimes

Two-phase flows are traditionally generated in flow boiling experiments by vapor bubble nucleation from a heated surface. This incipience-based approach gives rise to a streamwise progression of flow regimes, typically transitioning from bubble to slug to annular flow. Large stochastic hydrodynamic variations, flow instabilities, and the close proximity of successive vapor bubbles that arise from the nucleation process confound the development of a comprehensive database of well-conditioned experimental results that is amenable for use in the validation of flow boiling models.

Recent experimental efforts have explored innovative techniques that control vapor bubble generation by avoiding a reliance on spontaneous nucleation. Bigham and Moghaddam [47] demonstrated active nucleation control from a 300 nm-diameter heated cavity. By varying the amplitude and period of a pulsed square wave, different time-periodic flow regimes ranging from bubbly to slug to annular were realized in a 120 μm-hydraulic diameter microchannel at very low Reynolds numbers. A method for producing the desired two-phase flow characteristics

while completely avoiding nucleation has also been proposed. Scammell and Kim [48] fabricated a test facility capable of producing a single vapor bubble of a desired length which was then injected into a liquid vertical upflow in an optically opaque, heated 6 mm macrochannel. There is a need for experimental approaches capable of producing a continuous stream of vapor bubbles that appropriately emulates the physical behavior of slug flow boiling, with successive vapor bubbles separated by liquid slugs. Such an approach would enable characterization of key hydrodynamic and heat transfer parameters under well-defined boundary and flow conditions that are commonly encountered in microchannel heat sinks.

## 2.5    Transient Characterization of Flow Boiling

High-frequency thermal-fluidic characterization techniques (*e.g.*, measurement of pressure, mass flux, and temperature) are needed to resolve the transient flow boiling features. Rao *et al.* [49] embedded thin-film titanium heaters and thermistors beneath a single microchannel to allow heating and measurement of surface temperatures with high spatial and temporal resolution during flow boiling. Local surface temperatures were significantly influenced by bubble nucleation, thin-film evaporation, and dryout. Bigham and Moghaddam [47] custom-fabricated a test section that could make temperature measurements at 20,000 Hz using a series of 50 μm-wide resistance temperature detectors, enabling local heat flux measurements with spatial and temporal resolutions of 40-65 μm and 50 μs, respectively. Local vapor bubble dynamics were shown to influence the instantaneous heat transfer rates and mechanisms. Zhu *et al.* [50] used high-frequency wall temperature measurements to study the effect of adding hydrophilic micropillars to the bottom surface of square microchannels on the pressure drop instability and the resulting wall temperature variations. At heat fluxes just beyond that needed to cause boiling, large-amplitude wall temperature fluctuations were

observed due to transitions between single-phase and two-phase flow. As the heat flux or mass flux was increased, the wall temperature oscillation frequency increased. Higher mass fluxes also mitigated flow reversal. The micropillars promoted capillary-assisted rewetting of the wall and reduced the magnitude of the temperature oscillations compared to a smooth surface, but their influence on the hydrodynamic oscillations and the coupled thermal-fluidic behavior was not investigated.

## 2.6    Flow Boiling Performance During Transient Heating Conditions

Many applications undergo transient operation resulting in a time-varying heat generation, such as central processing units (CPUs), radio-frequency power amplifiers, laser diodes, and avionics [51]. These thermal transients can have repercussions on device operation and result in poor performance, reduced reliability, and even device failure. For example, gallium nitride power amplifiers used in multifunctional radar systems often suffer from self-heating electrothermal 'memory effects' when switching between different coherent processing intervals, which lead to changes in the amplifier gain and insertion phase that negatively affect device performance [52]. Recent interest in 'embedded cooling' strategies that would embed coolant channels within the device, near the source of heat generation, can exacerbate the effects of transient heating conditions [53]. These heating transients can lead to flow boiling instabilities and oscillations, which have been shown to reduce the heat transfer coefficient [54-56] and critical heat flux [57].

To address these concerns, researchers have begun to study the impact of transient heating conditions on flow boiling performance. Basu *et al.* [58] performed an experimental study to identify parametric trends governing the transient wall temperature during HFE-7000 flow boiling through a microgap in response to a heat flux step change and single pulse. The

effects of mass flux, heat flux amplitude, and pulse duration were investigated. The onset of boiling and bubble dynamics were observed using high-speed flow visualization. At low heat fluxes, nucleation of discrete bubbles governed the heat transfer performance, whereas at high heat fluxes nucleation quickly led to a vapor film over the heater surface and a large temperature rise. Huang *et al.* [59] performed an experimental study to investigate the base temperature response of a multi-microchannel evaporator during a 'cold startup' (*i.e.*, heat flux step change from zero to a given level). An infrared camera was used to measure the base temperature synchronous to flow visualization captured with the high-speed camera. At the onset of boiling, the base temperature increased significantly, well above the steady wall temperature during constant heating conditions. However, reducing the inlet orifice width, heat flux magnitude, inlet subcooling, and outlet saturation temperature, or increasing the mass flux, decreased the maximum base temperature during this transient event. Using the same experimental setup, Huang *et al.* [59] also studied the effects of periodic heat pulses on the base temperature of a two-phase parallel channel heat sink. Near the inlet of the channels, the flow oscillated between single-phase flow and subcooled boiling, resulting in large oscillation amplitudes and a higher overall temperature. Further downstream, continuous flow boiling was observed thus reducing the oscillation amplitude and the overall temperature. Chen and Cheng [60] studied the flow boiling phenomena and surface temperature response of a microheater in a single microchannel subjected to a 2 ms-long heat pulse. The temperature of the platinum microheater was measured synchronously to flow visualization for various heat and mass flux combinations. For a given mass flux, nucleate boiling was the dominant heat transfer mechanisms at low heat flux levels whereas film boiling dictated the performance at high heat flux levels. Miler *et al.* [61] studied flow boiling in a single microchannel and found that for the same total heater power, pulsed

heating conditions cause an increase in the time-averaged device temperature. Aguiar and Ribatski [62] investigated the effects of transient heat flux variations on wall temperature and HTC by performing flow boiling experiments at various heat and mass fluxes and inlet vapor qualities for R134a in a 1.1 mm diameter stainless steel tube. Sinusoidal, square, and sawtooth transient heating profiles were applied to a 10 mm hotspot that was centrally located along a 90 mm heated region of the tube. Parametric trends were reported for various transient hotspot heating waveforms, frequencies, and amplitudes.

# 3 HIGH-FREQUENCY THERMAL-FLUIDIC CHARACTERIZATION OF THE RAPID-BUBBLE-GROWTH INSTABILITY AT THE ONSET OF BOILING

This chapter provides a description of the experimental test facility used to conduct the flow boiling instability studies in Chapters 3 and 4. This chapter assesses the effect of flow inertia and inlet liquid subcooling on the rapid-bubble-growth instability at the onset of boiling, and quantifies its underlying mechanisms. The material from this chapter was published in *International Journal of Multiphase Flow* [16].

This research is sponsored by the Naval Engineering Education Consortium (NEEC), with support of Naval Surface Warfare Center (NSWC) Crane Division in Crane, Indiana. Special thanks to Dr. Brian D. Olson (NSWC Crane Division) for technical discussion of this work.

## 3.1 Experimental Methods

### 3.1.1 Test Facility

The custom-built experimental facility, schematically illustrated in Figure 3.1, uses a pressurized reservoir to deliver degassed, dielectric HFE-7100 liquid (Novec Engineered Fluid, 3M; fluid properties listed in Table 3.1) to the test section. The pressure difference between this reservoir and the ambient is used to generate an open-loop flow. The rigid stainless steel reservoir is pressurized by boiling fluid using a submerged cartridge heater (G6A-15568, Watlow). Electrical power is supplied to the cartridge heater using an adjustable direct current (DC) power supply (XG 850W 150-5.6, Sorensen). A constant reservoir pressure is set and maintained by adjusting the amount of power delivered to the cartridge heater.

Liquid is extracted from the reservoir through an internal dip tube. The liquid flow rate and the test section outlet saturation pressure are adjusted using a pair of needle valves (FVL-404-SS and FVL-405-SS, Omega Engineering), one upstream and one downstream of the test section, respectively. The liquid volumetric flow rate and temperature are measured using a liquid flow meter (LC-10CCM-D-EPDM, Alicat; accuracy of ±1% full scale). The liquid mass flux is determined using the measured volumetric flow rate and the density corresponding to the measured liquid temperature at that location. The fluid is preheated to the desired inlet temperature immediately upstream of the test section, using a constant-temperature circulating bath (NESLAB EX 17, Thermo Electron Corp.). The inlet and outlet fluid temperatures are measured immediately upstream and downstream of the test section, respectively, using small exposed-tip thermocouples (TMTSS-020E-6, Omega Engineering; accuracy of ±0.5 °C) featuring a bead diameter of ~250 μm, which enables dynamic changes in fluid temperatures to be measured. The pressures at the inlet and outlet of the microchannel are measured using separate pressure transducers (PX309-030G5V and PX309-015G5V, respectively, Omega Engineering; accuracy of ±1.0%). Short, rigid stainless steel tubes were used to connect the pressure transducers to the polyetheretherketone (PEEK) connectors (ZX2LPK, Valco Instruments) to minimize damping and enable dynamic pressure fluctuations to be accurately measured. Two individual pressure transducers were used instead of a differential pressure transducer to minimize the volume of fluid that would effectively be in parallel with the test section; the pressure measurements were observed to be damped when the use of a differential transducer was explored. The pressure drop across the test section is taken as the difference between the inlet and outlet pressure measurements. The thermocouples and pressure transducers, in addition to the fluid inlet and outlet connections, are mounted to the PEEK

connectors, as shown in Figure 3.1; the test-section microchannel is mounted horizontally between these connectors.

The circular cross-section microchannel is made of borosilicate glass (CV5070, VitroCom) with an inside diameter of $D = 500$ μm and a wall thickness of 100 μm. The outside surface of the microchannel is custom-coated with an approximately 100 nm-thick layer of indium tin oxide (ITO) using atomic layer deposition (Ultratech Inc.). The ITO layer is optically transparent and electrically conductive, enabling visualization of the two-phase flow while subjected to uniform Joule heating. Power is supplied to the ITO coating using an adjustable DC power supply (XG 850W 300V-2.8A, Sorensen). The ITO layer is electrically isolated from the flow loop using non-conductive polytetrafluoroethylene (PTFE) ferrules and PEEK nuts for attachment of the microchan2nel to the PEEK connectors. Any vapor leaving the test section condenses before discharging as liquid to an open reservoir at ambient pressure.

Pressure, mass flux, and fluid temperature measurements are obtained at 2500 Hz using a high-frequency data acquisition (DAQ) unit (USB-6259, National Instruments). The power to the test section is measured at 0.4 Hz using a separate, high-voltage DAQ (34970A, Agilent). The total heating power (which includes power loss to the ambient) applied to the test section is quantified by measuring the voltage drop across and current through the ITO microchannel coating; the current is obtained from a shunt resistor (6142-1-1000, Empro Shunts). The entire experimental facility is mounted on a damped optical table (VIS3672-PG2-325A, Newport Corp.) to ensure that external vibrations are not transmitted to the components.

The microchannel outside wall temperature is measured at a single fixed location using an infrared (IR) camera (SC7000, FLIR) pointed vertically downward at the microchannel. The IR objective lens (ASIO 4×, Janos Technology, Inc.) is focused on a single black dot painted on

the outside surface of the microchannel.  This IR imaging configuration enables nonintrusive measurement of the wall temperature without obscuring the flow visualization.  Infrared images were acquired at 500 frames per second (fps) using an image resolution of $80 \times 64$ pixels.  An IR camera integration (*i.e.*, exposure) time of 90 μs was used, which enabled wall temperatures up to approximately 200 °C to be measured before saturating the IR camera sensor.

The flow is visualized from the side of the microchannel using a high-speed camera (VEO710L, Phantom) coupled to a macro lens (AF Micro-Nikkor, Nikon).  The opposite side of the microchannel is uniformly backlit using a high-intensity light-emitting diode (LED) strip with an integrated light diffuser (BL168, Advanced Illumination).  High-speed optical and IR images were synchronized to pressure, mass flux, and temperature measurements using a pulse generator (565, Berkeley Nucleonics Corp.) to simultaneously trigger both cameras and the high-frequency DAQ unit.
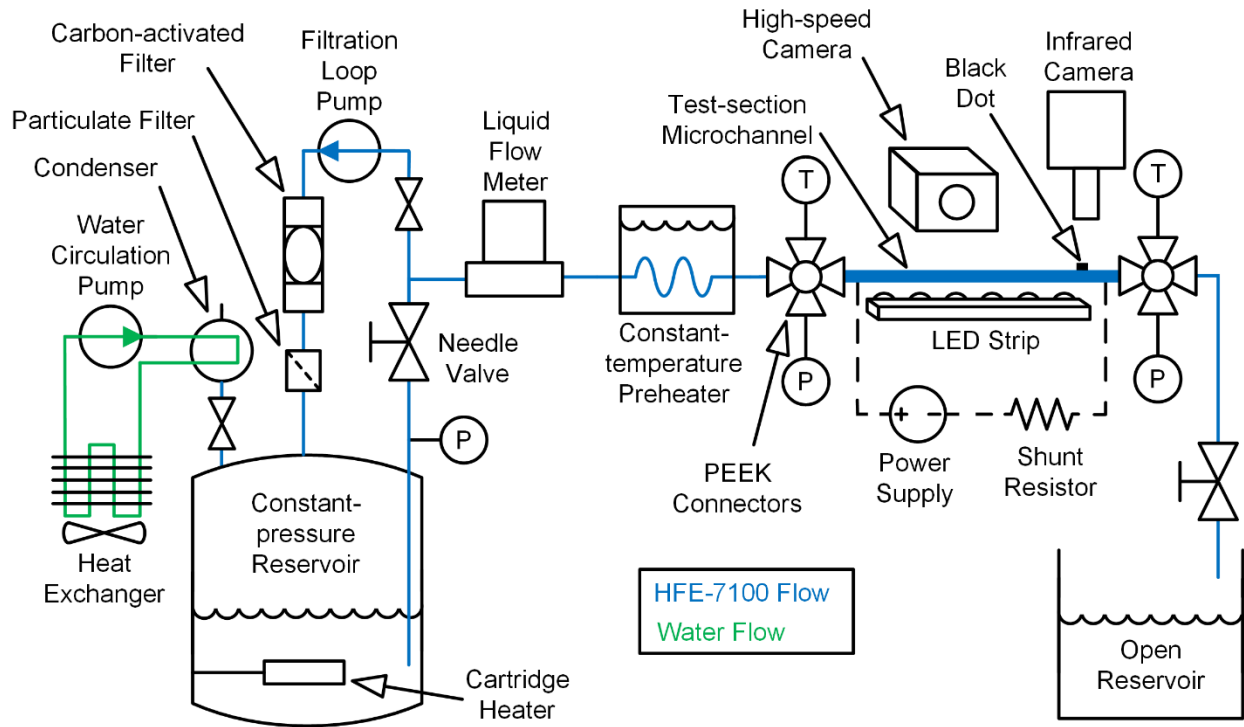
Figure 3.1 Schematic diagram of the experimental facility featuring a constant pressure reservoir used to deliver fluid flow through the heated test section microchannel.

Table 3.1. Fluid properties of saturated HFE-7100 at atmospheric pressure [63].

|  | Liquid | Vapor |
|---|---|---|
| Density, $\rho$ [kg/m$^3$] | 1399 | 9.87 |
| Specific heat, $c_p$ [J/(kg °C)] | 1255 | 929 |
| Thermal conductivity, $k$ [W/(m K)] | 0.0618 | 0.0156 |
| Dynamic viscosity, $\mu$ [kg/(m s)] | $3.61 \times 10^{-4}$ | $1.12 \times 10^{-5}$ |
| Heat of vaporization, $h_{fg}$ [J/kg] | — 111600 — | |
| Saturation temperature, $T_{sat}$ [°C] | —— 61 —— | |
| Surface tension, $\sigma$ [N/m] | — 0.0103 — | |

### 3.1.2  Test Procedure

Immediately prior to testing, the HFE-7100 fluid was degassed by vigorously boiling the

liquid in the reservoir using the submerged cartridge heater.  An auxiliary pumped loop

circulates water through a condenser (Figure 3.1) to condense the vapor, which falls back into

the reservoir, while non-condensable gases are expelled from the system. While degassing, the HFE-7100 was also circulated through an auxiliary pumped loop containing a 2 μm particulate filter (SS-4TF-2, Swagelok) and an activated-carbon filter (12011 Pall Corporation) to remove any contaminants. After degassing and filtering, the pumps in these auxiliary loops were turned off.

Experiments were initiated by boiling the liquid in the reservoir until it reached a constant reservoir pressure of 190 kPa. Liquid flow was then initiated through the test section at the desired nominal single-phase mass flux while maintaining an average test section outlet saturation pressure of 114 kPa, which corresponds to an outlet saturation temperature of 65 °C, by adjusting the needle valves. The test facility features a constant pressure drop across the system, not a constant mass flux, and thus a nominal single-phase mass flux is defined based on the value measured prior to the onset of boiling. The constant-temperature bath setpoint was then adjusted to heat the liquid to the desired inlet temperature.

After establishing the desired flow conditions, power was applied to the ITO-coating on the microchannel in increments, allowing for steady-state conditions to be achieved between each set point. At low power conditions, the flow remained in a single phase. At a power level large enough to cause the onset of boiling, all sensor and imaging (IR and optical) data were recorded synchronously immediately before and after incipience, thus capturing this transient event. During this onset of boiling, optical images were acquired at 50,000 fps for a duration of 7.85 s, extending approximately 6 s after boiling was initiated.

### 3.1.3   Data Reduction

The wall temperature of the microchannel is determined from measurement of the IR image intensity in a $30 \times 24$-pixel region in the middle of the black dot painted on the outer wall

of the microchannel. This intensity is converted to a temperature using a calibration of the IR camera that was performed after testing was complete. For the calibration, the IR camera is focused on a target surface featuring the same black paint used on the microchannel and was varied from 20 °C to 200 °C in approximately 10 °C increments while recording the image intensity. A unique fourth-order polynomial fit of this temperature versus intensity data for each pixel in the imaging region is used to convert the intensity measured during testing to a microchannel wall temperature. The average wall temperature for each image is then calculated by computing the spatial average from the $30 \times 24$-pixel region.

A portion of the total power supplied to the ITO coating on the microchannel is lost to the ambient (*i.e.*, not transferred to the fluid through the microchannel wall). This heat loss is a function of the channel wall temperature and was calibrated after testing. First, the HFE-7100 was drained from the test-section microchannel and the channel was open to the ambient. Next, electric power levels ranging from 0 - 1.5 W (in approximately 0.1 W increments) were applied to the microchannel. In this configuration, all of the supplied heat is lost to the ambient. The wall temperature is measured using the IR camera at each power level and a linear fit is applied: $P_{loss} = 0.0086 \, T_{wall} - 0.2188$. This temperature-dependent heat loss equation had a coefficient of determination of $R^2 = 0.98$. A time-averaged wall temperature (over each data acquisition time) is used to quantify the heat loss that occurs during testing, resulting in different heat losses for each operating condition. The power into the microchannel is calculated by subtracting the power loss from the total electric power supplied using $P_{in} = P_{total} - P_{loss}$; power is calculated using $P_{total} = VI$ where $V$ is the voltage applied to the test section and $I$ is the current through the test section. The time-averaged heat flux into the test section is calculated using $q_{in,avg} = P_{in} / (\pi \, D \, L_{heated})$.

The instantaneous mass flux through the test section is calculated using $G = Q\rho \, / \, (\pi D^2/4)$ where $Q$ is the measured volumetric flow rate and $\rho$ is the calculated liquid density corresponding to the measured liquid temperature at the flow meter. The inlet liquid subcooling is determined using $\Delta T_{sub} = T_{sat,out,avg} - T_{in}$ where $T_{sat,out,avg}$ is the time-averaged fluid saturation temperature corresponding to the measured pressure at the outlet of the test section and $T_{in}$ is the inlet fluid temperature. The pressure drop across the test section is calculated as the difference between the test section inlet and outlet pressures, $\Delta p = p_{in} - p_{out}$.

### 3.1.4   Design of Experiments

Five different combinations of nominal single-phase mass flux and inlet liquid subcooling were investigated in this study, as shown in Table 3.2. The test procedure described in Section 3.1.2 was adopted for each combination. In this study, the nominal single-phase mass flux is varied, enabling the effect of flow inertia to be studied, while holding the inlet liquid subcooling constant at $\Delta T_{sub} = 5$ °C. Similarly, the inlet liquid subcooling is varied while holding the nominal single-phase mass flux constant at $G_{1\phi} = 400$ kg/m²s.

Table 3.2 Operating conditions used in this study to investigate the rapid-bubble-growth instability.

| Nominal Single-Phase Mass Flux, $G_{1\phi}$ [kg/m²s] | Inlet Liquid Subcooling, $\Delta T_{sub}$ [°C] |
|---|---|
| 200 | 5 |
| 400 | 5 |
| 400 | 15 |
| 400 | 35 |
| 800 | 5 |

## 3.2    Results and Discussion

When the flow transitions from single-phase to two-phase, the rapid-bubble-growth instability is observed at the onset of boiling, and is captured in the flow visualizations and transient sensor measurements.  Figure 3.2a shows a series of selected images at the onset of flow boiling obtained by the high-speed camera for a nominal single-phase mass flux of 400 kg/m²s and an inlet liquid subcooling of 5 °C.  The nominal flow direction (positive mass flux) is from left to right.  The entire heated length of the microchannel ($L_{heated}$ / $D$ = 84) is shown in the frame; the electrical connections to the ITO coating are just outside the viewing region.  Figure 3.2a ($t$ = 0.024 s) shows the single-phase liquid flow immediately prior to nucleation.  The small black dot visible in each image, on the top portion of the channel near the outlet, is the location of the IR wall temperature measurement.  The entire microchannel cross-section is shown in each image (A-L) and appears uniformly gray; the wall thickness is virtually unidentifiable in the images at the magnification shown.  The reservoir, inlet, and outlet pressures, pressure drop across the channel, mass flux, inlet and outlet fluid temperatures, and wall temperature data recorded immediately before and after the onset of boiling (0 s < $t$ < 0.1 s) are shown in Figure 3.2b.  A longer-timescale plot (0 s < $t$ < 1.0 s) is shown in Figure 3.2c to

illustrate the transition from the onset of boiling to time-periodic boiling. The gray shaded box and dashed vertical lines in Figure 3.2b correspond to the time instances in Figure 3.2a when the flow visualizations were captured (images A-L).

Prior to nucleation (*i.e.*, during single-phase flow), all the sensor measurements remain constant in time, as shown in Figure 3.2b from $0 \text{ s} < t < 0.024 \text{ s}$. Immediately prior to nucleation, the outlet fluid temperature is 78.0 °C, corresponding to a large liquid superheat of 12.4 °C relative to the outlet saturation temperature of the fluid (65.6 °C). The glass microchannel used in this study has a smooth inside wall and HFE-7100 is a highly wetting liquid; these characteristics impose a large energy barrier for nucleation that typically suppresses vapor bubble formation during boiling until a large liquid superheat is attained, for example, as shown by Kuo and Peles [14] for the walls of smooth silicon microchannels. At $t = 0.025 \text{ s}$, a single vapor bubble nucleates from the top portion of the inside wall of the microchannel near the middle of the heated region (Figure 3.2a). Nucleation at the onset of boiling preferentially occurred at this location, likely because of a small imperfection on the inside surface. Once formed, the small vapor bubble grows very rapidly both upstream and downstream from the nucleation site. This explosive growth is attributed to the vapor bubble being surrounded by superheated liquid, which drives rapid liquid-to-vapor phase change and volumetric expansion of the bubble due to the density difference between vapor and liquid. As the vapor bubble becomes circumferentially confined by the microchannel wall, growth predominantly occurs in the axial direction. The furthest upstream and downstream portions of the vapor bubble feature a bullet-like shape, due to the high-velocity (3.5 m/s) propagation of the vapor-liquid interface. Rapid growth of the vapor bubble generates a large pressure spike within the microchannel that also propagates upstream and downstream through the liquid. As shown in Figure 3.2b, the inlet

pressure begins to abruptly increase at $t = 0.026$ s until it reaches a maximum pressure of 283 kPa at $t = 0.030$ s. The pressure spike is so large that the inlet pressure exceeds that of the reservoir pressure (190 kPa). Similarly, the outlet pressure begins increasing at $t = 0.027$ s until it reaches a maximum pressure of 168 kPa at $t = 0.033$ s. The local spike in pressure promotes flow reversal upstream of the nucleation site. This local pressure spike, combined with the large liquid superheat that drives evaporation and expansion of the bubble, are the underlying mechanisms responsible for the rapid-bubble-growth instability. The faster response and increased pressure magnitude of the inlet pressure, relative to the outlet pressure, is attributed to the inability of the system to relieve the increasing pressure upstream of the rapidly growing vapor bubble. Instead, it begins to pressurize any compressible volume upstream of the test section.

Eventually, the entire heated length of the microchannel is occupied by a long continuous vapor bubble with only a thin layer of liquid separating it from the heated wall (Figure 3.2a; $t = 0.032$ s). This time instant approximately corresponds to maxima being observed in the inlet pressure and pressure drop, as shown in Figure 3.2b. A flow reversal is detected by the upstream flow meter, which measures a change in mass flux from the nominal single-phase flow condition of 400 kg/m$^2$s to virtually zero at $t = 0.042$ s and extends until $t = 0.057$ s (duration of 0.015 s); the flow meter is unable to measure negative flow rates, and shows a zero reading instead.

As the vapor-liquid interface moves downstream, and past the location of the wall temperature measurement (Figure 3.2a; $t = 0.029$ s), the liquid begins to cool as the excess sensible heat stored in the superheated liquid is converted to latent heat via evaporation. The outlet fluid temperature eventually decreases to the saturation temperature of the fluid. This process initially begins to cool the microchannel wall, as shown in Figure 3.2b at $t = 0.048$ s.

There is a 0.019 s delay between the vapor bubble passing the location of the temperature measurement and the wall temperature beginning to decrease, due to the thermal lag in conduction through the channel wall. At later times, the liquid film appears to thin and becomes more spatially uniform (*i.e.*, interfacial waves are eliminated) and the channel is filled with mostly vapor (Figure 3.2a; $t = 0.061$ s). Due to starvation of incoming liquid, the wall temperature then begins to increase at $t = 0.062$ s.

As the pressure wave that was generated at the onset of boiling travels upstream and downstream through the liquid, its magnitude decays and results in a reduction in the inlet and outlet pressures and eventually initiates a measurable mass flux at $t = 0.058$ s. The pressure build-up in the compressible volume upstream of the test section is relieved, causing the mass flux to increase to a maximum of 440 kg/m$^2$s at $t = 0.080$ s, exceeding the nominal single-phase mass flux for a brief time. The increased mass flux causes the vapor located upstream of the image frame to be forced back downstream and the furthest upstream portion of the vapor-liquid interface to become visible again within the viewing window (Figure 3.2b; $t = 0.069$ s). Small vapor bubbles begin to successively nucleate and depart from the microchannel wall at a fixed axial location (Figure 3.2b; $t = 0.073$ s). As these bubbles move downstream and grow, they coalesce and form larger, confined vapor bubbles resembling a slug flow regime before transitioning to churn and annular flow. After $t = 0.081$ s, the two-phase morphology begins exhibiting time-periodic fluctuations and the effects of the rapid-bubble-growth instability completely attenuate.

Figure 3.2c shows the pressure drop, mass flux, and wall temperature data for a longer duration ($0 < t < 1$ s) to illustrate the transition from the onset of boiling to time-periodic boiling; time-periodic oscillations in the pressure drop and mass flux are observed for $t > 0.081$ s (Figure

3.2c).  The thermal response is much slower than the hydrodynamic response due to the thermal

capacitance of the microchannel wall, and the wall temperature takes longer to achieve time-

periodic behavior (Figure 3.2c).  The wall temperature first increases 2 °C due to the rapid-

bubble-growth instability, from 133.4 °C during single-phase flow to a maximum wall

temperature of 135.4 °C at $t = 0.244$ s.  It then reduces due to the change in the two-phase

morphology and exhibits time-period fluctuations around a mean of 82 °C beginning at

approximately $t = 0.900$ s.
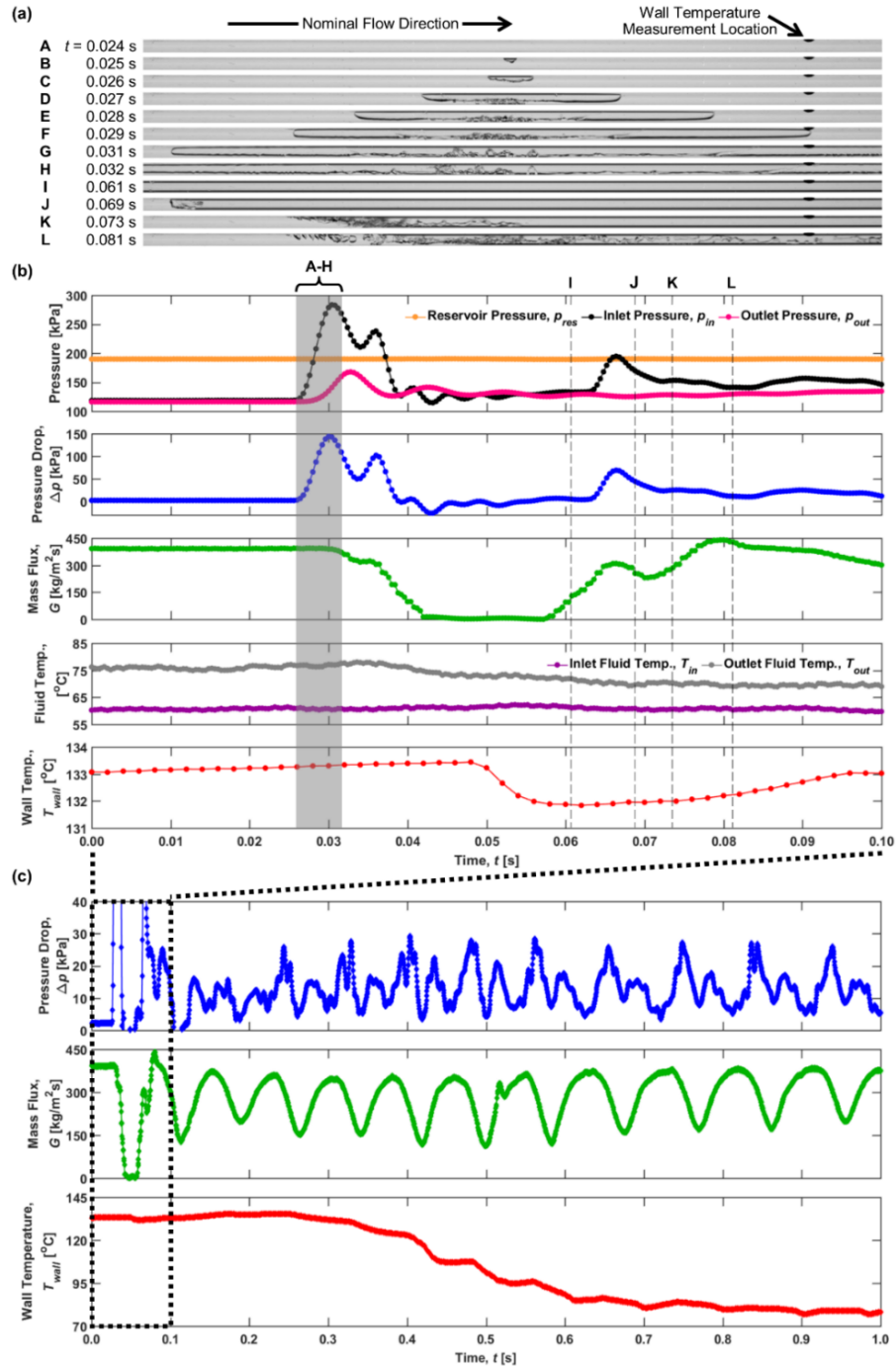
Figure 3.2. (a) Selected images of the two-phase morphology during the rapid-bubble-growth instability at the onset of boiling for $G_{1\phi} = 400$ kg/m$^2$s and $\Delta T_{sub} = 5$ °C, and (b) synchronized measurements of pressure, pressure drop, mass flux, inlet and outlet fluid temperatures, and wall temperature. Images A-L in (a) correspond to the time instances indicated by the gray box (A-H) and dashed vertical lines (I-L) in (b). The nominal flow direction in (a) is from left to right. (c) The pressure drop, mass flux, and wall temperature measurements are also plotted over a longer timescale showing the transition from the onset of boiling to time-periodic flow boiling.

### 3.2.1    Effect of Flow Inertia

While the rapid-bubble-growth instability at the onset of boiling for $G_{1\phi}$ = 400 kg/m$^2$s

and $\Delta T_{sub}$ = 5 °C only resulted in a 2 °C transient increase in the wall temperature relative to

single-phase flow that then decayed (Figure 3.2), this was not always the case. In particular,

when the flow inertia was reduced, a larger and longer transient temperature excursion was

observed. Figure 3.3 shows a series of selected images at the onset of flow boiling for a nominal

single-phase mass flux of 200 kg/m$^2$s and an inlet liquid subcooling of 5 °C, as well as the

synchronized pressure drop, mass flux, and wall temperature measurements before, during, and

after the onset of boiling on a longer timescale (0 s < t < 4.5 s). Prior to nucleation, the wall

temperature is 119 °C. Once a vapor bubble nucleated from the channel surface (Figure 3.3; $t$ =

0.299 s), it exhibits explosive growth both upstream and downstream, as in the discussion above.

Similarly, it is accompanied by a large pressure spike and a reduction in the mass flux (Figure

3.3b) to a value of zero. A mass flux value of zero (indicating flow reversal) is detected for a

duration of 0.066 s, a fourfold increase relative to the case with $G_{1\phi}$ = 400 kg/m$^2$s. The wall

temperature then begins to increase significantly and reaches a maximum temperature of 163 °C

at $t$ = 1.968 s. This larger increase in wall temperature is attributed to the lower flow inertia in

this case, which causes flow reversal (as detected by the flow meter) and the initial vapor bubble

that fills the channel (Figure 3.3a) to remain in place for a longer period of time for $G_{1\phi}$ =

200 kg/m$^2$s compared to $G_{1\phi}$ = 400 kg/m$^2$s, starving the heated wall of adequate liquid

replenishment. Such significant increases in the wall temperature caused by the rapid-bubble-

growth instability could be catastrophic to temperature-sensitive devices. Shortly after the wall

reaches its maximum temperature, the flow begins to enter a time-periodic flow boiling condition

where oscillations in pressure drop and mass flux are observed ($t$ > ~2.25 s). This cools the

microchannel wall and time-periodic wall temperature oscillations centered at ~75 °C begin at

approximately $t = 4.0$ s.

**(a)**



**(b)**
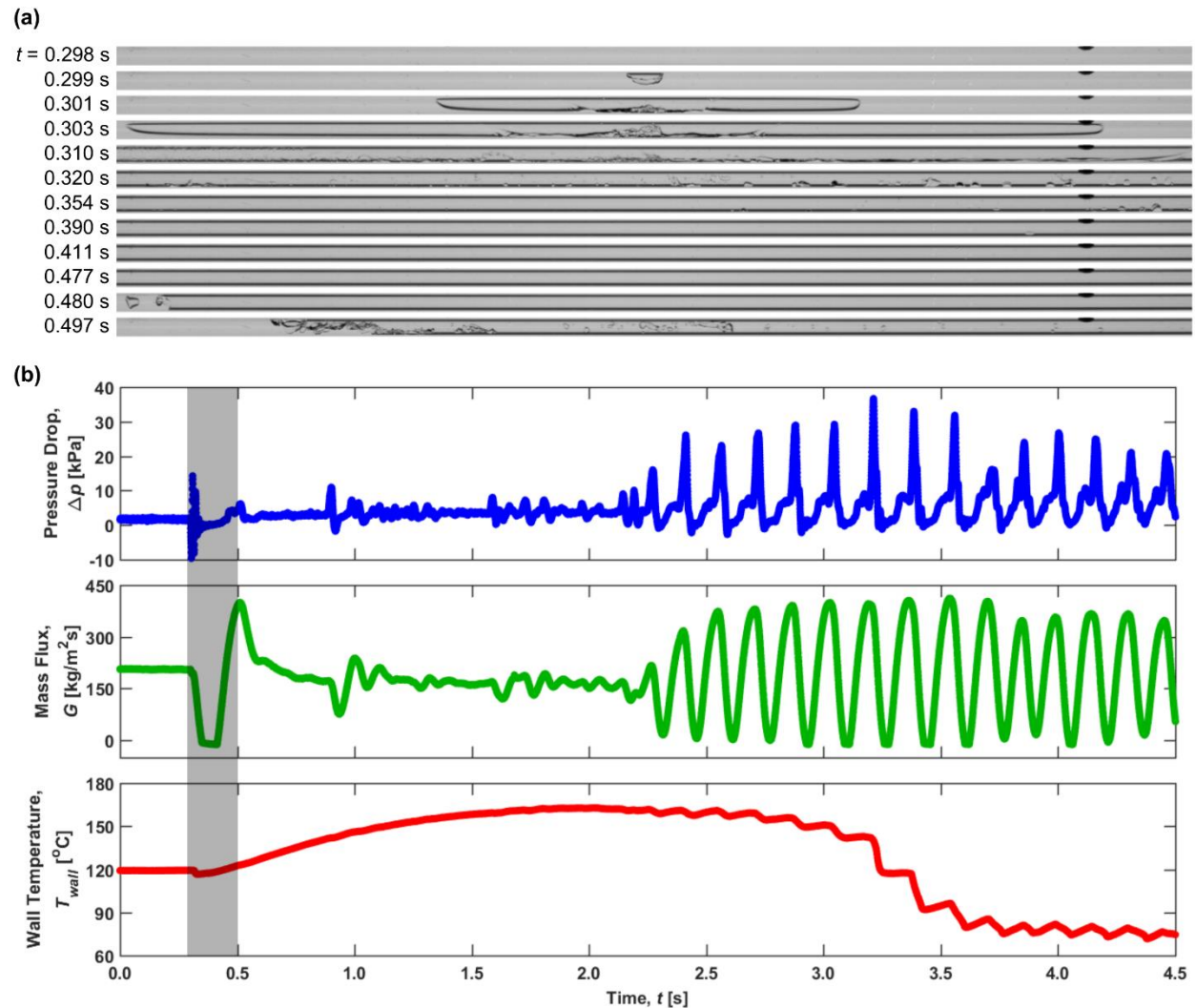


Figure 3.3. (a) Selected images of the two-phase morphology during the rapid-bubble-growth instability at the onset of boiling for $G_{1\phi} = 200$ kg/m²s and $\Delta T_{sub} = 5$ °C, and (b) synchronized measurements of pressure drop, mass flux, and wall temperature. Images in (a) correspond to the time instances in the gray box in (b).

For a larger nominal single-phase mass flux of $G_{1\phi} = 800$ kg/m²s, the effect on the rapid-bubble-growth instability is minimal because the flow inertia is sufficient to mitigate the effects of flow reversal (as was observed at $G_{1\phi} = 400$ kg/m²s). The flow meter measured a value of zero (indicating flow reversal) for a duration of 0.015 s when $G_{1\phi} = 800$ kg/m²s, identical to the

case when $G_{1\phi}$ = 400 kg/m$^2$s. At the onset of boiling for $G_{1\phi}$ = 800 kg/m$^2$s, the wall temperature

reduced to a much lower value; there was never an increase from its initial temperature during

single-phase flow (unlike the brief increase at the onset observed for $G_{1\phi}$ = 400 kg/m$^2$s).

### 3.2.2   Effect of Inlet Liquid Subcooling

The effect of the inlet liquid subcooling on the rapid-bubble-growth instability was

studied by changing the subcooling to $\Delta T_{sub}$ = 15 °C and 35 °C while holding the nominal-single

phase mass flux constant ($G_{1\phi}$ = 400 kg/m$^2$s). Figure 3.4 shows a series of selected images at the

onset of flow boiling for a nominal single-phase mass flux of 400 kg/m$^2$s and an inlet liquid

subcooling of 15 °C, as well as the synchronized pressure drop, mass flux, and wall temperature

measurements before, during, and after the onset of boiling on a longer timescale (0 s < $t$ <

2.0 s).

Similar to the prior case at the lower inlet liquid subcooling of $\Delta T_{sub}$ = 5 °C, vapor bubble

nucleation from the channel surface (Figure 3.4; $t$ = 0.078 s) is accompanied by explosive growth

both upstream and downstream causing the vapor bubble to occupy most of the channel (Figure

3.4; $t$ = 0.092 s). A large pressure spike and a reduction in mass flux are observed (Figure 3.4b).

A zero mass flux is detected by the flow meter at $t$ = 0.089 s (Figure 3.4b), which lasts for

0.006 s, a reduction in time relative to the smaller inlet liquid subcooling of $\Delta T_{sub}$ = 5 °C (at

which the zero mass flux reading lasted for 0.015 s). As a result, a minimal wall temperature

increase of 0.5 °C is observed, from the single-phase wall temperature of 126.0 °C to a

maximum temperature of 126.5 °C at $t$ = 0.218 s. Incoming liquid then quickly replenishes the

channel (Figure 3.4; $t$ = 0.099 s) and cools (Figure 3.4b) the heated wall. The reduction in this

duration of flow reversal likely results from the relatively cool incoming liquid minimizing the

upstream propagation of the evaporating vapor-liquid interface.

After the onset of boiling, the mass flux slowly increases (~0.25 s $< t <$ ~1.55 s) while the fluid is boiling (Figure 3.4; $t = 1.061$ s and $t = 1.500$ s). Eventually, the furthest upstream portion of the vapor-liquid interface is pushed downstream (Figure 3.4; $t = 1.621$ s) and the channel transitions to a single-phase flow regime (Figure 3.4; $t = 1.640$ s). A subsequent increase in the wall temperature is observed (Figure 3.4b). This cyclical process, namely, single-phase flow, boiling incipience, rapid-bubble-growth instability, and return to single-phase flow, marks the start of time-periodic flow boiling, which is discussed in Chapter 4.

When the inlet liquid subcooling is increased further to $\Delta T_{sub} = 35$ °C, the high inlet subcooling minimizes the effect of the rapid-bubble-growth instability. While local flow reversal is still observed in the channel at the onset of boiling and results in a reduction in mass flux, the flow meter never detects a value of zero, indicating that the local flow reversal observed within the channel does not propagate upstream to the flow meter. A small increase in the wall temperature is observed shortly after the onset of boiling, similar to the cases for $\Delta T_{sub} = 5$ °C and 15 °C, before reducing to a much lower value during flow boiling conditions.
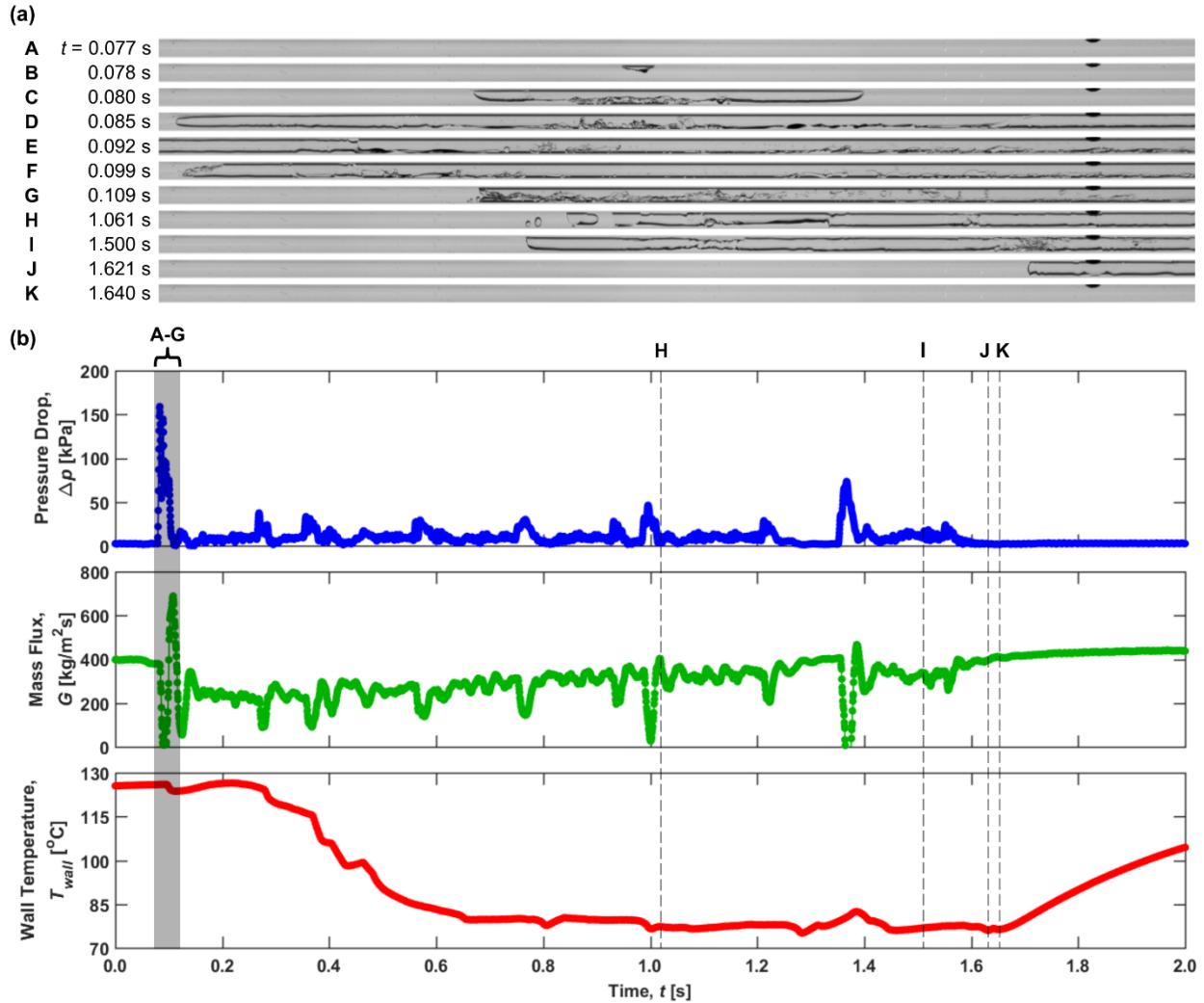
Figure 3.4. (a) Selected images of the two-phase morphology during the rapid-bubble-growth instability at the onset of boiling for $G_{1\phi} = 400$ kg/m$^2$s and $\Delta T_{sub} = 15$ °C, and (b) synchronized measurements of pressure drop, mass flux, and wall temperature. Images A-K in (a) correspond to the time instances indicated by the gray box (A-G) and dashed vertical lines (H-K) in (b).

## 3.3   Conclusions

A constant pressure source was used to deliver fluid flow through a single microchannel subjected to a uniform heat flux while synchronized high-speed flow visualization and high-frequency pressure, mass flux, and temperature measurements were acquired. This deliberate design of the hydrodynamic boundary condition closely resembles that of an individual channel

in a parallel-channel heat sink. The effects of nominal single-phase mass flux and inlet liquid subcooling on the rapid-bubble-growth instability is reported. The mechanisms underlying the rapid-bubble-growth instability, namely, large liquid superheat and a large pressure spike, were quantified and shown to result in flow reversal. Low flow inertia exacerbates the rapid-bubble-growth instability by starving the heated channel of liquid replenishment for longer durations and results in severe temperature increases. While flow reversal was also observed in the cases with high flow inertia, the wall temperature increase was minimal. The effect of the inlet liquid subcooling on the rapid-bubble-growth instability was small as indicated by the minimal increase in wall temperature. Flow reversal was observed for all three levels of subcooling, but higher subcoolings resulted in a shorter duration of flow reversal.

# 4   IMPACT OF OPERATING CONDITIONS ON INSTABILITY TYPE AND SEVERITY OF DYNAMIC MICROCHANNEL FLOW BOILING INSTABILITIES

This chapter utilizes the experimental facility described in Chapter 3 to investigate the effect of operating conditions on the instability type and the resulting time-periodic hydrodynamic and thermal oscillations, which have been established after the initial boiling incipience event. The effect of flow inertia, inlet liquid subcooling, and heat flux on the hydrodynamic and thermal oscillations and time-averaged performance is assessed. Two predominant dynamic instabilities are observed: a time-periodic series of rapid-bubble-growth instabilities and the pressure drop instability. The material from this chapter was published in *International Journal of Multiphase Flow* [64].

## 4.1   Experimental Methods

The test procedure used to capture transient data at the onset of boiling, as described in Chapter 3, was extended to investigate the flow instabilities during time-periodic boiling, after the initial boiling incipience event. Once the desired flow conditions were established, power was applied to the ITO coating on the microchannel in increments, allowing for steady-state conditions to be achieved at each set point. These small increments enable data to be collected over a range of power conditions. At low power conditions, the flow remained a single-phase

liquid; synchronized, high-frequency sensor data and IR images were recorded for 6 s once a steady-state condition was achieved. At the minimum power level required to first cause nucleation in the channel, data were recorded to capture this brief boiling onset event that was investigated in Chapter 3. At all higher power levels, sensor and imaging data were recorded for 12 s once the flow became time-periodic; these results are analyzed here in Chapter 4. The increase in power level to the test section continued until the wall temperature was high enough to saturate the IR camera sensor (~ 200 °C).

A portion of the total power supplied to the ITO coating on the microchannel is lost to the ambient. This heat loss is a function of the time-averaged wall temperature (over each data acquisition time), resulting in a different heat loss for each operating condition; $P_{loss}$ was between 9% - 49% of $P_{total}$. The power into the microchannel is calculated by subtracting the power loss from the total electric power supplied using $P_{in} = P_{total} - P_{loss}$. The time-averaged heat flux into the test section is calculated using $q_{in,avg} = P_{in} / (\pi D L_{heated})$.

The instantaneous mass flux through the test section is calculated using $G = Q\rho / (\pi D^2/4)$ where $Q$ is the measured volumetric flow rate and $\rho$ is the calculated liquid density. The inlet liquid subcooling is determined using $\Delta T_{sub} = T_{sat,out,avg} - T_{in}$ where $T_{sat,out,avg}$ is the time-averaged fluid saturation temperature corresponding to the measured pressure at the outlet of the test section and $T_{in}$ is the inlet fluid temperature. The time-averaged heat transfer coefficient is calculated using $h_{avg} = q_{in,avg} / (T_{wall,avg} - T_{ref})$, where the reference temperature ($T_{ref}$) is evaluated at the location of the wall temperature measurement; in this study, the axial position of the wall temperature measurement along the heated length of the microchannel is $(z / L_{heated}) = 0.90$. For single-phase flow, the reference temperature is defined as the liquid temperature at this location assuming a linear increase in liquid temperature from the inlet to the outlet of the microchannel:

$T_{ref} = T_{in} + (z / L_{heated})(T_{out} - T_{in})$.  For two-phase flow, the reference temperature is defined as the time-averaged local saturation temperature of the two-phase mixture at the location of the wall temperature measurement, $T_{ref} = T_{sat,avg}$.  A time-averaged local saturation pressure is calculated assuming a linear decrease in the time-averaged pressure from the inlet to the outlet of the microchannel: $p_{sat,avg} = p_{in,avg} - (z / L_{heated})(p_{in,avg} - p_{out,avg})$.  The time-averaged wall superheat is calculated using $\Delta T_{wall,sup,avg} = T_{wall,avg} - T_{ref}$.

The pressure drop across the test section is calculated as the difference between the test section inlet and outlet pressures, $\Delta p = p_{in} - p_{out}$.  The pressure drop oscillation amplitude is defined as $\Delta \tilde{p}_{osc,amp} = (\Delta p_{95} - \Delta p_5) / 2)$, where $\Delta p_{95}$ and $\Delta p_5$ are the 95th and 5th percentile of the pressure drop data recorded over the data acquisition time, respectively; this definition was chosen because it excludes occasional outlier data.  The normalized pressure drop oscillation amplitude is defined as the ratio of the oscillation amplitude to the time-averaged magnitude measured over the data acquisition time, $\Delta \tilde{p}_{osc,amp}/\Delta p_{avg}$.  This normalized oscillation amplitude will be used to quantify the pressure drop oscillations.  Analogous definitions to those shown above are used to obtain the normalized mass flux oscillation amplitude, $\tilde{G}_{osc,amp}/G_{avg}$.  These normalized oscillation amplitudes provide a better indication of the relative impact of the oscillations, making it possible to compare across different operating conditions.  A wall temperature oscillation amplitude, defined as $\tilde{T}_{wall,osc,amp} = (T_{wall,95} - T_{wall,5}) / 2)$, will be used to quantify the thermal oscillations.  These thermal oscillations can be compared across different operating conditions; thus, a normalized quantity has not been used.

Five different combinations of nominal single-phase mass flux and inlet liquid subcooling are investigated in this study, as shown in Table 4.1.  The nominal single-phase mass flux is varied, enabling the effect of flow inertia to be studied, while holding the inlet liquid

subcooling constant at $\Delta T_{sub} = 5$ °C.  Similarly, the inlet liquid subcooling is varied while

holding the nominal single-phase mass flux constant at $G_{1\phi} = 400$ kg/m²s.  The maximum heat

flux applied to the test section differed for each combination of nominal single-phase mass flux

and inlet liquid subcooling, as shown in Table 4.1, due to the sensor saturation criterion of the IR

camera used to cease testing.

Table 4.1. Operating conditions used in this study to investigate dynamic flow boiling instabilities.

| Nominal Single-Phase Mass Flux, $G_{1\phi}$ [kg/m²s] | Inlet Liquid Subcooling, $\Delta T_{sub}$ [°C] | Heat Flux, $q_{in,avg}$ [kW/m²] |
|---|---|---|
| 200 | 5 | 0 - 64.6 |
| 400 | 5 | 0 - 85.0 |
| 400 | 15 | 0 - 80.4 |
| 400 | 35 | 0 - 93.6 |
| 800 | 5 | 0 - 100.6 |

## 4.2    Results and Discussion

### 4.2.1    Time-averaged Characteristics

Figure 4.1 shows the time-averaged wall superheat, heat transfer coefficient, pressure

drop, and mass flux as a function of heat flux for the three nominal single-phase mass fluxes at a

fixed $\Delta T_{sub} = 5$ °C.  At low heat fluxes, single-phase flow is observed at all mass fluxes (denoted

with open symbols in Figure 4.1) whereas, at higher heat fluxes, time-periodic boiling is

observed (denoted with closed symbols in Figure 4.1).
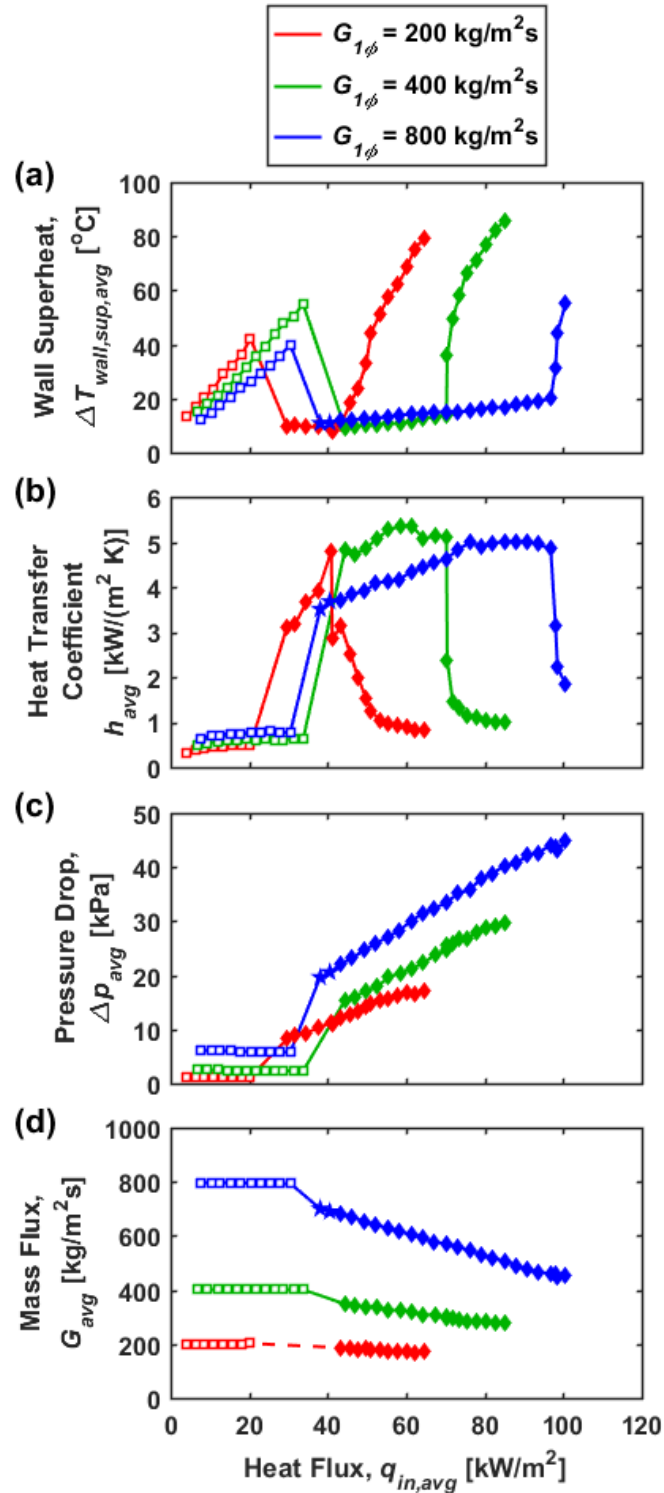
Figure 4.1. Time-averaged (a) wall superheat, (b) heat transfer coefficient, (c) pressure drop, and (d) mass flux as a function of heat flux for the three nominal single-phase mass fluxes ($G_{1\phi}$ = 200, 400, and 800 kg/m$^2$s) at a fixed inlet liquid subcooling ($\Delta T_{sub}$ = 5 °C). Open symbols denote single-phase flow and closed symbols denote time-periodic flow boiling.

The heat transfer trends in the single-phase flow regime are as expected; this regime is characterized by a wall superheat that increases linearly with increasing heat flux (Figure 4.1a), resulting in a nearly constant heat transfer coefficient (Figure 4.1b). Once boiling is initiated, the wall superheat reduces significantly, as shown by the sharp downward shift in Figure 4.1a. This reduction in wall superheat during two-phase flow results from a more efficient heat transfer process compared to single-phase flow, as indicated by the eightfold increase in the heat transfer coefficient at this transition (Figure 4.1b). Note that the reference temperature used changes between single-phase flow and two-phase flow (as explained in Section 2), but this change has a negligible influence on the aforementioned reduction in wall superheat and increase in the heat transfer coefficient. For all three nominal single-phase mass fluxes tested, there is a minimal change in the wall superheat for a large range of heat fluxes over which boiling occurs (*e.g.*, at $G_{1\phi} = 400$ kg/m$^2$s, the heat flux increases from 44.4 kW/m$^2$ to 70.2 kW/m$^2$, while the wall superheat only increases from 9.2 °C to 13.7 °C). However, at a certain heat flux in each boiling curve (Figure 4.1a), a transition is observed from a relatively low to a significantly higher wall superheat. Beyond this transitional heat flux, there is also a significant reduction in the heat transfer coefficient as observed in Figure 4.1b.

The significant increase in wall superheat observed at the transitional heat fluxes (Figure 4.1a) is attributed to local liquid-vapor interface dynamics at the point of the wall temperature measurement. At these heat fluxes, the liquid film at the wall-temperature measurement location transitions from being wavy and relatively thick at lower heat fluxes to being thin and smooth (*i.e.*, no interfacial waves) for most the data acquisition time. While a thinning liquid film is typically associated with an increasing heat transfer coefficient, this smooth film is observed to correspond to a higher wall superheat, which indicates there is likely intermittent dryout in some

locations, resulting in lower heat transfer coefficients. Further investigation of the liquid film behavior at higher-magnification imaging is required to confirm this hypothesis.

In the single-phase regime, the wall superheat at a given heat flux increases with decreasing mass flux (Figure 4.1a). Additionally, the slope of the wall superheat versus heat flux decreases with increasing mass flux (Figure 4.1a), indicative of the increased heat transfer coefficient at the higher mass fluxes (Figure 4.1b) as the hydrodynamic and thermal developing lengths increase. In the boiling regime, the wall superheat at a given heat flux is approximately the same for all three nominal single-phase mass fluxes (Figure 4.1a) and each case shows comparable heat transfer coefficients (Figure 4.1b). This indicates that the flow boiling heat transfer performance is relatively independent of flow inertia, as has been observed in microchannels when nucleate boiling heat transfer is the dominant heat transfer mechanism [25, 28, 65]. However, the transitional heat flux (point above which significant increases in wall superheat occur) is significantly different for the three different nominal single-phase mass fluxes. At $G_{1\phi} = 200$ kg/m$^2$s, large increases in wall superheat begin at $q_{in,avg} = 45.8$ kW/m$^2$ whereas, at $G_{1\phi} = 400$ kg/m$^2$s and $G_{1\phi} = 800$ kg/m$^2$s, this behavior is not observed until $q_{in,avg} = 70.5$ kW/m$^2$ and $q_{in,avg} = 98.0$ kW/m$^2$, respectively. This inertia-dependent behavior has been observed to govern the performance of two-phase heat sinks at higher heat fluxes when nucleate boiling gives way to forced convection boiling as the dominant heat transfer mechanism [25].

The time-averaged pressure drop across the test section (Figure 4.1c) can also be correlated to the single-phase and boiling regimes. During single-phase flow, the pressure drop reduces slightly with increasing heat flux due to a reduction in fluid viscosity with an increase in liquid temperature (Figure 4.1c); the pressure drop is higher at larger mass fluxes. Once boiling is initiated, the pressure drop increases by factors of 7.1, 6.8, and 3.4 compared to the single-

phase flow values, for respective mass fluxes of 200, 400, and 800 kg/m$^2$s, due to vapor generation and the associated accelerational pressure drop.  As the heat flux increases, the pressure drop increases linearly through the two-phase regime.  The pressure drop is again larger in the two-phase regime at the higher mass fluxes.

Because a constant pressure difference between the pressurized reservoir and the ambient is used to drive the flow, the instantaneous mass flux through the channel can vary with time. While the nominal single-phase mass flux provides a single reference value for each case, Figure 4.1d shows the time-averaged mass flux as a function of heat flux for the three nominal single-phase mass fluxes.  In the single-phase regime, the time-averaged mass flux is nearly constant at its nominal value with increasing heat flux due to a nearly constant pressure drop across the test section.  Once boiling occurs, the flow resistance across the test section increases and results in a reduction in the time-averaged mass flux because of the fixed pressure drop across the system (reservoir to ambient).  The time-averaged mass flux continues to drop with increasing heat flux throughout the boiling regime.  In Figure 4.1d, for $G_{1\phi}$ = 200 kg/m$^2$s, a dashed line is drawn between the last data point in the single-phase flow regime point and the first data point shown in the two-phase flow regime ($q_{in,avg}$ = 43.5 kW/m$^2$) because for the first six heat fluxes resulting in two-phase flow ($q_{in,avg}$ = 29.7 - 41.2 kW/m$^2$), the mass flux oscillations were so large that they resulted in flow reversal for extended periods of time (as will be shown later in Figure 4.7 for $q_{in,avg}$ = 37.7 kW/m$^2$).  Because the flow meter is unable to measure negative flow rates, the time-averaged mass flux could not be quantified for these six heat fluxes; hence these points were omitted from the Figure 4.1d.

Figure 4.2 shows the time-averaged wall superheat, heat transfer coefficient, pressure drop, and mass flux as a function of heat flux for the three inlet liquid subcoolings at a fixed

single-phase mass flux. The case with $\Delta T_{sub} = 5$ °C and $G_{1\phi} = 400$ kg/m²s corresponds to the same case in Figure 4.1. In the single-phase flow regime, the wall superheat is nearly identical at each heat flux for the three inlet liquid subcoolings (Figure 4.2a) resulting in nearly identical heat transfer coefficients (Figure 4.2b). The heat flux required to initiate boiling increases with increasing inlet liquid subcooling because of the larger sensible heating needed. The degree of subcooling and heat flux are shown to significantly affect the time-averaged heat transfer coefficient and wall temperature in the boiling regime. At $\Delta T_{sub} = 5$ °C, the heat transfer coefficient increases eightfold during boiling and is relatively constant until $q_{in,avg} = 70.5$ kW/m², above which it again drops to levels similar to those in the single-phase flow regime. For $\Delta T_{sub} = 15$ °C, the heat transfer coefficient only increases by a factor of 1.4 to 3.1 following boiling incipience, before reaching an eightfold increase at higher heat fluxes within the boiling regime (Figure 4.2b). Similarly, for $\Delta T_{sub} = 35$ °C, the heat transfer coefficient only increases by factors of 1.7 to 3.7 following boiling incipience, before again reaching the eightfold increase at higher heat fluxes within the boiling regime (Figure 4.2b). At even higher heat fluxes, the heat transfer coefficient drops significantly and large increases in the wall superheat are observed. The mechanisms causing these variations in the heat transfer coefficient throughout the boiling region will be discussed in Section 3.2.1.

The trends of variation of single-phase pressure drop (Figure 4.2c) and mass flux (Figure 4.2d) with heat flux are identical for the three inlet liquid subcoolings. In the boiling regime, the pressure drop increases linearly with heat flux and is accompanied by a linear reduction in the time-averaged mass flux. For a fixed heat flux in the boiling regime, the pressure drop is the largest for the smallest inlet liquid subcooling because it results in a larger axial length of the microchannel being occupied by two-phase flow. The slope of the pressure drop versus heat flux

(Figure 4.2c) curve as well as that of mass flux versus heat flux (Figure 4.2d) are approximately equal for the three inlet liquid subcoolings.
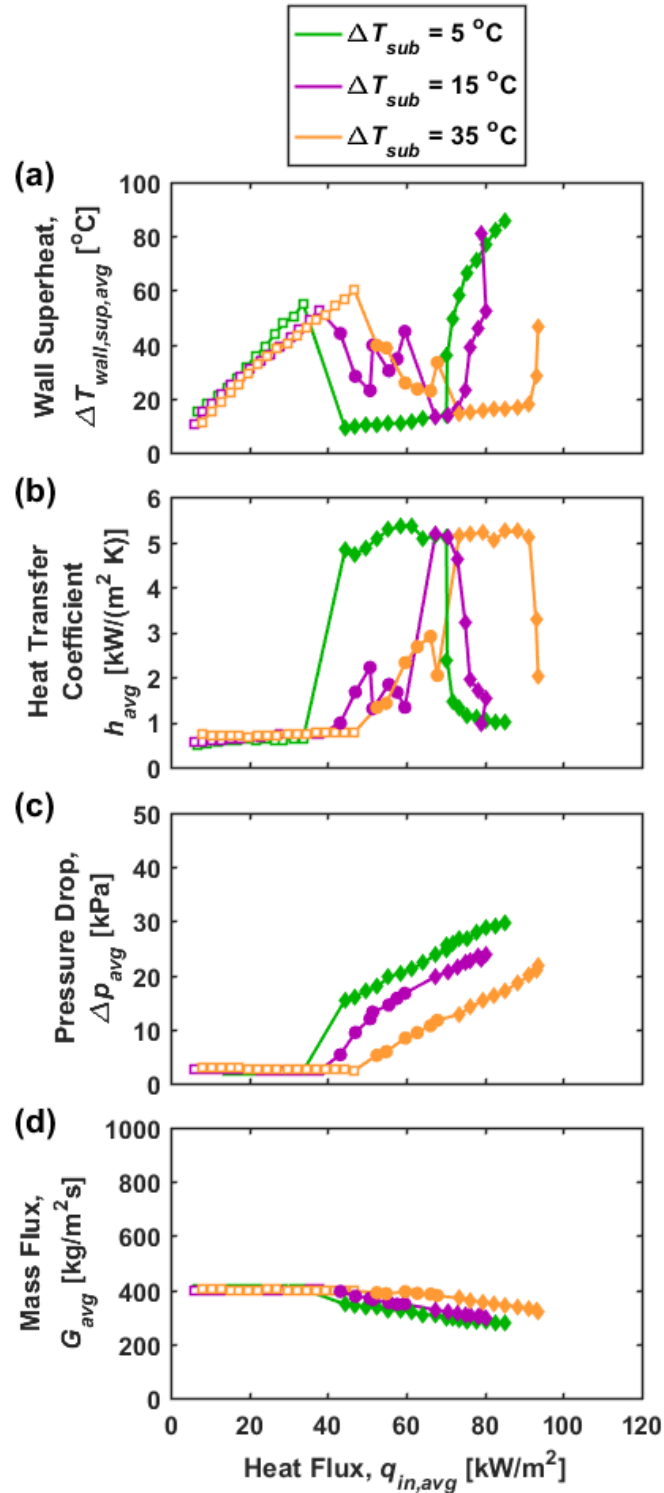
Figure 4.2. Time-averaged (a) wall superheat, (b) heat transfer coefficient, (c) pressure drop, and (d) mass flux as a function of heat flux for three inlet liquid subcoolings ($\Delta T_{sub}$ = 5, 15, and 35 °C) at a fixed nominal single-phase mass flux ($G_{1\phi}$ = 400 kg/m²s). Open symbols denote single-phase flow and closed symbols denote time-periodic flow boiling.

**4.2.2  Transient Characterization of Time-Periodic Flow Boiling Instabilities**

**4.2.2.1  Effect of Inlet Liquid Subcooling**

The type of dynamic instability observed during time-periodic flow boiling is dependent on the operating conditions.  Figure 4.3 maps the two different types of dynamic flow instabilities, *viz.*, a time-periodic series of rapid-bubble-growth instabilities and the pressure drop instability, that were observed at different levels of inlet liquid subcooling and heat flux for a fixed $G_{1\phi}$ = 400 kg/m$^2$s.  All data points shown in Figure 4.3 are for time-periodic flow boiling conditions; data points corresponding to single-phase flow have been omitted.  For $\Delta T_{sub}$ = 15 and 35 °C at low levels of heat flux ($q_{in,avg} \leq$ 59.7 kW/m$^2$ and $q_{in,avg} \leq$ 67.9 kW/m$^2$, respectively), a time-periodic series of rapid-bubble-growth instabilities was observed [denoted with circles (●) in Figure 4.3].  For the same subcoolings of $\Delta T_{sub}$ = 15 and 35 °C at higher levels of heat flux ($q_{in,avg} \geq$ 67.5 kW/m$^2$ and $q_{in,avg} \geq$ 73.5 kW/m$^2$, respectively), as well as for all heat fluxes levels at $\Delta T_{sub}$ = 5 °C, the pressure drop instability was observed [denoted with diamond symbols (♦) in Figure 4.3].  Two specific operating conditions (called out in Figure 4.3) will be described in the following paragraphs to demonstrate the characteristics of these two types of instabilities.
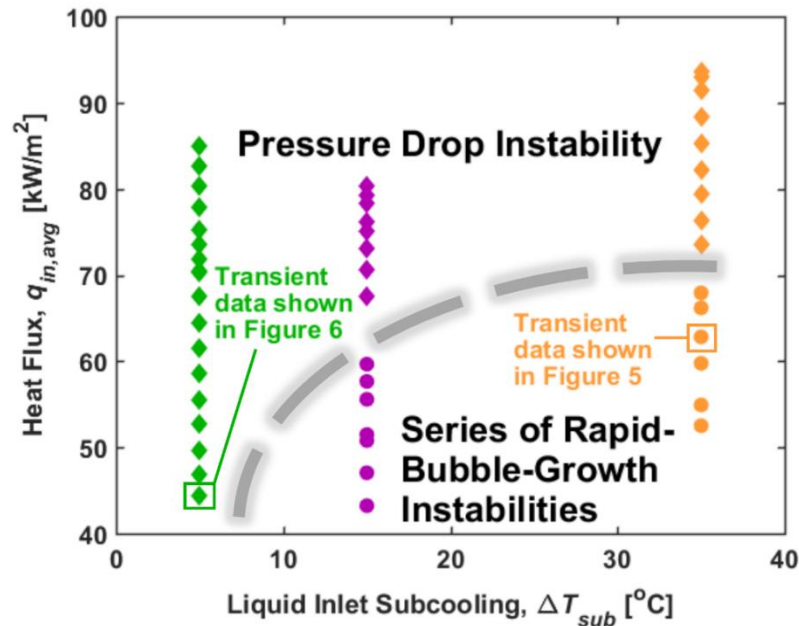
Figure 4.3.  Flow boiling instability types observed at different levels of heat flux and inlet liquid subcooling (for a fixed $G_{1\phi}$ = 400 kg/m$^2$s); the three inlet liquid subcoolings are distinguished by color.  Diamond symbols (♦) denote flow-boiling operating conditions where the pressure drop instability was observed.  Circles (●) denote flow-boiling operating conditions where a time-periodic series of rapid-bubble-growth instabilities was observed.  The dashed line demarcates the regions in which each of the two types of flow boiling instabilities are observed.

Figure 4.4a shows selected images of the two-phase morphology during one cycle of the time-periodic series of rapid-bubble-growth instabilities for $G_{1\phi}$ = 400 kg/m$^2$s, $\Delta T_{sub}$ = 35 °C, and $q_{in,avg}$ = 62.8 kW/m$^2$ (*i.e.*, orange data point highlighted in Figure 4.3).  Figure 4.4b shows the synchronized pressure drop, mass flux, and wall temperature for 4 s of the total 12 s of data acquisition time.  In Figure 4.4a, the flow is in the single-phase flow regime at $t$ = 2.373 s; the flow was in a boiling regime immediately prior to this time instant thereby resulting in a relatively low wall temperature.  The wall temperature begins increasing from 78 °C ($t$ = 2.388 s) to a maximum temperature of 109 °C ($t$ = 2.734 s) because of the significantly reduced heat transfer performance associated with single-phase flow compared to two-phase flow; the mass flux and pressure drop are steady in time.  At $t$ = 2.707 s, the wall temperature is hot enough that

it causes a small vapor bubble to nucleate from the microchannel wall. The vapor bubble grows very quickly, in both upstream and downstream directions, until it spans the entire heated length of the channel (Figure 4.4a; $t = 2.714$ s). This explosive vapor bubble growth is accompanied by a spike in the pressure drop, and the mass flux reduces to zero. The latent heat absorbed via evaporation begins cooling the microchannel wall. When the mass flux increases, it pushes the upstream portion of the two-phase interface downstream (Figure 4.4a, $2.726$ s $< t < 3.190$ s). These observations are identical to those associated with the rapid-bubble-growth instability described in Chapter 3. However, instead of transitioning into a flow regime with individual bubbles nucleating from the wall (as shown in Chapter 3 for $G_{1\phi} = 400$ kg/m$^2$s and $\Delta T_{sub} = 5$ °C), all the vapor is pushed out of the heated channel (Figure 4.4a, $t = 3.233$ s) and the relatively low wall temperature ($T_{wall} = 78$ °C) begins to increase again. Single-phase flow is observed and the process repeats. The large-amplitude, low-frequency time-periodic wall temperature oscillations shown in Figure 4.4b result from the flow transitioning between single-phase and two-phase flow. Additionally, these flow transitions result in the previously noted wall superheat and heat transfer coefficient characteristics shown in Figure 4.2a and Figure 4.2b, that yield time-averaged performance somewhere in between that of single-phase flow and two-phase flow. A large inlet liquid subcooling ($\Delta T_{sub} = 15$ or $35$ °C) causes this phenomenon to occur because the cool incoming liquid quenches the heated microchannel wall and stops the nucleation of vapor bubbles during depressurization of the upstream compressible volume.
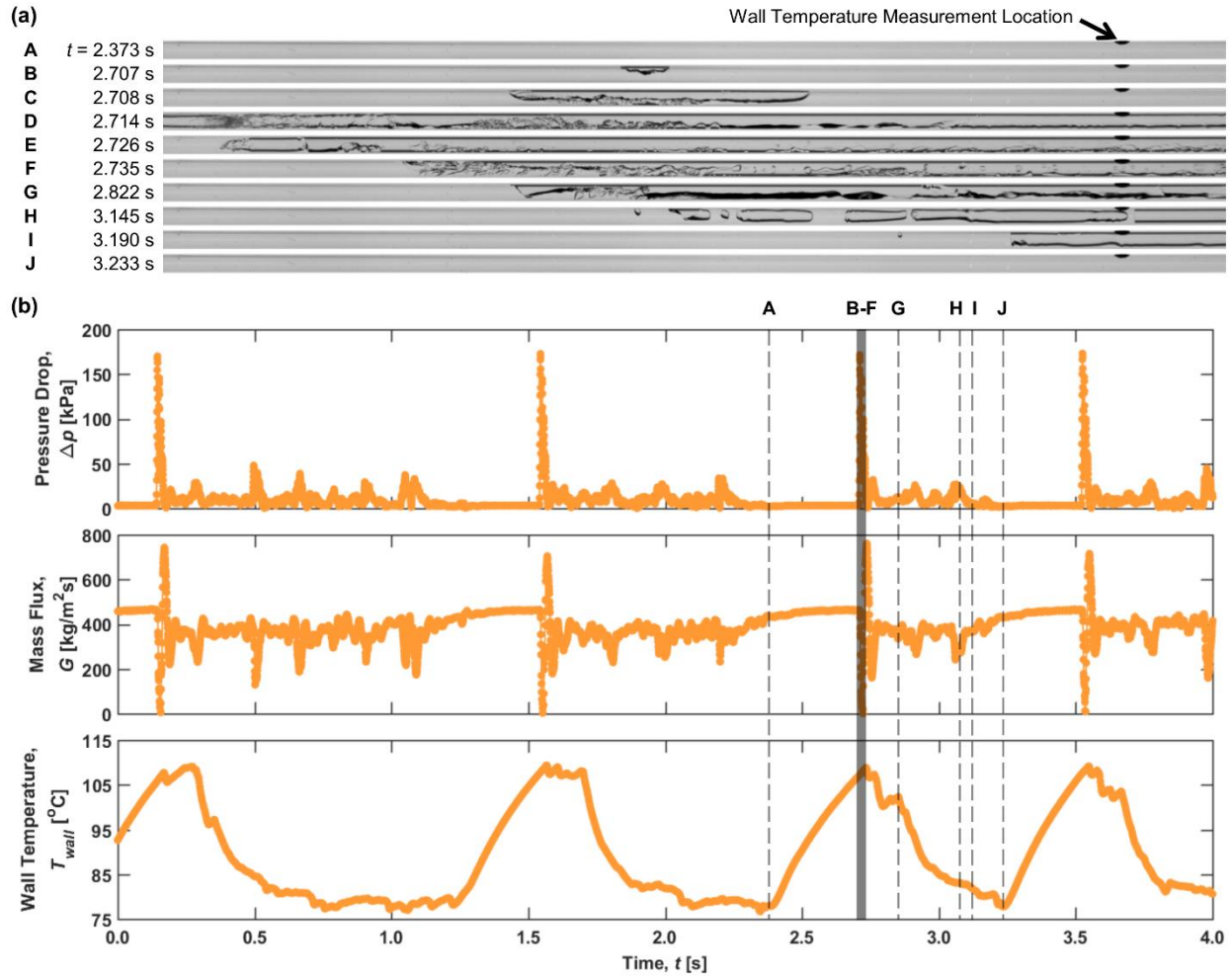
Figure 4.4. (a) Selected images of the time-periodic two-phase morphology for $G_{1\phi} = 400$ kg/m$^2$s, $\Delta T_{sub} = 35$ °C, and $q_{in,avg} = 62.8$ kW/m$^2$ (*i.e.*, orange data point highlighted in Figure 4.3) for one cycle in a series of time-periodic rapid-bubble-growth instabilities. The entire heated portion of the microchannel ($L_{heated} / D = 84$) is shown in (a). (b) Synchronized pressure drop, mass flux, and wall temperature data. The gray box in (b) correlates to the flow visualizations shown in (a).

As shown in Figure 4.3, for $q_{in,avg} \geq 67.5$ kW/m$^2$ at $\Delta T_{sub} = 15$ °C and $q_{in,avg} \geq$

73.5 kW/m$^2$ for $\Delta T_{sub} = 35$ °C, a time-periodic series of rapid-bubble-growth instabilities is no

longer observed because these larger heat fluxes allow vapor bubbles to continue to nucleate

during instances of high mass flux quenching; the pressure drop instability is observed.

Additionally, for a low inlet liquid subcooling of $\Delta T_{sub} = 5$ °C, the series of rapid-bubble-growth

instabilities is not observed for any heat flux level shown in Figure 4.3 because the incoming

liquid is much warmer and does not quench the microchannel wall; the pressure drop instability

is observed at this low inlet liquid subcooling.

Figure 4.5a shows selected images of one cycle of the time-periodic two-phase

morphology for $G_{1\phi} = 400$ kg/m$^2$s, $\Delta T_{sub} = 5$ °C, and $q_{in,avg} = 44.4$ kW/m$^2$ (*i.e.*, green data point

highlighted in Figure 4.3) observed during the pressure drop instability.  Figure 4.5b shows the

synchronized pressure drop, mass flux, and wall temperature for 0.5 s of the total 12 s of data

acquisition time.  At $t = 0.050$ s, small vapor bubbles nucleate and depart from the channel wall

and are carried downstream by the relatively high mass flux ($G \approx 400$ kg/m$^2$s); the wall

temperature is near a local minimum in the periodic signal.  As the mass flux decreases, the

reduction in flow inertia causes these small vapor bubbles to stagnate axially and begin to grow

circumferentially until they become confined and occupy most of the channel cross-section near

the nucleation site, leaving only a thin liquid layer adjacent to the channel wall (Figure 4.5a; $t =$

0.073 s).  The confined vapor bubbles grow in both upstream and downstream directions, rather

than being carried downstream after departing from the wall as did the small vapor bubbles.

Meanwhile, the mass flux in the channel decreases and the pressure drop increases to 26 kPa at

$t = 0.079$ s, because of the increased flow resistance due to additional vapor within the

microchannel.  The confined vapor bubbles grow and coalesce until the entire channel is filled

with a long continuous vapor bubble (Figure 4.5a; $t = 0.088$ s).  The wall temperature is also

higher at this time during which there is lowered mass flux.  The increase in pressure drop

(mostly attributed to an increase in the inlet pressure) causes any compressible volume upstream

of the test section to pressurize.  As a result of the reduction in mass flux, the pressure drop

reduces to 10 kPa at $t = 0.103$ s (Figure 4.5b).  As this occurs, the increased pressure gradient

between the upstream compressible volume and the microchannel results in an increase in the mass flux beginning at $t = 0.104$ s. Because the channel is virtually filled with vapor in the annular regime, the increase in mass flux results in an increase in pressure drop with negligible change in the void fraction. The wall temperature reduces along with the increasing mass flux. The pressure drop increases with increasing mass flux until the furthest upstream portion of the vapor-liquid interface begins to enter the heated portion of the channel (Figure 4.5a; $t = 0.123$ s). The reduction in the portion of the channel length occupied by vapor causes the pressure drop to decrease again even as the mass flux continues to increase. The mass flux continues to increase until it returns to a peak of 413 kg/m$^2$s at $t = 0.149$ s, when the two-phase morphology again features individual bubbles nucleating and departing from a fixed location on the inside of the microchannel wall; this is again accompanied by a relatively low wall temperature. This cyclical process then repeats. These characteristic fluctuations in the two-phase morphology, pressure drop, mass flux, and wall temperature define the pressure drop instability that occurs because of delayed interaction between the compressible volume upstream of the test section and the inertia of the flow.

For each oscillation period in Figure 4.5b, there are two peaks in the pressure drop signal for every peak in the mass flux: one larger-magnitude peak due to increased flow resistance from the presence of more vapor within the channel (despite a reduction in mass flux) and a second peak due to increased mass flux through the channel with an approximately constant amount of vapor.

**(a)**

| | |
|---|---|
| $t = 0.050$ s | |
| 0.073 s | |
| 0.075 s | |
| 0.081 s | |
| 0.088 s | |
| 0.114 s | |
| 0.123 s | |
| 0.127 s | |
| 0.150 s | |
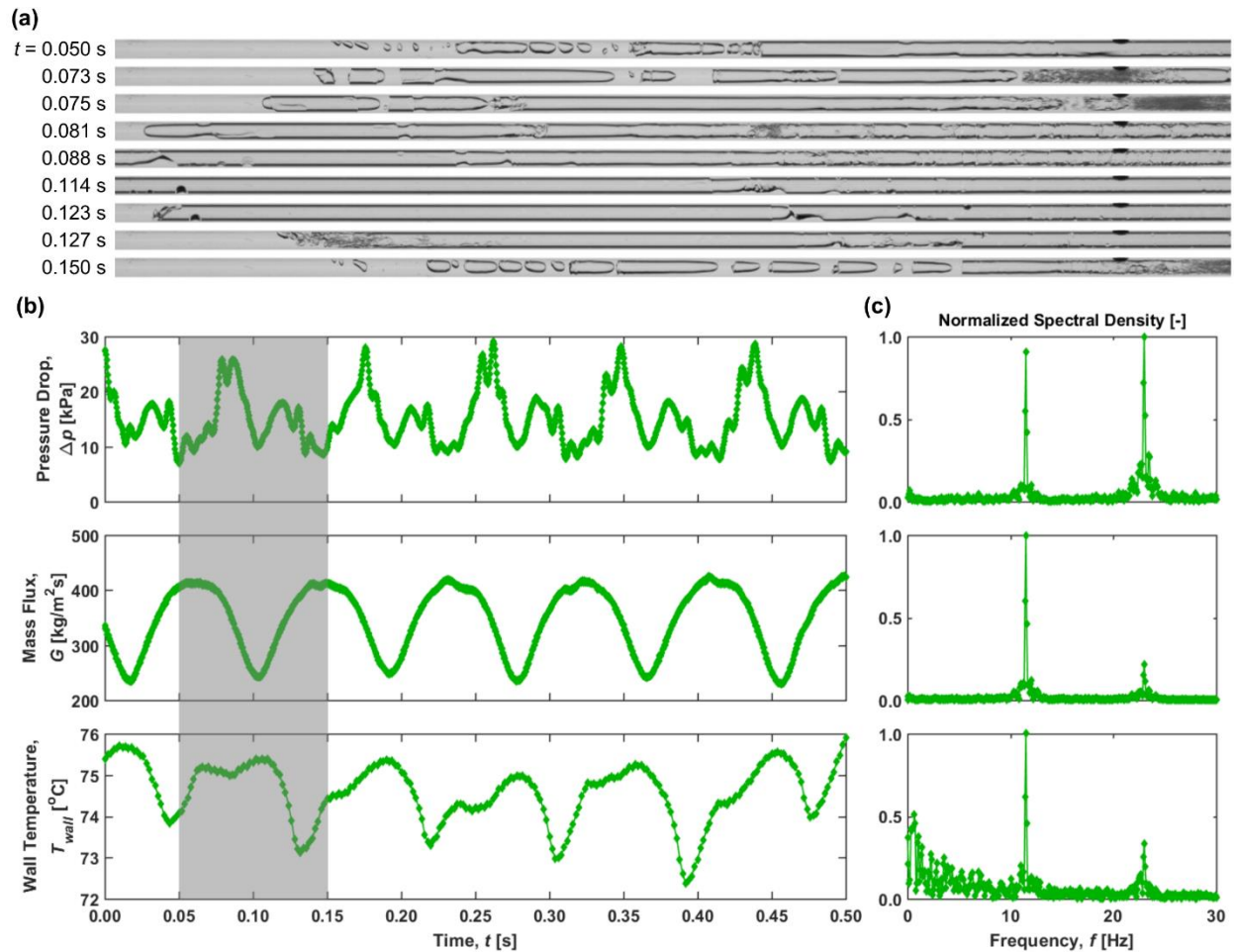


Figure 4.5. (a) Selected images showing the time-periodic two-phase morphology resulting from the pressure drop instability, (b) synchronized pressure drop, mass flux, and wall temperature fluctuations, and (c) normalized spectral density of the pressure drop, mass flux, and wall temperature data, for $G_{1\phi} = 400$ kg/m$^2$s, $\Delta T_{sub} = 5$ °C, and $q_{in,avg} = 44.4$ kW/m$^2$. The gray box in (b) correlates to the flow visualizations shown in (a).

To identify the characteristic frequencies of the time-periodic oscillations, a fast Fourier transform (FFT) is applied to the pressure drop, mass flux, and wall temperature data collected over the 12 s of total data acquisition time in each case. Figure 4.5c shows the normalized spectral density of these data for frequencies below 30 Hz (where all the spectral density is concentrated). The amplitude of the spectral density resulting from the FFT transformation is normalized relative to the maximum spectral density in each case.

In Figure 4.5c, two notable frequencies are easily identifiable at 11.5 Hz and 23 Hz. The two frequencies have nearly equal normalized spectral density magnitudes in the pressure drop signal. The flow visualizations (Figure 4.5a) showed the characteristic oscillation frequency for the pressure drop oscillations to be 11.5 Hz. The frequency of 23 Hz results from a 11.5 Hz fluctuation in pressure drop resulting from the accumulation of vapor within the channel at fixed mass flux and a 11.5 Hz fluctuation in pressure drop resulting from increased mass flux at an approximately constant void fraction within the channel, which are out of phase by one-half cycle. Thus, for this case, the 11.5 Hz oscillation frequency corresponding to characteristic pressure drop oscillations will be used for further analysis. For the mass flux and wall temperature, the spike in normalized spectral density at 11.5 Hz is significantly more dominant. In the case of the wall temperature, there are also low-magnitude, low-frequency ($< \sim 8$ Hz) oscillations that appear. However, these oscillations do not appear to be linked to flow hydrodynamics, given that they do not appear in the pressure drop or mass flux spectra.

For each combination of nominal single-phase mass flux and inlet liquid subcooling shown in Table 1, such spectral analyses were performed at each heat flux that resulted in two-phase flow. From this complete set of spectral data (not shown), a single characteristic oscillation frequency corresponding to the maximum normalized spectral density for the pressure drop, mass flux, and wall temperature was extracted, which is used as a measure to assess the effect of operating conditions on the oscillation frequency. The effect of inlet liquid subcooling on the hydrodynamic and thermal oscillations during flow-boiling operating conditions is discussed in detail in Appendix A. The level of inlet liquid subcooling is shown to have a dramatic effect on the amplitude and frequency of the hydrodynamic and thermal oscillations during flow boiling due primarily to differences in the type of flow instability that is occurring.

Specifically, the wall temperature oscillation amplitude is significantly larger for operating conditions producing a time-periodic series of rapid-bubble-growth instabilities compared to the pressure drop instability.

### 4.2.2.2   Effect of Flow Inertia

The severity of the hydrodynamic and thermal oscillations resulting from the pressure drop instability is dependent on the level of flow inertia.  For low levels of flow inertia, the oscillations are more severe whereas high levels of flow inertia moderate the amplitude of the oscillations.  The pressure drop instability can even be fully suppressed if the flow inertia is high ($G_{1\phi}$ = 800 kg/m$^2$s) and a low heat flux ($q_{in,avg} \leq 40.5$ kW/m$^2$) is supplied to the heated channel. The qualitative trend of decreasing severity of the pressure drop instability with increasing flow inertia for varying heat fluxes, at the three levels of the nominal single-phase mass flux considered in this study, is depicted pictorially in Figure 4.6, while a quantitative discussion is provided in the succeeding paragraphs and figures.
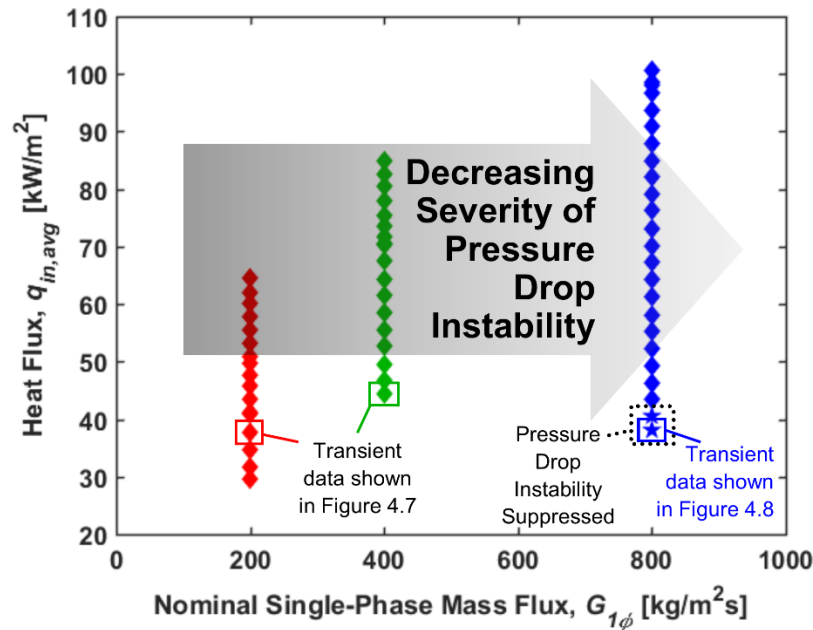
Figure 4.6. Trend of decreasing severity of the pressure drop instability with increasing flow inertia for the different heat fluxes and nominal single-phase mass fluxes (for a fixed $\Delta T_{sub}$ = 5 °C).  Diamond symbols (♦) denote flow boiling conditions where the pressure drop instability was observed.  Star symbols (★) denote flow boiling conditions where the pressure drop instability was suppressed and no other flow instabilities were observed.

The reduction in oscillation severity with increasing flow inertia is quantitatively illustrated in Figure 4.7 using synchronized pressure drop, mass flux, and wall temperature data for a low flow inertia condition of $G_{1\phi}$ = 200 kg/m²s [$\Delta T_{sub}$ = 5 °C and $q_{in,avg}$ = 37.7 kW/m² (in red)] and an intermediate flow inertia condition of $G_{1\phi}$ = 400 kg/m²s [$\Delta T_{sub}$ = 5 °C and $q_{in,avg}$ = 44.4 kW/m² (in green)] .  The pressure drop oscillations shown in Figure 4.7 for $G_{1\phi}$ = 200 and 400 kg/m²s are approximately the same, with a range of approximately 25 kPa.  However, for $G_{1\phi}$ = 200 kg/m²s, the mass flux oscillations are extreme, ranging from 0 to 938 kg/m²s, whereas for $G_{1\phi}$ = 400 kg/m²s, the mass flux oscillations are much smaller, ranging from 231 to 423 kg/m²s.  Recall from Section 3.1 that the flow meter is unable to measure negative flow rates and the signal flatlines to a mass flux of zero when there is flow reversal in the vicinity of the

flow meter for $G_{1\phi} = 200$ kg/m$^2$s.  The wall temperature oscillations for $G_{1\phi} = 200$ kg/m$^2$s are also more severe than for $G_{1\phi} = 400$ kg/m$^2$s, a direct result of the larger hydrodynamic oscillations associated with $G_{1\phi} = 200$ kg/m$^2$s.  The amplification of the hydrodynamic and thermal oscillations in the case of $G_{1\phi} = 200$ kg/m$^2$s results from the decreased flow inertia, causing a greater susceptibility to the pressure drop instability, relative to the increased flow inertia case of $G_{1\phi} = 400$ kg/m$^2$s.
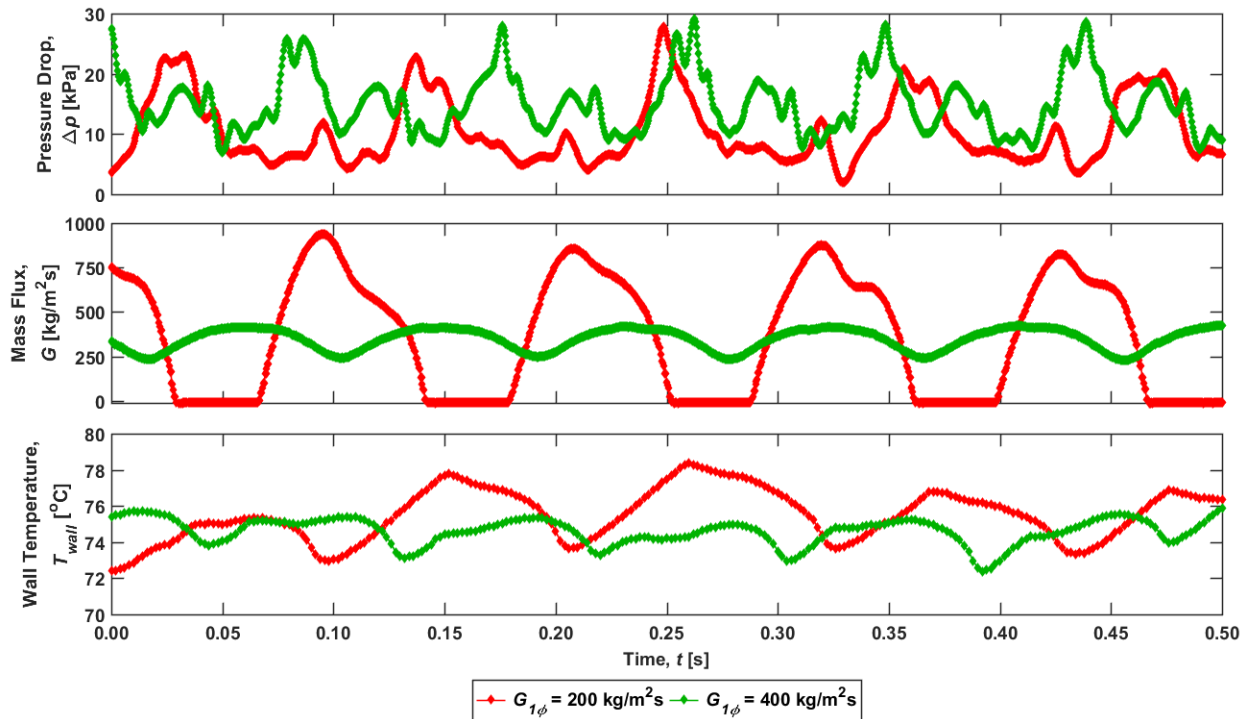


Figure 4.7. Synchronized pressure drop, mass flux, and wall temperature for $G_{1\phi} = 200$ kg/m$^2$s [$\Delta T_{sub} = 5$ °C , and $q_{in,avg} = 37.7$ kW/m$^2$ (in red)] and for $G_{1\phi} = 400$ kg/m$^2$s [$\Delta T_{sub} = 5$ °C, and $q_{in,avg} = 44.4$ kW/m$^2$ (in green)].  The data for $G_{1\phi} = 400$ kg/m$^2$s are identical to those shown in Figure 4.5, but have been replotted to enable a direct comparison to the $G_{1\phi} = 200$ kg/m$^2$s case.

While a further increase in the flow inertia from $G_{1\phi} = 400$ kg/m$^2$s to $G_{1\phi} = 800$ kg/m$^2$s did slightly reduce the severity of the pressure drop oscillations further, the effect is much smaller than the change from $G_{1\phi} = 200$ kg/m$^2$s to $G_{1\phi} = 400$ kg/m$^2$s (data for $G_{1\phi} = 800$ kg/m$^2$s are not included in Figure 4.7).  However, for the two lowest heat flux levels of $q_{in,avg} =$

38.1 kW/m$^2$ and 40.5 kW/m$^2$, the pressure drop instability was completely suppressed at $G_{1\phi}$ =

800 kg/m$^2$.  Figure 4.8a shows selected images in 0.002 s increments illustrating one periodic

cycle that depicts the nucleation, departure, and growth of a single vapor bubble that occurs

repeatedly during this operating condition.  The vapor bubble nucleates, departs almost

immediately, and grows as it flows downstream.  Local flow reversal and pressurization of the

upstream compressible volume are not observed, thus eliminating the pressure drop instability.

Figure 4.8b shows the synchronized pressure drop, mass flux, and wall temperature for a 0.5 s

period extracted from the 12 s data acquisition time; this behavior was observed throughout the

entire recording.  Owing to suppression of the pressure drop instability, the pressure drop, mass

flux, and wall temperature oscillation amplitudes are much lower compared to those shown in

Figure 4.7.  The elimination of the pressure drop instability, in this case, is a result of the

relatively increased flow inertia compared to the upstream compressibility.  At $q_{in,avg}$ ≥

43.4 kW/m$^2$, the time-averaged mass flux (and thus, flow inertia) decreases (as shown in Figure

4.1) and results in more vapor within the channel, causing compressibility to become dominant.

This leads to a transition to a flow regime featuring the pressure drop instability, like that shown

in Figure 4.5.  It is expected that at even higher nominal single-phase mass fluxes, the pressure

drop instability would be suppressed even at larger heat fluxes.

**(a)**



**(b)**
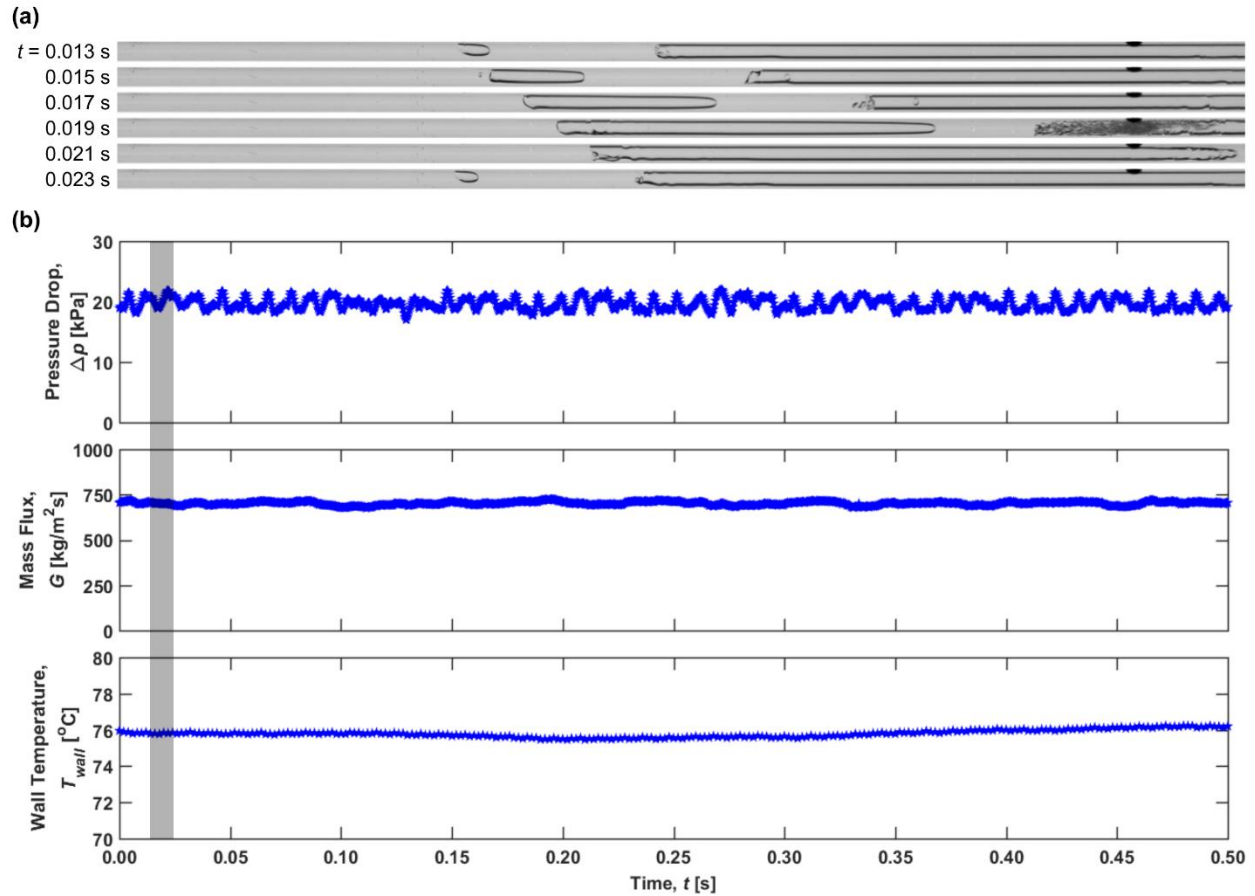


Figure 4.8. (a) Selected images showing the periodic nucleation, departure, and growth of a vapor bubble, and (b) synchronized pressure drop, mass flux, and wall temperature for $G_{1\phi} = 800$ kg/m²s, $\Delta T_{sub} = 5$ °C, and $q_{in,avg} = 38.1$ kW/m². Data are plotted on identical axes to those in Figure 4.7 to enable quantitative comparison.

The level of flow inertia significantly affects the amplitude of the hydrodynamic oscillations during flow-boiling operating conditions. Specifically, low levels of flow inertia result in large hydrodynamic oscillations because the ratio of flow inertia to upstream compressibility is smaller. A complete discussion of the effect of flow inertia on the hydrodynamic and thermal oscillation amplitudes and their characteristics frequencies during flow-boiling operating conditions is provided in Appendix B.

## 4.3    Conclusions

A constant pressure source was used to deliver fluid flow through a single microchannel subjected to a uniform heat flux while synchronized high-speed flow visualizations and high-frequency pressure, mass flux, and temperature measurements were acquired.  The effect of flow inertia, inlet liquid subcooling, and heat flux on the time-averaged hydrodynamic and heat transfer performance and the dynamic rapid-bubble-growth and pressure drop instabilities are reported.  Two different types of dynamic instabilities are observed:  (a) time-periodic transitions between single-phase and two-phase flow, which lead to a time-periodic series of rapid-bubble-growth instabilities, resulting in flow reversal and large increases in wall temperature, and (b) the pressure drop instability resulting in time-periodic pressure drop, mass flux, and wall temperature oscillations.  The characteristic frequencies of the oscillations are quantified using spectral analysis.  The parametric study enabled the following key conclusions to be drawn regarding the effect of operating conditions on the dynamic flow boiling instabilities:

Effect of inlet liquid subcooling at a constant nominal single-phase mass flux ($G_{1\phi}$ = 400 kg/m$^2$s):

- High levels of inlet liquid subcooling (*i.e.*, $\Delta T_{sub}$ = 15 and 35 °C) and low heat fluxes produce a time-periodic series of rapid-bubble-growth instabilities, resulting in large-amplitude, low-frequency wall temperature oscillations.

- The pressure drop instability is observed for (i) high levels of inlet liquid subcooling when subjected to high heat fluxes, and (ii) low levels of inlet liquid subcooling (*i.e.*, $\Delta T_{sub}$ = 5 °C) independent of the heat flux.

Effect of flow inertia at a constant inlet subcooling ($\Delta T_{sub}$ = 5 °C):

- Low levels of flow inertia exacerbate the pressure drop instability and result in more severe hydrodynamic and thermal oscillations.

- Higher flow inertia reduces the hydrodynamic and thermal oscillations associated with the pressure drop instability, and in the cases with high flow inertia ($G_{1\phi} = 800$ kg/m$^2$s) and low heat fluxes ($q_{in,avg} \leq 40.5$ kW/m$^2$), completely suppresses the pressure drop instability.

# 5   LEDINEGG INSTABILITY-INDUCED TEMPERATURE EXCURSION BETWEEN THERMALLY ISOLATED, HEATED PARALLEL MICROCHANNELS

This chapter details an experimental study that demonstrates a temperature excursion between two thermally isolated, heated parallel channels that results from the Ledinegg instability.  It is shown that boiling in one of the channels significantly increases the flow resistance due to the presence of vapor, and causes significant flow maldistribution, resulting in a large temperature increase in the boiling channel.  The material from this chapter was published in *International Journal of Heat and Mass Transfer* [66].

## 5.1   Experimental Methods

### 5.1.1   Test Facility

The custom-built experimental facility, schematically illustrated in Figure 5.1, is adapted from our previous studies of flow boiling instabilities in a single microchannel [16, 64], and uses a pressurized reservoir to deliver degassed, dielectric HFE-7100 liquid (Novec Engineered Fluid, 3M) to two parallel microchannels.  The pressure difference between the reservoir and the ambient is used to generate an open-loop flow.  The rigid stainless steel reservoir is pressurized by boiling fluid using a submerged cartridge heater (G6A-15568, Watlow).  Electrical power is supplied to the cartridge heater using an adjustable direct current power supply (XG 850W 150-

5.6, Sorensen). A constant reservoir pressure is set and maintained by adjusting the amount of power delivered to the cartridge heater.
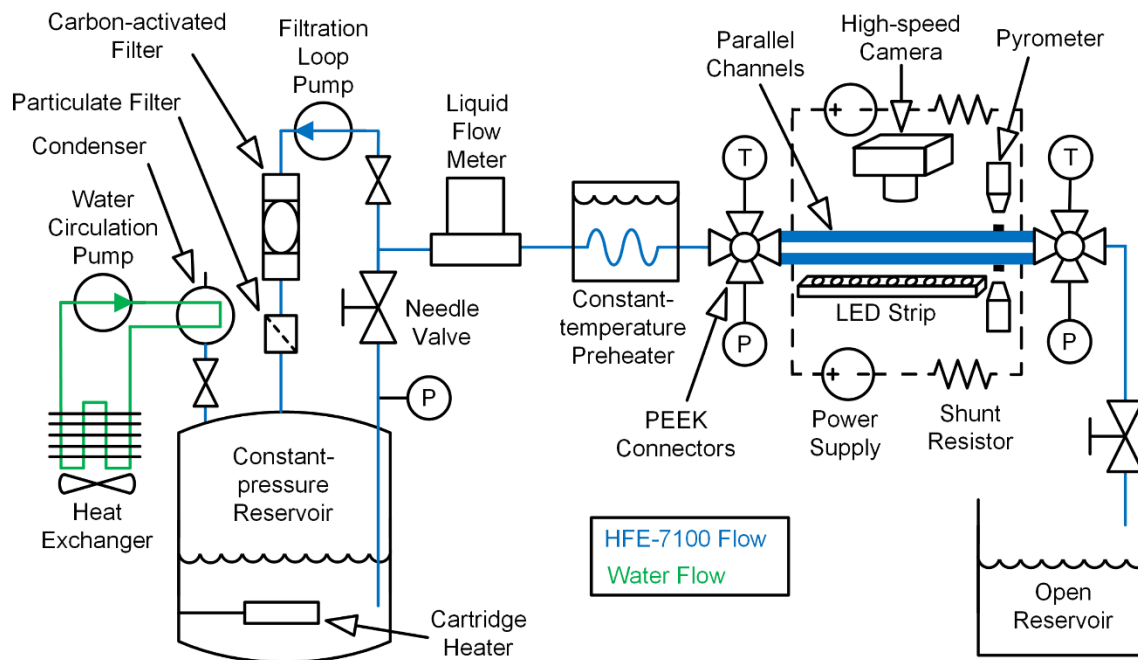


Figure 5.1. Schematic diagram of the experimental facility used to study the Ledinegg instability in two thermally isolated parallel microchannels.

Liquid is extracted from the reservoir through an internal dip tube. The liquid flow rate and the saturation pressure at the outlet of the microchannels are set using a pair of needle valves (FVL-404-SS and FVL-405-SS, Omega Engineering), one upstream and one downstream of the channels, respectively. The liquid volumetric flow rate and temperature are measured using a liquid flow meter (LC-10CCM-D-EPDM, Alicat; accuracy of ±1% full scale). The fluid is preheated to the desired inlet temperature immediately upstream of the microchannels using a constant-temperature circulating bath (NESLAB EX 17, Thermo Electron Corp.). The temperature of the fluid entering and exiting the microchannels is measured immediately upstream and downstream of the channels, respectively, using thermocouples (TMTSS-020E-6, Omega Engineering; ±0.5 °C). The pressures at the inlet and outlet of the microchannels are

measured using separate pressure transducers (PX309-030G5V and PX309-015G5V,

respectively, Omega Engineering; ±1%), and yield the pressure drop across the microchannels.

The thermocouples and pressure transducers, in addition to the fluid inlet and outlet connections,

are mounted to polyetheretherketone (PEEK) connectors (ZX2LPK, Valco Instruments) which

serve as inlet and outlet plenums, as shown in Figure 5.1; two microchannels are horizontally

mounted side-by-side in parallel between these connectors.

The two identical parallel channels are circular cross-section microchannels made of

borosilicate glass (CV5070, VitroCom) with an inside diameter of $D = 500$ μm and a wall

thickness of 100 μm.  The outside surface of the channels is custom-coated with an

approximately 100 nm-thick layer of indium tin oxide (ITO) using atomic layer deposition

(Veeco - CNT).  The ITO layer is optically transparent and electrically conductive, enabling

visualization of the two-phase flow while subjected to Joule heating.  Power is supplied to each

channel's ITO coating separately using two adjustable direct current power supplies (XG 850W

300V-2.8A, Sorensen).  The ITO layers are electrically isolated from the flow loop using non-

conductive polytetrafluoroethylene (PTFE) ferrules and PEEK nuts for attachment of the

channels to the PEEK connectors.  Any vapor leaving the channels condenses before discharging

as liquid to an open reservoir at ambient pressure.

As described in Ref. [16], pressure, mass flux, and fluid temperature measurements are

obtained using a data acquisition (DAQ) unit (USB-6259, National Instruments).  The power to

each channel is measured using a separate, high-voltage DAQ (34970A, Agilent).  The total

power (which includes power loss to the ambient) applied to each channel is quantified by

measuring the voltage drop across and current through each of the ITO-coated channels; current

measurements are obtained using two identical shunt resistors (6142-1-1000, Empro Shunts).

The entire experimental facility is mounted on a damped optical table (VIS3672-PG2-325A, Newport Corp.) to ensure that external vibrations are not transmitted to the components.

The outside wall temperature of each microchannel is measured at a single fixed location using two separate pyrometers (CTfast LT25F, Optris) coupled to focusing lenses (ACCTCF, Optris).  The pyrometers feature a small spot size of 500 μm to ensure accurate, nonintrusive temperature measurement on the outside surface of the channels without obscuring visualization of the flow.  Each pyrometer is focused on a black dot painted on the outside surface of a channel.  The axial position of the wall temperature measurement along the heated length of the microchannel is $(z / L_{heated}) = 0.91$; the heated length of the microchannel is $L_{heated} = 42$ mm.

The entire heated region of the microchannels is visualized from the top using a high-speed camera (VEO710L, Phantom) coupled to a macro lens (AF Micro-Nikkor, Nikon) using an image resolution of $1280 \times 120$.  The bottom side of the channels is uniformly backlit using a high-intensity light-emitting diode (LED) strip with an integrated light diffuser (BL168, Advanced Illumination).

### 5.1.2   Test Procedure

As described in Ref. [16], immediately prior to testing, the HFE-7100 fluid was degassed by vigorously boiling the liquid in the reservoir using the submerged cartridge heater.  Non-condensable gases are expelled, while the HFE-7100 vapor is condensed back into the reservoir (Figure 5.1).  While degassing, the HFE-7100 was also circulated through an auxiliary pumped filtration loop containing a 2 μm particulate filter (SS-4TF-2, Swagelok) and an activated-carbon filter (12011 Pall Corporation) to remove any contaminants.  After degassing and filtering, the pumps in these auxiliary loops were turned off.

Experiments were initiated by boiling the liquid in the reservoir until it reached a constant reservoir pressure of 190 kPa. Liquid flow was then initiated through the parallel microchannels at an average mass flux of 400 kg/m$^2$s while maintaining a saturation pressure of 114 kPa at the outlet of the channels by adjusting the needle valves; this corresponds to an outlet saturation temperature of $T_{sat,out} = 65$ °C. The test facility features a constant pressure drop across the system, not a constant mass flux, and thus the average mass flux through the microchannels can vary from the initial setting once boiling occurs and causes a change in the flow resistance. The constant-temperature bath setpoint was adjusted to heat the liquid to an inlet temperature of $T_{in} =$ 60 °C, resulting in an inlet liquid subcooling of 5 °C, based on the outlet saturation temperature. After establishing the desired flow conditions, power was applied to the ITO-coatings of the channels in increments, allowing for steady-state conditions to be achieved at each set point. Optical images and sensor data were then acquired at steady state for 12 s.

### 5.1.3   Data Reduction

The voltages output from the pyrometers are converted to a temperature via a calibration to a target surface featuring the same black paint as used on the microchannels. The calibration temperature was varied from 20 °C to 250 °C in 10 °C increments. A linear fit of this temperature versus voltage output is used for each pyrometer to convert the measured signal during testing to a channel wall temperature. The linear fits for the pyrometers are: $T_1 = 55.69\ V_1 - 0.35$ and $T_2 = 56.98\ V_2 - 2.36$ where $T_1$ and $T_2$ are the temperatures and $V_1$ and $V_2$ are the corresponding measured pyrometer output voltages. The coefficients of determination for both linear fits were $R^2 = 1.00$.

A portion of the total power supplied to the ITO coating on each microchannel is lost to the ambient (and not transferred to the fluid through the channel wall). This power loss was

calibrated as a function of the channel wall temperatures. The wall temperatures of both channels are measured using the pyrometers during calibration; it was observed that the power loss of an individual channel is a function of only the temperature of that channel, due to thermal isolation from the other channel. A temperature-dependent power loss equation was therefore developed for each individual channel and used to quantify the power loss during testing. The heating power being dissipated by the fluid flow inside each channel is calculated by subtracting the power loss from the total electric power supplied using $P_{in} = P - P_{loss}$; the total power supplied is calculated using $P = VI$ where $V$ is the voltage applied to the ITO coating on each channel and $I$ is the current through the ITO coating on each channel.

The heat flux into the fluid is calculated using $q_{in} = P_{in} / (\pi D L_{heated})$. The heat transfer coefficient is calculated using $h = q_{in} / (T_{wall} - T_{ref})$, where the reference temperature ($T_{ref}$) is evaluated at the location of the wall temperature measurement [$(z / L_{heated}) = 0.91$]. For single-phase flow, the reference temperature is defined as the liquid temperature at this location assuming a linear increase in liquid temperature from the inlet to the outlet of the microchannel: $T_{ref} = T_{in} + (z / L_{heated})(T_{out} - T_{in})$. For two-phase flow, the reference temperature is defined as the local saturation temperature of the two-phase mixture at the location of the wall temperature measurement, $T_{ref} = T_{sat}$. A local saturation pressure is calculated assuming a linear decrease in the pressure from the inlet to the outlet of the microchannel: $p_{sat} = p_{in} - (z / L_{heated})(p_{in} - p_{out})$. The average mass flux through the two channels is calculated as $G = Q\rho / (2\pi D^2/4)$ where $Q$ is the measured total volumetric flow rate and $\rho$ is the calculated liquid density corresponding to the measured liquid temperature at the flow meter. Note that the mass flux through each individual channel is not measured. The pressure drop across the channels is equal and is calculated as the difference between the inlet and outlet pressures, $\Delta p = p_{in} - p_{out}$.

## 5.2    Results and Discussion

Figure 5.2 shows the (a) wall temperature, (b) heat flux into the fluid, and (c) heat transfer coefficient of each microchannel as a function of total power.  At low power levels ($P =$ 0 - 2.4 W), single-phase flow is observed in both channels (marked as region I in Figure 5.2). Under single-phase flow conditions, the wall temperatures (Figure 5.2a) and heat fluxes (Figure 5.2b) of the two channels are equal (within measurement uncertainty) and increase linearly with increasing power.  An equal wall temperature at the same power indicates that both channels are receiving the same mass fluxes and thus the flow is evenly distributed by the inlet plenum.  The heat transfer coefficients for both channels are correspondingly similar at each power level and remain relatively constant with increasing power throughout the single-phase regime (Figure 5.2c).
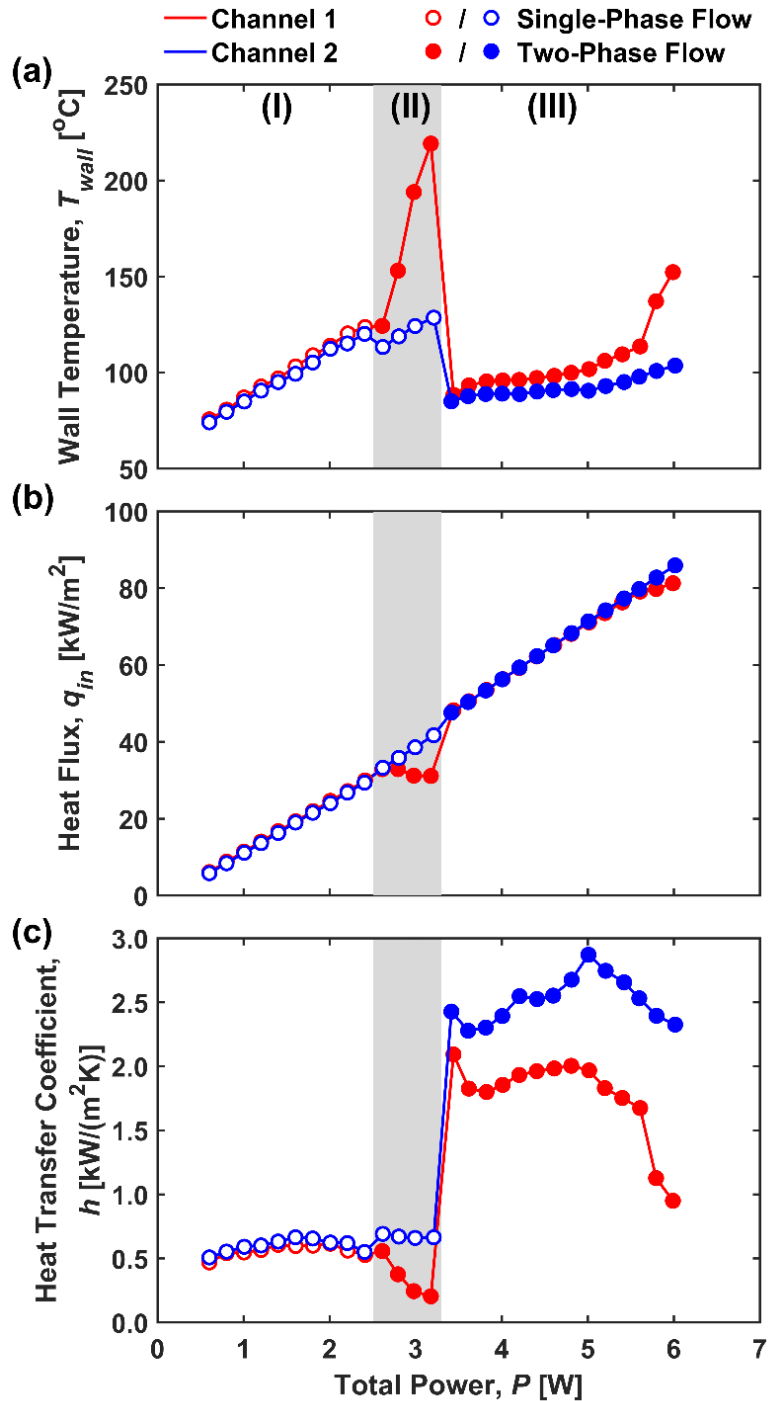
Figure 5.2. (a) Wall temperature, (b) heat flux into the fluid, and (c) heat transfer coefficient of each microchannel as a function of total power. The flow regime in each channel is denoted by the symbol type: Open symbols (○) for single-phase flow and closed symbols (●) for two-phase flow. The labeled regions indicate operating conditions where: (I) flow through both channels is single-phase, (II) boiling is occurring in channel 1 only, and (III) boiling is occurring in both channels.

At a power of $P = 2.6$ W, boiling is observed in channel 1 while channel 2 remains in the single-phase regime. After boiling incipience in channel 1, its wall temperature increases steeply with increasing power, from $T_{wall,1} = 124$ °C at $P = 2.6$ W to $T_{wall,1} = 219$ °C at $P = 3.2$ W (region II). In contrast, boiling incipience in channel 1 causes an initial reduction in the wall temperature of channel 2 (from $T_{wall,2} = 120$ °C at $P = 2.4$ W to $T_{wall,2} = 113$ °C at $P = 2.6$ W), followed by a linear increase with power (to $T_{wall,2} = 129$ °C at $P = 3.2$ W); this behavior reflects an initial increase in mass flux going to channel 2 followed by single-phase operation. The range of power that causes boiling in channel 1 and single-phase flow in channel 2 is indicated as region II (gray box) in Figure 5.2. Once boiling in channel 1 occurs (at $P = 2.6$ W), the Ledinegg instability is triggered and causes flow maldistribution between the two channels (*i.e.*, a larger mass flux through channel 2 than channel 1) and a hydrodynamic excursion with increasing power, which induces a temperature excursion. While it has been shown in the literature that the Ledinegg instability can cause a temperature difference between two thermally isolated channels [67], to the authors' knowledge, the growing difference in the wall temperature of the channels with increasing power (*i.e.*, temperature excursion between the channels) has not been previously observed in experiments.

The heat flux into channel 1 decreases slightly with increasing power throughout region II (Figure 5.2b) because the convective thermal resistance on the inside surface of the channel increases due to the worsening flow maldistribution. Meanwhile, the heat flux into channel 2 increases linearly with increasing power throughout region II. The increase in thermal resistance for channel 1 throughout region II is reflected by the decrease in the heat transfer coefficient with increasing power (Figure 5.2c). A slight increase in the heat transfer coefficient for channel 2 is observed in region II relative to region I due to the increased mass flux, which causes an increase

in the length of the channel experiencing thermally developing laminar flow.  It is important to note that the thermal isolation between the two channels, which restricts heat exchange from channel 1 to channel 2, prevents the equalization of heat flux in the two channels.

At $P = 3.4$ W, the wall temperature of channel 2 becomes large enough to cause boiling incipience in channel 2 and a significant reduction is observed in the wall temperature of both channels to $T_{wall} = 85$ °C.  The flow resistances of the two channels become approximately equal again once both experience boiling, which reduces the flow maldistribution between the two channels and suppresses the temperature excursion induced by the Ledinegg instability.  When both channels experience boiling (region III), the heat fluxes to each channel are again equal at each power level (Figure 5.2b).  The steep reduction in wall temperatures upon boiling incipience in channel 2 is reflected in the large increase seen in the heat transfer coefficients (Figure 5.2c).  The wall temperatures and heat transfer coefficients are relatively constant throughout region III until $P = 5.8$ W when the wall temperature of channel 1 begins to increase with power, likely due to intermittent dryout.

The flow in both microchannels was visualized at each power level.  Figure 5.3 shows a selected image obtained by the high-speed camera and an accompanying schematic representation of the flow regime in the two parallel channels.  The flow direction is from left to right.  The entire heated length of the channels is shown in the images; the electrical connections to the ITO coating are just outside the viewing region.  The mass flux to each channel in each of the three regions is qualitatively represented by the length of the arrows near the channel inlets. The flow visualizations captured at each power level, and those selected in Figure 5.3, enable the two-phase morphology to be identified and support the trends shown in Figure 5.2.  That is, three different regions exist depending on the operating conditions, where (I) both channels are in the

single-phase flow regime, (II) boiling is observed in channel 1 and single-phase flow is observed

in channel 2, or (III) both channels are boiling.
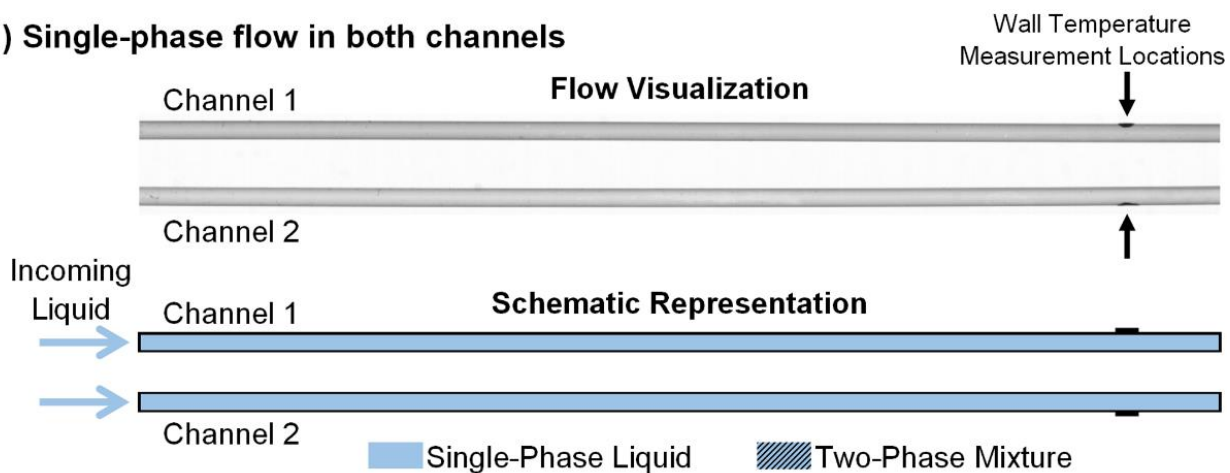


Figure 5.3. Flow visualization images and accompanying schematic representations of the flow regime observed in each channel for (I) single-phase flow in both channels, (II) boiling in channel 1 and single-phase flow is in channel 2, and (III) boiling in both channels. The flow direction is from left to right.

While the two parallel microchannels are thermally isolated, they are hydrodynamically

coupled through the same inlet and outlet plenums, resulting in a common pressure drop.

However, because of the non-monotonic nature of the channel demand curve, the mass flux

through the channels can differ significantly, even with the same pressure drop. While the mass flux through each individual channel cannot be measured, an average mass flux is measured using the upstream flow meter, thus providing an indication of the overall flow resistance of the two parallel channels. Figure 5.4 shows the (a) pressure drop and (b) average mass flux of the two channels as a function of total power. At low power levels ($P = 0$ - 2.4 W) when both channels are in the single-phase flow regime (region I), the pressure drop remains fairly constant at 2 kPa and the average mass flux through both channels is 400 kg/m$^2$s. Once boiling occurs in channel 1 at $P = 2.6$ W, the flow resistance increases and the pressure drop increases to approximately 3.5 kPa within region II. The additional flow resistance caused by boiling in channel 1 does not significantly increase the pressure drop because fluid is rerouted to channel 2, which is still in the single-phase regime. Thus, the average mass flux through the channels only reduces slightly. A minimal increase in pressure drop was also noted by Flynn *et al.* [67] when boiling occurred in only one of the two parallel channels. At $P = 3.4$ W, when boiling starts occurring in both channels, the pressure drop increases significantly to 11.7 kPa and the average mass flux reduces to 368 kg/m$^2$s. Throughout region III, the pressure drop increases with increasing power due to the increased flow resistance associated with vapor generation within both channels. As a result, the average mass flux also reduces with increasing power.

○ **Single-Phase Flow**  ● **Two-Phase Flow**

**(a)**

**(b)**
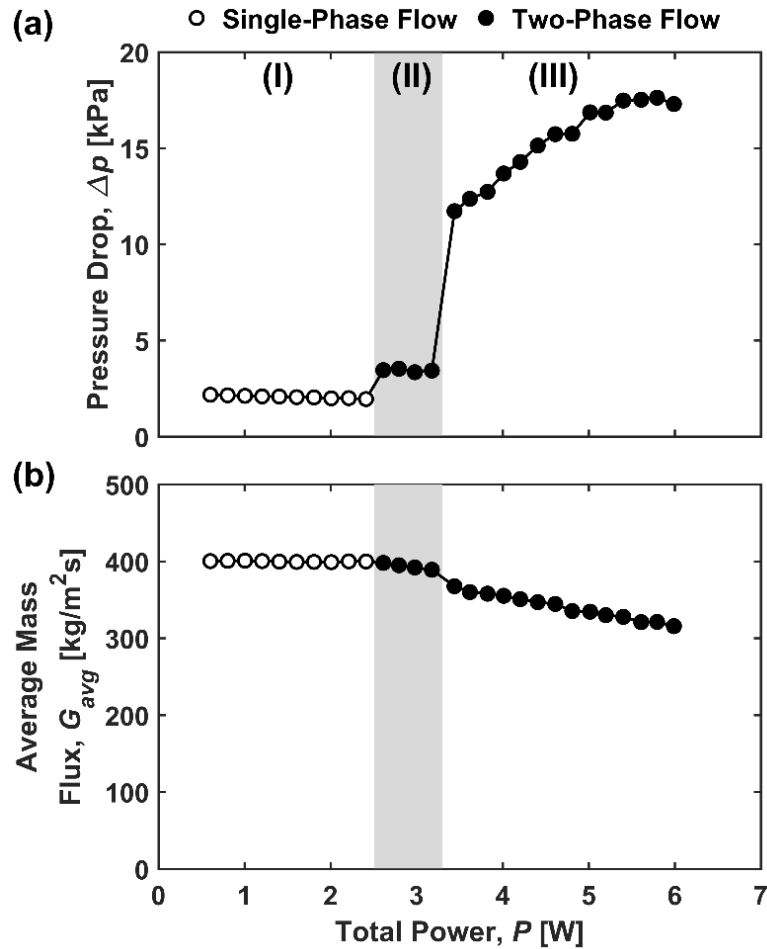
Figure 5.4. (a) Pressure drop across and (b) average mass flux through the two microchannels as a function of total power. Open symbols (○) denote single-phase flow in both channels and closed symbols (●) denote that at least one channel is boiling.

## 5.3  Conclusions

In this study, the Ledinegg instability and its influence on the thermal performance of a

parallel microchannel system are experimentally investigated. HFE-7100 liquid is delivered to

two thermally isolated parallel channels using a constant pressure source. Both channels are

uniformly subjected to the same power, which is increased in steps. High-speed flow

visualization is synchronized with pressure drop, mass flux, and wall temperature measurements.

When the flow in both channels is in the single-phase regime, the mass flux to each channel is

approximately equal. At a power level sufficient to cause boiling incipience in one of the channels, the flow resistance in that channel increases and triggers the Ledinegg instability which causes severe flow maldistribution. With increasing power to the channels, the Ledinegg instability triggers a temperature excursion, causing the wall temperature of the flow-starved channel (experiencing boiling) to increase along with a correspondingly deteriorating heat transfer coefficient. The temperature excursion continues until boiling incipience occurs in the second channel, after which the maldistribution reduces and the wall temperature of both channels reduces significantly. This study illustrates the thermal implications of the Ledinegg instability in thermally isolated parallel channels and provides new understanding of the mechanisms leading to the observed temperature excursion.

# 6 TIME-RESOLVED CHARACTERIZATION OF MICROCHANNEL FLOW BOILING DURING TRANSIENT HEATING: PART 1 – DYNAMIC RESPONSE TO A SINGLE HEAT FLUX PULSE

This chapter investigates the dynamic response of flow boiling to a single heat flux pulse using time-resolved characterization techniques. It is observed that any step up/down in the heat flux level that induces/ceases boiling, causes the temperature to temporarily over/under-shoot the eventual steady temperature.

This research is sponsored by the Naval Engineering Education Consortium (NEEC), with support of Naval Surface Warfare Center (NSWC) Crane Division in Crane, Indiana. Special thanks to Dr. Brian D. Olson (NSWC Crane Division) for technical discussion of this work.

## 6.1 Experimental Methods

### 6.1.1 Test Facility

The custom-built experimental facility, schematically illustrated in Figure 6.1, is adapted from our previous flow boiling studies [16, 64, 66], and uses a pressurized reservoir to deliver degassed, dielectric HFE-7100 liquid (Novec Engineered Fluid, 3M) to a single microchannel. The pressure difference between this reservoir and the ambient is used to generate an open-loop flow. The rigid reservoir is pressurized by boiling fluid using a submerged cartridge heater. A constant reservoir pressure is set and maintained by adjusting the cartridge heater power.
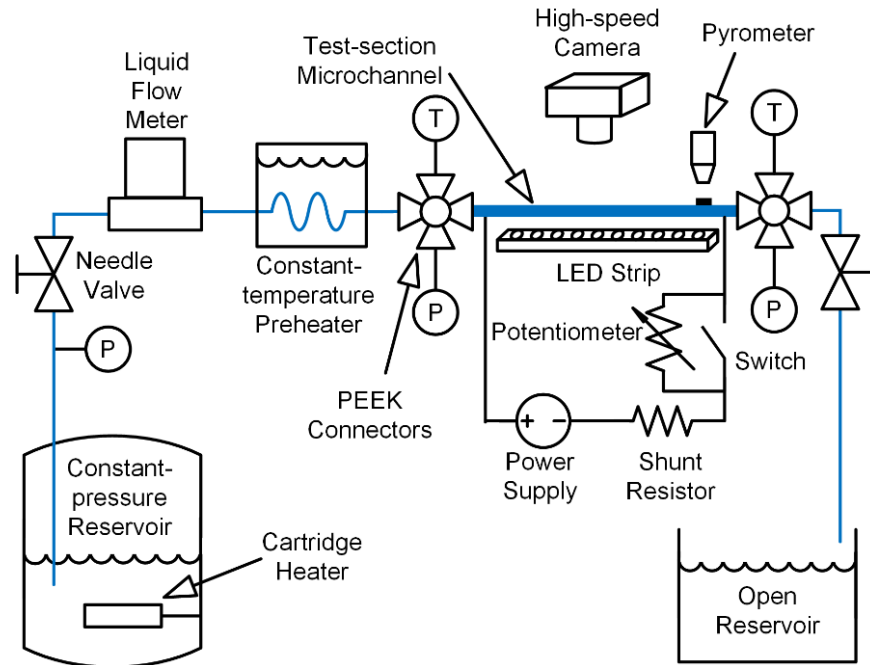
Figure 6.1. Schematic diagram of the experimental facility used to study characterize flow boiling during transient heating conditions.

Liquid is extracted from the reservoir through an internal dip tube.  The liquid flow rate and the test section outlet saturation pressure are adjusted using a pair of needle valves, one upstream and one downstream of the test section, respectively.  The liquid volumetric flow rate and temperature are measured using a liquid flow meter (LC-10CCM-D-EPDM, Alicat; accuracy of ±1% full scale).  The fluid is preheated to the desired inlet temperature immediately upstream of the test section, using a constant-temperature circulating bath.  The inlet and outlet fluid temperatures are measured immediately upstream and downstream of the test section, respectively, using small exposed-tip thermocouples (TMTSS-020E-6, Omega Engineering; accuracy of ±0.5 °C) featuring a bead diameter of ~250 μm, which enables dynamic changes in fluid temperatures to be measured.  The pressures at the inlet and outlet of the microchannel are measured using separate pressure transducers (PX309-030G5V and PX309-015G5V, respectively, Omega Engineering; accuracy of ±1%).  Short, rigid stainless steel tubes were used

to connect the pressure transducers to the polyetheretherketone (PEEK) connectors to minimize

damping and enable dynamic pressure fluctuations to be accurately measured. The pressure drop

across the test section is taken as the difference between the inlet and outlet pressure

measurements. The thermocouples and pressure transducers, in addition to the fluid inlet and

outlet connections, are mounted to the PEEK connectors, as shown in Figure 6.1; the test-section

microchannel is mounted horizontally between these connectors.

The circular cross-section microchannel is made of borosilicate glass (CV5070,

VitroCom) with an inside diameter of $D = 500$ μm and a wall thickness of 100 μm. This thin

wall thickness enables transient heating conditions to propagate to the coolant with minimal

damping and delay, as may occur in embedded two-phase heat sinks [68, 69]. The outside

surface of the microchannel has an approximately 100 nm-thick layer of indium tin oxide (ITO).

The ITO layer is optically transparent and electrically conductive, enabling visualization of the

two-phase flow while subjected to uniform Joule heating. Power is supplied to the ITO coating

using an adjustable DC power supply (XG 850W 300V-2.8A, Sorensen). The total heating

power (which includes power loss to the ambient) applied to the test section is quantified by

measuring the voltage drop across and current through the ITO microchannel coating; the current

is obtained from a shunt resistor. A solid-state switch (PAA140, IXYS Corp.) is wired in

parallel to a circuit of potentiometers (RJS10KE, RHS1K0E, RES100E; Ohmite) to allow active

switching between two different power levels and fine adjustment of the magnitudes. The switch

is activated by an output voltage signal from a high-frequency data acquisition (DAQ) unit

(USB-6259, National Instruments) that is controlled using LabVIEW. Test-section heat flux,

wall temperature, pressure drop, and mass flux measurements are obtained at 2.5 kHz using the

high-frequency DAQ unit.

The outside wall temperature of the microchannel is measured at a single fixed location using a pyrometer (CTfast LT25F, Optris) coupled to a focusing lens (ACCTCF, Optris). The pyrometer is focused on a black dot painted on the outside surface of a channel. Calibration of the pyrometer voltage output to the wall temperature is described in Ref. [66]. The axial position of the wall temperature measurement along the heated length of the microchannel is $(z / L_{heated}) = 0.91$; the heated length of the microchannel is $L_{heated} = 42$ mm.

The entire heated region of the microchannel is visualized from the top using a high-speed camera (VEO710L, Phantom) coupled to a macro lens (AF Micro-Nikkor, Nikon) using an image resolution of $1280 \times 120$ at 30,000 fps. The bottom side of the channel is uniformly backlit using a light-emitting diode (LED) strip. High-speed optical images are synchronized to heat flux, pressure drop, mass flux, and wall temperature measurements using a pulse generator (565, Berkeley Nucleonics Corp.) to simultaneously trigger the camera and high-frequency DAQ unit.

### 6.1.2 Test Procedure

As described in Ref. [16], immediately prior to testing, the HFE-7100 fluid was degassed by vigorously boiling the liquid in the reservoir using the submerged cartridge heater. Non-condensable gases are expelled, while the HFE-7100 vapor is condensed back into the reservoir (Figure 6.1). Experiments were initiated by boiling the liquid in the reservoir until it reached a constant reservoir pressure of 190 kPa. Liquid flow was then initiated through the test section at a mass flux of 400 kg/m$^2$s and a saturation pressure of $p_{sat} = 114$ kPa at the outlet of the channel; this corresponds to an outlet saturation temperature of $T_{sat} = 65$ °C. The test facility features a constant pressure drop across the system, not a constant mass flux, and thus the mass flux through the microchannel can vary from the initial setting once boiling occurs and causes a

change in the flow resistance. The constant-temperature bath setpoint was adjusted to heat the liquid to an inlet temperature of $T_{f,in} = 60$ °C, resulting in an inlet liquid subcooling of 5 °C, based on the outlet saturation temperature.

After establishing the desired flow conditions, two sets of tests were performed. First, constant heat flux was applied to the ITO-coating on the microchannel in increments, allowing for steady-state conditions to be achieved between each set point. At low heat flux conditions, the flow remained in a single phase and only sensor data was recorded. At heat flux levels resulting in boiling, sensor data and optical images were recorded. Sensor data and optical images were acquired for 12 s and the recorded data then averaged to produce time-averaged data. Next, transient heating tests were initiated. A single heat flux pulse was applied to the microchannel, defined in this study as a step change from one heat flux level to another heat flux level for a fixed time duration followed by a step change back to the original heat flux level. The heat flux levels and pulse durations chosen for this study are discussed in Section 6.2.2 and summarized in Table 6.1. For these transient tests, sensor data and optical images were recorded 2 s prior to and 10 s after the start of the heat flux pulse.

### 6.1.3   Data Reduction

A portion of the total power supplied to the ITO coating on the microchannel is lost to the ambient (*i.e.*, not transferred to the fluid through the microchannel wall). This power loss is a function of the channel wall temperature and was calibrated after testing using the procedure described in Ref. [16]. A temperature-dependent power loss equation, $P_{loss} = 0.0073\, T_{wall} - 0.1854$, is obtained and had a coefficient of determination of $R^2 = 0.97$. The instantaneous wall temperature during transient tests is used to quantify the power loss, resulting in a time-varying power loss. The net power into the microchannel is calculated by subtracting the power loss

from the total electric power supplied using $P_{net} = P_{total} - P_{loss}$; power is calculated using $P_{total} =$ $VI$ where $V$ is the voltage applied to the test section and $I$ is the current through the test section.

The instantaneous heat flux into the test section is calculated using $q_{net} =$ $P_{net} / (\pi D L_{heated})$. The time-averaged heat transfer coefficient is calculated using $h_{avg} =$ $q_{net,avg} / (T_{wall,avg} - T_{ref,avg})$, where the time-averaged reference temperature ($T_{ref,avg}$) is evaluated at the location of the wall temperature measurement $[(z / L_{heated}) = 0.91]$. For single-phase flow, the time-averaged reference temperature is defined as the liquid temperature at this location assuming a linear increase in liquid temperature from the inlet to the outlet of the microchannel: $T_{ref,avg} = T_{f,in,avg} + (z / L_{heated})(T_{f,out,avg} - T_{f,in,avg})$. For two-phase flow, the reference temperature is defined as the local saturation temperature of the two-phase mixture at the location of the wall temperature measurement, $T_{ref,avg} = T_{sat,avg}$. A local saturation pressure is calculated assuming a linear decrease in the pressure from the inlet to the outlet of the microchannel: $p_{sat} =$ $p_{in} - (z / L_{heated})(p_{in} - p_{out})$. The time-averaged wall superheat is calculated using $\Delta T_{wall,sup,avg} =$ $T_{wall,avg} - T_{ref,avg}$.

The instantaneous mass flux through the test section is calculated using $G = Q\rho / (\pi D^2/4)$ where $Q$ is the measured volumetric flow rate and $\rho$ is the calculated liquid density corresponding to the measured liquid temperature at the flow meter. The pressure drop across the test section is calculated as the difference between the test section inlet and outlet pressures, $\Delta p = p_{in} - p_{out}$.

## 6.2 Results and Discussion

### 6.2.1 Time-averaged Characterization During Constant Heating Conditions

Figure 6.2 shows the time-averaged (a) wall superheat, (b) heat transfer coefficient, (c) pressure drop, and (d) mass flux as a function of time-averaged heat flux under constant heating

conditions. At $q_{net,avg} \leq 29.7$ kW/m$^2$, single-phase flow is observed in the microchannel (denoted with open symbols in Figure 6.2) whereas at $q_{net,avg} > 29.7$ kW/m$^2$, boiling is observed (denoted with closed symbols in Figure 6.2). The trends with increasing heat flux in the single-phase flow regime are as expected; the wall superheat that increases linearly (Figure 6.2a), which corresponds to an approximately constant heat transfer coefficient (Figure 6.2b), and the pressure drop (Figure 6.2c) and mass flux (Figure 6.2d) are nearly constant.
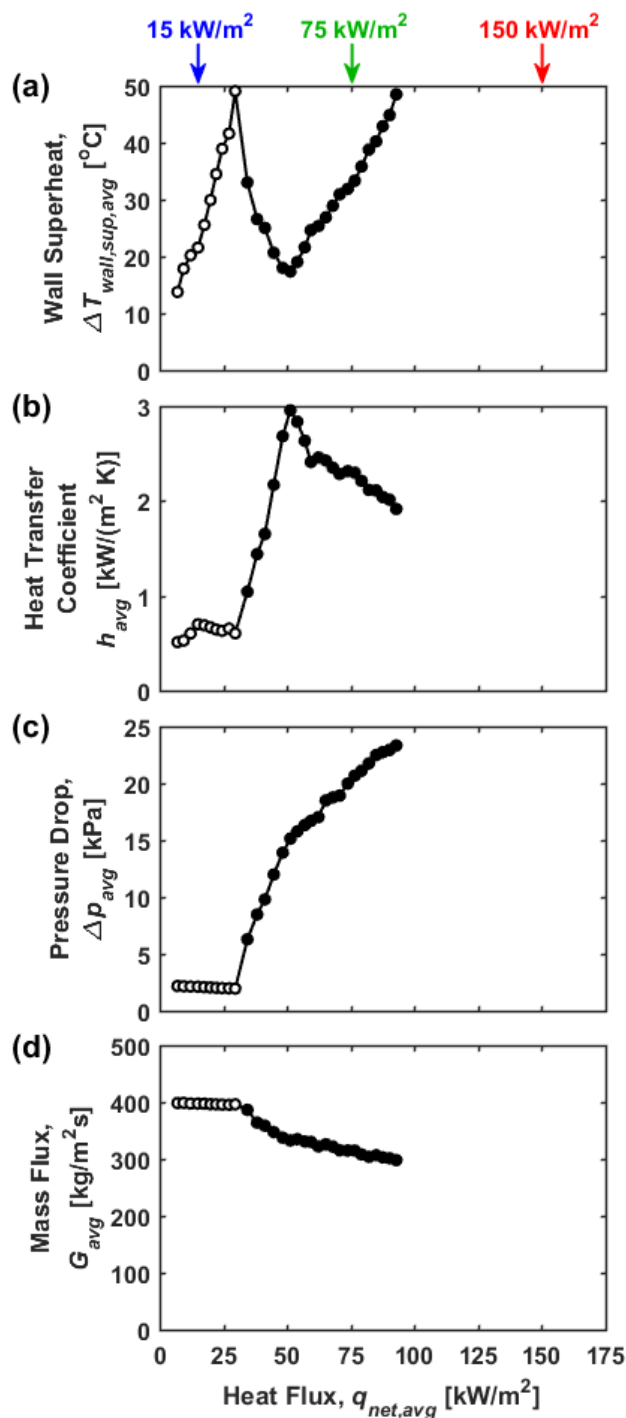
Figure 6.2. Time-averaged (a) wall superheat, (b) heat transfer coefficient, (c) pressure drop, and (d) mass flux as a function of time-averaged heat flux under constant heating conditions. Open symbols denote observation of a single-phase flow regime and closed symbols denote flow boiling. Three select heat fluxes of $q_{net,avg}$ = 15, 75, and 150 kW/m$^2$ are noted, which respectively correspond to single-phase flow, flow boiling, and a very high heat flux above critical heat flux that is unobtainable under constant heating conditions.

Once boiling is observed ($q_{net,avg} > 29.7$ kW/m$^2$), the wall superheat reduces with increasing heat flux until it reaches a local minimum of $T_{wall,avg} = 17.6$ °C at $q_{net,avg} = 51.3$ kW/m$^2$, after which it begins to increase. This trend in the wall superheat is correlated to the heat transfer coefficient, which increases with increasing heat flux once the fluid is boiling until it reaches a maximum of $h_{avg} = 3.0$ kW/(m$^2$ K) at $q_{net,avg} = 51.3$ kW/m$^2$, after which it begins to decrease. For the first five heat flux measurements that cause boiling ($29.7 < q_{net,avg} \leq 51.3$ kW/m$^2$), the flow periodically transitions between single-phase flow and two-phase flow throughout the 12 s data collection period. Throughout this span of heat inputs, the percentage of time spent in the two-phase flow regime increases monotonically with increasing heat flux, resulting in a lower time-averaged wall superheat and a higher time-averaged heat transfer coefficient. For $q_{net,avg} \geq 51.3$ kW/m$^2$, boiling is always occurring in the channel, and the observed increase in the wall superheat and decrease in the heat transfer coefficient correlates to an increase in the vapor quality. The hydrodynamic trends throughout the boiling region ($q_{net,avg} > 29.7$ kW/m$^2$) are as expected, a monotonic increase in the time-averaged pressure drop due to an increased accelerational pressure drop, and a monotonic decrease in the time-averaged mass flux through the channel, due to the increased flow resistance.

This study focuses on the effect of transient heating conditions on flow boiling performance. Of specific interest are pulses between vastly different heat flux levels that may cause flow regime transitions or other dynamic behaviors affecting the performance. For purposes of studying such transient pulses, three different heat flux levels were selected based on the time-averaged data shown in Figure 6.2 to exhibit highly contrasting flow conditions: a low heat flux corresponding to single-phase flow ($q_{net,avg} = 15$ kW/m$^2$), an intermediate heat flux corresponding to continuous flow boiling ($q_{net,avg} = 75$ kW/m$^2$), and a very high heat flux which

would cause critical heat flux if operated at this level continuously ($q_{net,avg} = 150$ kW/m$^2$).  These three selected heat flux levels are illustrated relative to the time-averaged heat transfer and hydrodynamic behavior in Figure 6.2.

### 6.2.2   Characterization During Transient Heating Conditions

Four different operating scenarios (*i.e.*, combinations of initial and pulsed heat flux levels) are obtainable based on the three selected heat flux levels, as shown in Table 6.1.  Note that the heat flux cannot be initially constant at 150 kW/m$^2$ because it would result in critical heat flux; this heat flux level can only be sustained for brief time periods as the pulsed heat flux. For operating scenarios 1 and 2, where the initial and pulsed heat fluxes switch between 15 kW/m$^2$ and 75 kW/m$^2$, the pulse durations range from 0 to 10 s. This range spans from conditions with no heat flux pulse (0 s pulse duration) to effectively a step change in the heat flux level because the flow reaches a new steady-state condition by the end of the 10 s pulse.  For operating scenarios 3 and 4, where the heat flux is pulsed to 150 kW/m$^2$, the pulse duration was increased from zero in 0.05 s increments until the wall temperature measured during the transient event neared a limit of 200 °C (which corresponded to pulse durations of 0.35 and 0.50 s for operating scenarios 3 and 4, respectively).  To illustrate the dynamic response to a transient heat flux pulse, the maximum pulse duration tested for each of the four operating scenarios will be shown in Figure 6.3-Figure 6.6.  Results for several shorter pulse durations for each operating scenario are shown in Appendix C.

Table 6.1.  Operating scenarios and pulse durations used in this study to perform the transient heating tests.

| Operating Scenario | Initial Heat Flux [kW/m²] | Pulsed Heat Flux [kW/m²] | Pulse Durations [s] |
|---|---|---|---|
| 1 | 15 | 75 | 0 - 0.50*, 0.75, 1, 2, 4, 6, 8, 10 |
| 2 | 75 | 15 | 0 - 0.50*, 0.75, 1, 2, 4, 6, 8, 10 |
| 3 | 15 | 150 | 0 - 0.35* |
| 4 | 75 | 150 | 0 - 0.50* |

* Increments of 0.05 s

Figure 6.3a shows the heat flux, wall temperature, pressure drop, and mass flux as a function of time for the heat flux pulse from 15 to 75 kW/m². At $t = 0$ s (start of the pulse), the wall temperature increases quickly until it reaches 105 °C at $t = 0.172$ s, which causes the fluid inside the microchannel to boil. Once boiling, the wall temperature remains fairly steady until approximately $t = 0.5$ s, at which point it begins to increase again until it reaches a maximum wall temperature of 120 °C at $t = 0.688$ s. Thereafter, the wall temperature slowly reduces until it assumes time-periodic behavior after approximately $t = 2.5$ s. It is important to note that during this transition from constant heating at 15 to 75 kW/m², the wall temperature spikes approximately 20 °C higher than the time-averaged wall temperature observed at 75 kW/m² at $t > 2.5$ s. This result demonstrates the critical potential effects of transient changes in heating conditions on flow boiling performance, which can induce wall temperatures excursions during flow transitions events that exceed the bounding limits expected of steady performance.

Like that of the wall temperature, the onset of boiling also causes a dynamic response in the pressure drop and mass flux before transitioning to a time-periodic condition at $t > 2.5$ s, where there are abrupt, time-periodic spikes in the pressure drop and corresponding dips in the mass flux. These result from the pressure drop instability that occurs during boiling due to the interaction between vapor within the channel and compressible volume upstream of the test

section.  An exhaustive characterization and discussion of the pressure drop instability during constant heating conditions was provided in Ref. [64].
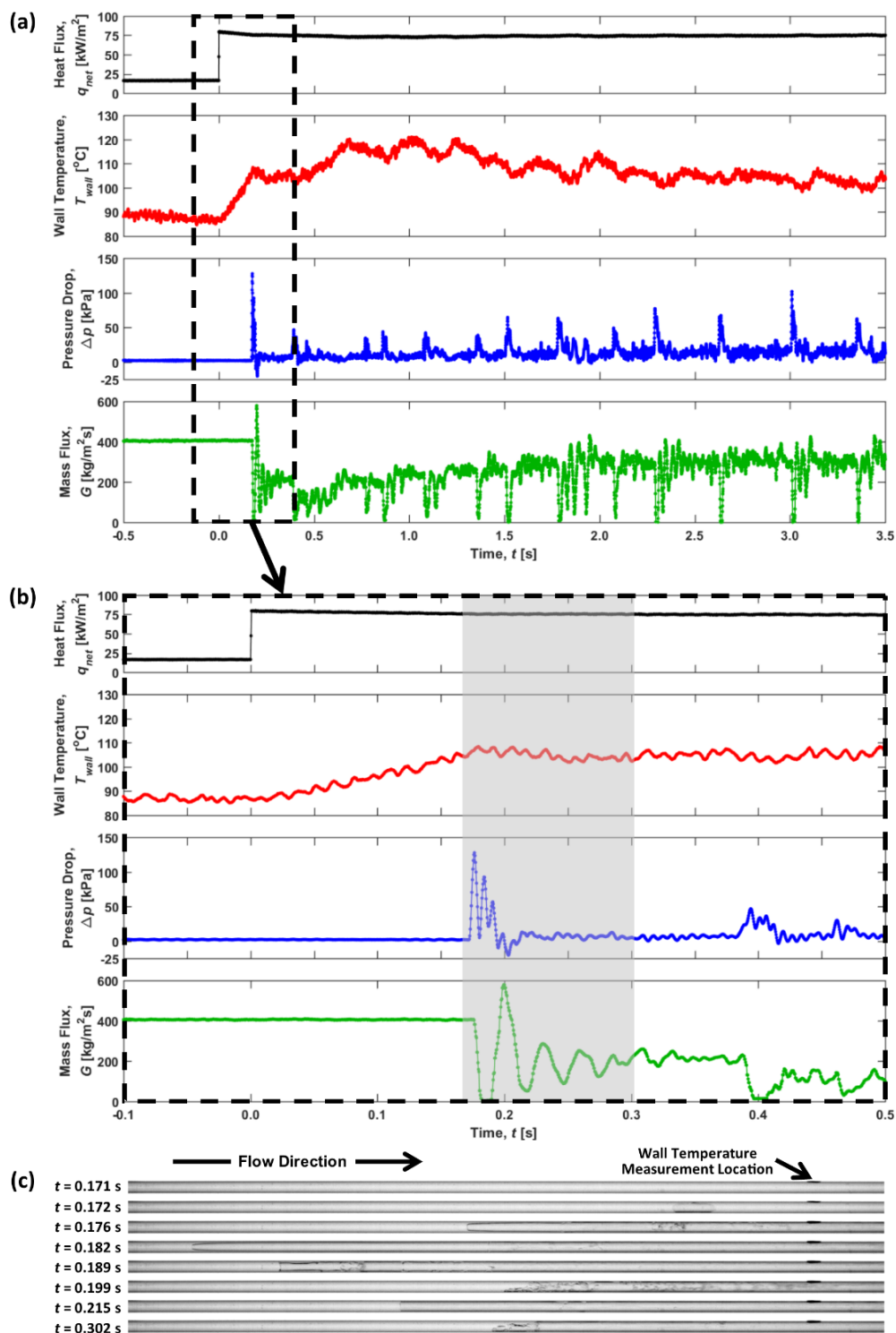
Figure 6.3. Synchronized measurements of heat flux, wall temperature, pressure drop, and mass flux as a function of time for (a) -0.5 to 3.5 s and (b) -0.1 to 0.5 s relative to the start of a 10 s heat flux pulse from 15 to 75 kW/m$^2$ (operating scenario 1). (c) Selected images of the two-phase morphology are shown that correspond to the time period indicated by the gray box in (b).

Further investigation into the pressure drop, mass flux, and two-phase morphology immediately after the onset of boiling reveals the dynamic response of the system. Shown in Figure 6.3b are the sensor measurements immediately before and after the heat flux pulse at $t = 0$ s. A series of selected images obtained by the high-speed camera from $t = 0.171$ - $0.302$ s are shown in Figure 6.3c, which correspond to the gray shaded region in Figure 6.3b. The flow direction in Figure 6.2c is from left to right. The entire heated length of the microchannel ($L_{heated}$ / $D = 84$) is shown in the frame; the electrical connections to the ITO coating are just outside the viewing region. The small black dot visible in each image, on the top portion of the channel near the outlet, is the location of the wall temperature measurement. Immediately following vapor bubble nucleation from the microchannel wall at $t = 0.172$ s, a large spike in the pressure drop to ~128 kPa and a corresponding reduction in the mass flux to zero is observed. This pressure drop spike results from explosive-like growth of the vapor bubble, a characteristic of the rapid-bubble-growth instability at the onset of boiling [16]. Rapid bubble growth within the channel results in local flow reversal, as shown in Figure 6.3c from $t = 0.172$ - $0.182$ s, and pressurization of the upstream compressible volume. The pressure drop then reduces and is followed by a surge in the mass flux to 579 kg/m$^2$s (well above the initial mass flux of 400 kg/m$^2$s during single-phase flow) due to depressurization of the upstream compressible volume, which pushes the vapor in the channel downstream, as shown in Figure 6.3c at $t = 0.189$ and 0.199 s. Oscillations in the pressure drop, mass flux, and two-phase morphology are observed thereafter, which decay in magnitude over time and eventually transition to the time-periodic boiling conditions described above and shown in Figure 6.2a. This oscillatory behavior immediately following the onset of boiling is qualitatively similar to the dynamic response of an underdamped mass-spring-damper system subjected to a unit step input. This response is due to

the complex interaction between the inertia of the flow, upstream compressibility, and vapor within the channel, which to date is poorly understand. Observing and quantifying the dynamic response during this transient event provides new insights into the governing mechanisms that may lead to predictive mechanistic modeling capabilities.

Operating scenario 2 probes the transient response during a transition from two-phase flow to single-phase flow. Figure 6.4a shows the heat flux, wall temperature, pressure drop, and mass flux as a function of time for the heat flux pulse from 75 to 15 kW/m$^2$. Prior to the start of the pulse, the fluid in the channel is boiling and the pressure drop instability is occurring, resulting in time-periodic fluctuations in the wall temperature, pressure drop, and mass flux. Time-periodic oscillations in the vapor front, which moves upstream and downstream in the channel as shown in Figure 6.4b from $t = $ -0.113 to 0 s, are characteristic of the pressure drop instability. At $t = 0$ s (start of the pulse), the wall temperature decreases and the vapor front moves downstream (Figure 6.4b; $t = 0$ to 0.348 s). During this time period, there is a continual reduction in the pressure drop and a corresponding increase in the mass flux through the channel, as shown in Figure 6.4a. Once the vapor moves downstream of the location of the wall temperature measurement (which occurs at $t = 0.339$ s), the wall temperature begins to rise until it reaches 90 °C; this correlates to the reduced heat transfer coefficient for single-phase flow relative to two-phase flow at a given heat flux level. Similar to the onset of boiling, when the flow transitions from two-phase to single-phase flow, the wall temperature does not monotonically transition from one operating condition to another, but instead undershoots its eventually operating point and features a larger thermal fluctuation during this transient event.
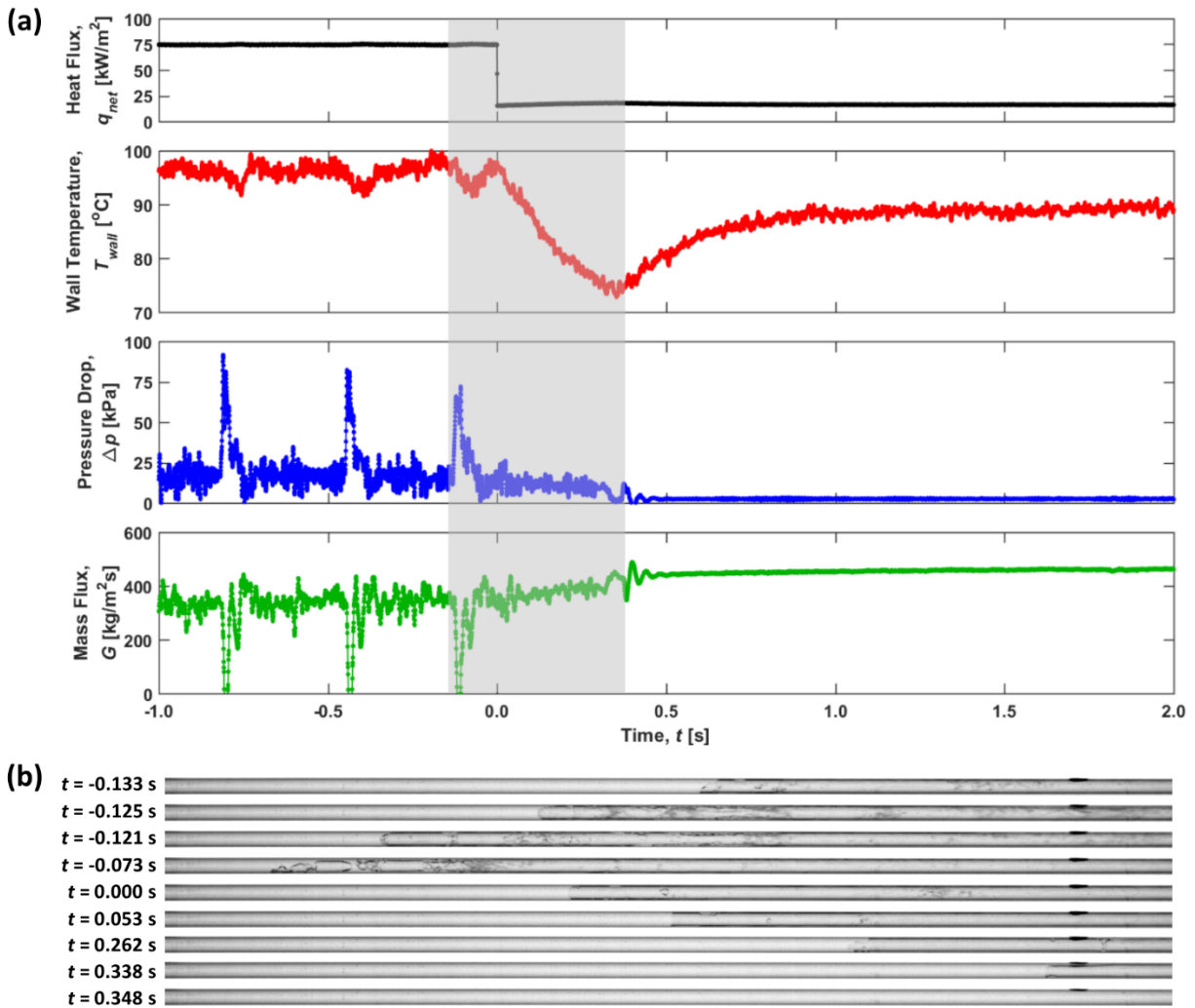
Figure 6.4. (a) Synchronized measurements of heat flux, wall temperature, pressure drop, and mass flux as a function of time for -1 to 2 s relative to the start of a 10 s heat flux pulse from 75 to 15 kW/m$^2$ (operating scenario 2). (b) Selected images of the two-phase morphology are shown that correspond to the time period indicated by the gray box in (a).

In many applications, short high-heat-flux pulses are encountered that are above the heat fluxes that could be sustained by the cooling system during steady operation. It is critical to assess the response of the cooling system to these transient heat flux pulse events. Figure 6.5a shows the heat flux, wall temperature, pressure drop, and mass flux as a function of time for a 0.35 s heat flux pulse from 15 to 150 kW/m$^2$. Prior to the pulse, the wall temperature, pressure

drop, and mass flux are steady and the flow is single-phase. Once the pulse begins, the wall

temperature increases until fluid in the channel begins boiling near the outlet (Figure 6.5b; $t =$

0.047 s). Nucleation of a vapor bubble causes a large pressure spike within the channel, leading

to a sharp reduction in the mass flux. The high heat flux causes the vapor within the channel to

expand quickly and move upstream until most of the channel is full of vapor (Figure 6.5b; $t =$

0.178 s). A underdamped dynamic response, similar to that noted alongside Figure 6.3, can be

observed in the flow visualizations and sensor measurement between approximately $t = 0.04$ -

0.1 s. While the heat flux is pulsed, the expanding vapor within the channel induces a large flow

resistance which causes the mass flux through the channel to be extremely low ($< 100$ kg/m$^2$s)

and the wall temperature to rise. A thin liquid layer is observed to remain wetted on the

microchannel wall, which suggests that the temperature rise is due to a lack of incoming liquid

that suppresses the forced convective boiling heat transfer mechanism; it is not due to dryout

(*i.e.*, vapor contacting the heated wall). After the heat flux pulse ends at $t = 0.35$ s, the wall

temperature, pressure drop, mass flux gradually return to their initial levels before the pulse and

vapor is no longer present in the channel. At $t = 1.5$ s, an inflection point in the reducing wall

temperature is observed, corresponding to a local change in the two-phase morphology near the

location of the wall temperature measurement. Specifically, the liquid annulus adjacent to the

wall thickens, which could allow for bubble nucleation and changes in the heat transfer

mechanisms.
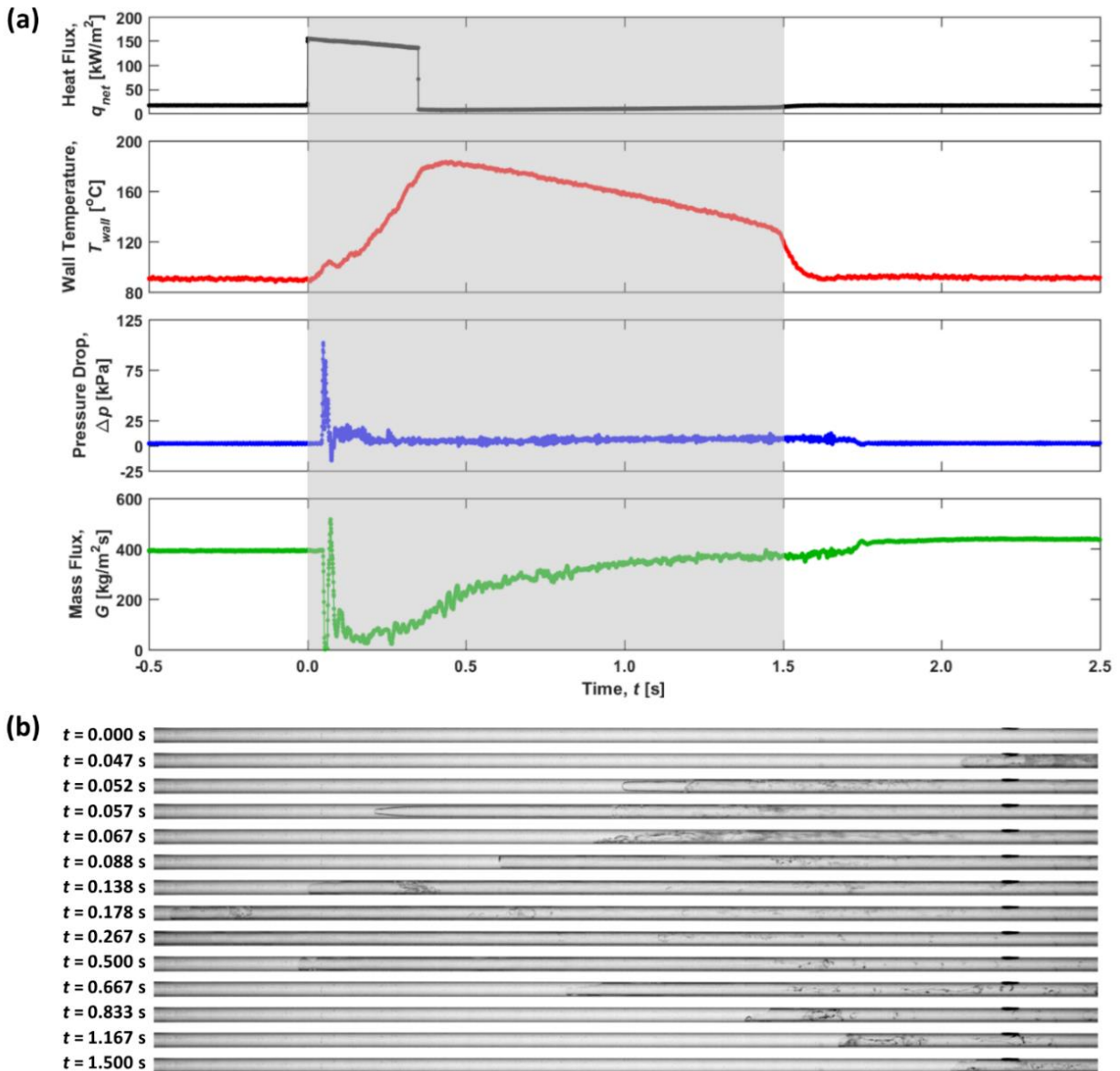
Figure 6.5. (a) Synchronized measurements of heat flux, wall temperature, pressure drop, and mass flux as a function of time for -0.5 to 2.5 s relative to the start of a 0.35 s heat flux pulse from 15 to 150 kW/m$^2$ (operating scenario 3). (b) Selected images of the two-phase morphology are shown that correspond to the time period indicated by the gray box in (a).

Figure 6.6a shows the heat flux, wall temperature, pressure drop, and mass flux as a function of time for a 0.5 s heat flux pulse from 75 to 150 kW/m$^2$. Prior to the pulse, from $t = -0.5$ to 0 s, the fluid in the channel is boiling and there are time-periodic pressure drop oscillations. The frequency of these oscillations is 4 Hz, as determined through spectral analysis

of the sensor measurements using a fast Fourier transform. When the pulse begins at $t = 0$ s, the

wall temperature begins to rise and the vapor front within the channel moves upstream until it is

very close to the entrance of the heated region, as shown in Figure 6.6b at $t = 0.279$ s.

Throughout the pulse, time-periodic fluctuations in the pressure drop and mass flux

measurements are again observed, but the frequency of the oscillations is significantly increased

to 29 Hz. The increased frequency is due to the vapor front being located near the channel inlet,

reducing the axial distance the vapor front needs to travel to move upstream into the inlet plenum

during the pressure drop oscillations. One cycle of the time-periodic two-phase morphology

observed during the high-frequency pressure drop oscillations that occur during the heat flux

pulse is shown in Figure 6.6b, and is indicated by the gray box in Figure 6.6a. It is worth noting

that a 150 kW/m$^2$ heat flux pulse is sustained for 0.5 s with a wall temperature below the 200 °C

limit when boiling was initially occurring within the channel at $q_{net} = 75$ kW/m$^2$, whereas only a

0.35 s pulse could be sustained when the flow was initially single-phase at $q_{net} = 15$ kW/m$^2$. This

occurs despite wall temperature being slightly higher for the initially boiling scenario than for the

initially single-phase flow scenario.
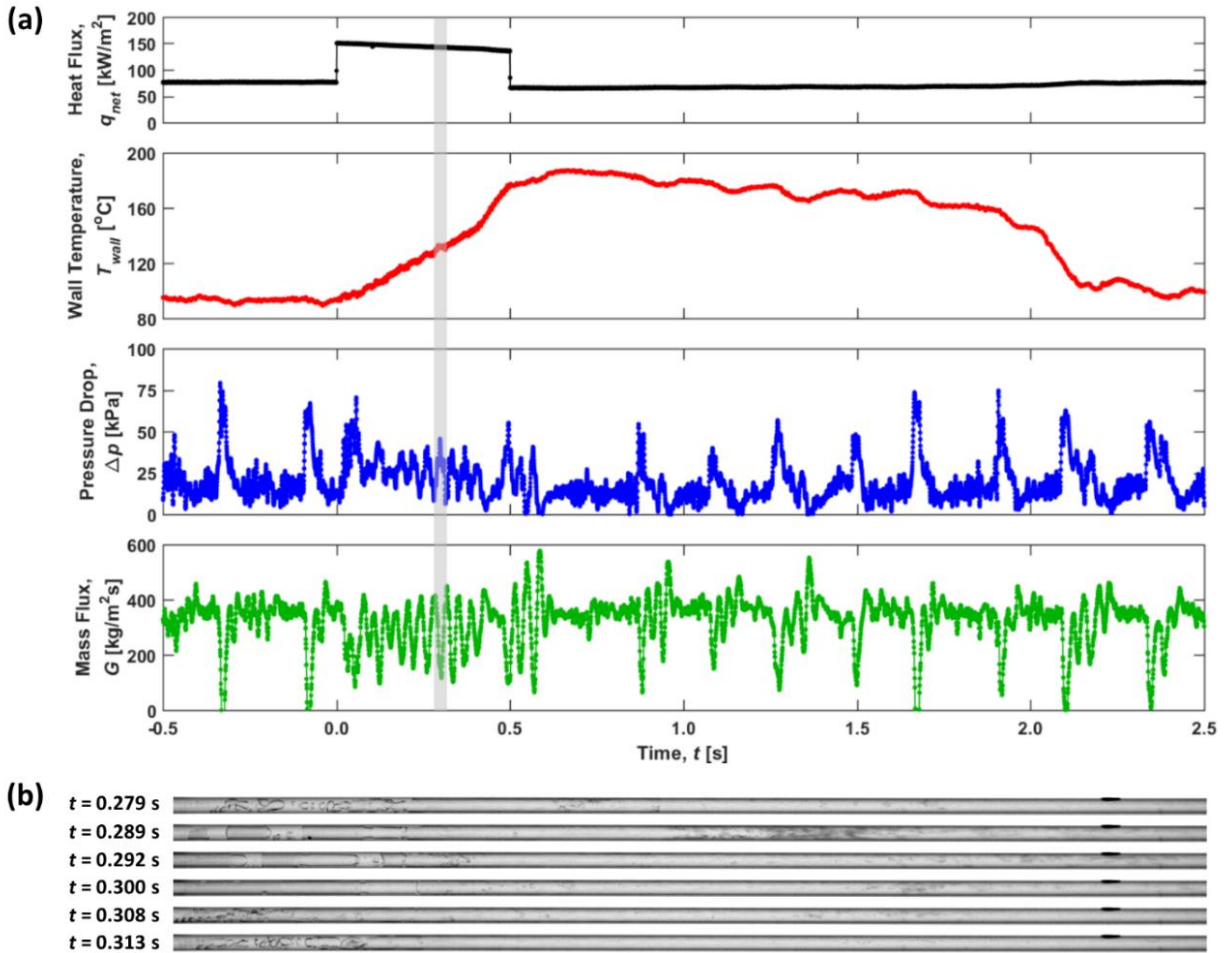
Figure 6.6. (a) Synchronized measurements of heat flux, wall temperature, pressure drop, and mass flux as a function of time for -0.5 to 2.5 s relative to the start of a 0.5 s heat flux pulse from 75 to 150 kW/m² (operating scenario 4).  (b) Selected images of the two-phase morphology are shown that correspond to the time period indicated by the gray box in (a).

## 6.3    Conclusions

The dynamic response of a microchannel flow boiling to a single heat flux pulse was experimentally investigated in this study.  A heat flux applied to the ITO layer on the channel enabled transient heating simultaneous to high-speed flow visualization of the two-phase morphology and high-frequency measurement of the wall temperature, pressure drop, and mass flux.  Thermal and hydrodynamic characterization was first performed during constant heating to identify the single-phase and two-phase flow operating conditions.  Three different heat flux

levels which result in highly contrasting flow conditions were selected based on the time-averaged data, namely $q_{net}$ = 15, 75, and 150 kW/m$^2$, which respectively correspond to single-phase flow, continuous two-phase flow, and what would be critical heat flux if heated continuously. Four different operating scenarios are possible for pulsed heating tests based on the three selected heat flux levels. The pulse duration was incremented for each operating scenario until either a steady condition was achieved during the pulse or the wall temperature reached the temperature limit. At the onset of boiling, the dynamic response resembled an underdamped mass-spring-damper system subjected to a unit step input. During transitions between single-phase flow and time-periodic flow boiling, the wall temperature temporarily overshoots the eventual steady operating temperature thus demonstrating that transient performance can extend beyond the bounds of steady performance. Furthermore, it is shown that longer duration high-heat-flux pulses can be withstood when the fluid in the microchannel is initial boiling before the pulse compared to if it is initially in the single-phase flow regime.

# 7 TIME-RESOLVED CHARACTERIZATION OF MICROCHANNEL FLOW BOILING DURING TRANSIENT HEATING: PART 2 – DYNAMIC RESPONSE TO TIME-PERIODIC HEAT FLUX PULSES

This chapter extends the work presented in the previous chapter by experimentally characterizing the dynamic flow boiling response to time-periodic heat flux pulses.  The effect of heating pulse frequency on flow regime transitions, pressure drop oscillations, and heat flux propagation is shown.

## 7.1 Experimental Methods

The experimental facility is described in Part 1 [70] of this two-part study; a brief description is provided here.  Degassed, dielectric HFE-7100 liquid is delivered to the test-section microchannel, shown in Figure 7.1, using a constant pressure reservoir.  The liquid flow rate and the test section outlet saturation pressure can be adjusted using needle valves placed in the open flow loop.  The liquid volumetric flow rate is measured using an upstream liquid flow meter.  The liquid is preheated to the desired inlet temperature immediately upstream of the test section using a constant-temperature circulating bath. The inlet and outlet fluid temperatures are measured immediately upstream and downstream of the test section.  The inlet and outlet pressure of the microchannel are measured using separate pressure transducers; the pressure drop

across the microchannel is taken as the difference between the inlet and outlet pressure measurements.

The test-section microchannel is mounted horizontally between two polyetheretherketone (PEEK) connectors, which serve as the inlet and outlet plenums (Figure 7.1). The circular cross-section microchannel is made of borosilicate glass with an inside diameter of 500 μm and a wall thickness of 100 μm. The thin wall enables transient heating profiles to propagate to the coolant with minimal damping and delay, as may occur in embedded cooling heat sinks [68, 69]. The outside surface of the microchannel is coated with a 100 nm-thick layer of indium tin oxide (ITO). The ITO layer is optically transparent and electrically conductive, enabling simultaneous Joule heating and visualization of the two-phase flow.
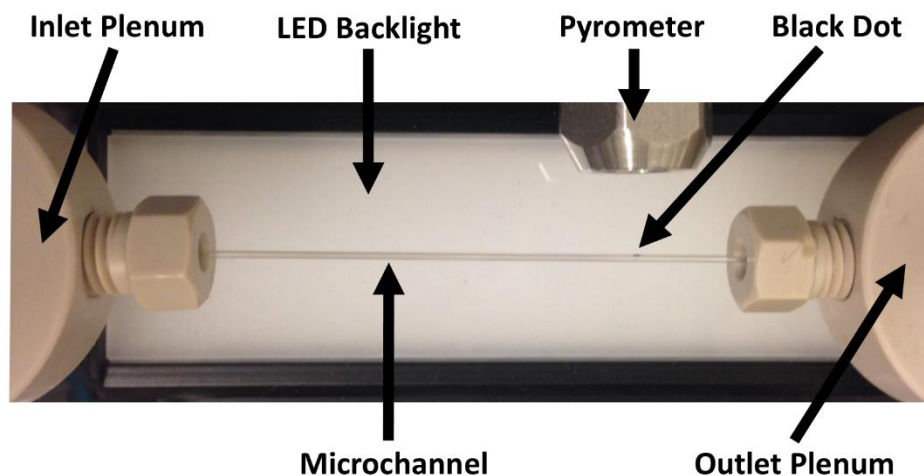


Figure 7.1. Test-section microchannel and surrounding equipment.

Power is supplied to the ITO coating using an adjustable direct current power supply. The total heating power (which includes power loss to the ambient) applied to the test section is quantified by measuring the voltage drop across and current through the ITO microchannel coating. A solid-state switch is wired in parallel to several potentiometers to allow transient switching between two different power levels and fine adjustment of the magnitudes. The switch

is activated by an output voltage signal from a data acquisition (DAQ) unit that is controlled using LabVIEW.  The outside wall temperature of the microchannel is measured at a single fixed location using a pyrometer coupled to a focusing lens.  The pyrometer is focused on a black dot painted on the outside surface of a channel.  Test-section heat flux, wall temperature, pressure drop, and mass flux measurements are obtained at 2,500 Hz using the high-frequency DAQ unit.

The entire heated region of the microchannel is visualized from the top using a high-speed camera coupled to a macro lens.  The bottom side of the channel is uniformly illuminated using a light-emitting diode backlight.  High-speed optical images are synchronized to heat flux, wall temperature, pressure drop, and mass flux measurements using a pulse generator to simultaneously trigger the camera and high-frequency DAQ unit.

Three different heat flux levels were selected to construct the transient heating profiles based on the time-averaged data described in Part 1 of this study.  The selected levels are: $q_{net} =$ 15, 75, and 150 kW/m$^2$, which under steady heating conditions respectively correspond to single-phase flow, continuous flow boiling, and above critical heat flux (if operated at 150 kW/m$^2$ continuously).  Once the desired flow conditions were set (reservoir pressure of 190 kPa, mass flux of 400 kg/m$^2$s, and test section outlet pressure of 114 kPa) using the same procedure described in Part 1 of this study [70], a square wave heating profile was applied to the microchannel.  The different square wave profiles investigated are defined by operating scenarios and frequencies shown in Table 7.1.  For each operating scenario, the square wave profile switches between two of the selected levels, noted as the low and high heating levels in the table.  For operating scenarios 1 and 2, a 50% duty cycle (defined as the ratio of time at the high heating level to total time for each period) was used whereas for operating scenario 3, composed of the two higher heating levels, the duty cycle was reduced to 25% to keep the

transient wall temperature below 200 °C.  For each operating scenario, tests were initiated at the

highest heating pulse frequency (100 Hz) and reduced either to 0.1 Hz or until the transient wall

temperature measured during the tests approached the 200 °C limit; the lowest heating pulse

frequency for operating scenarios 2 and 3 was 0.8 Hz.  For each operating scenario, sensor data

and optical images were recorded for 12 s at 2,500 Hz and 30,000 fps, respectively.  The data

reduction methods used to process the acquired data were the same as those described in Part 1

of this study [70].

Table 7.1. Operating conditions used in this study to perform time-periodic heating of the microchannel.

| Operating Scenario | Low Heating Level [kW/m$^2$] | High Heating Level [kW/m$^2$] | Duty Cycle [%] | Heating Pulse Frequency, $f$ [Hz] |
|:---:|:---:|:---:|:---:|:---:|
| 1 | 15 | 75 | 50 | 0.1, 0.2, 0.5, 1, 2, 5, 10, 15, 20, 25, 50, 100 |
| 2 | 15 | 150 | 50 | 0.8, 1, 2, 3, 4, 5, 10, 15, 20, 25, 50, 100 |
| 3 | 75 | 150 | 25 | 0.8, 1, 2, 3, 4, 5, 10, 15, 20, 25, 50, 100 |

## 7.2    Results and Discussion

### 7.2.1    Summary of Transient Heating-induced Fluctuations

The heating pulse levels and frequencies investigated in this study (Table 7.1) resulted in

three different time-periodic flow boiling fluctuations: flow regime transitions, pressure drop

oscillations, and heating pulse propagation.  In this study, flow regime transitions are defined as

time-periodic transitions between single-phase flow and two-phase flow that arise due to low-

frequency (~1 Hz) compressibility effects within the flow loop at heat fluxes just beyond that

required to induce boiling and cause relatively cool incoming liquid to quench the channel wall

and cease boiling.  These flow regime transitions are separate from those directly induced by

increases or decreases in the heat flux level that induce or cease boiling.  Pressure drop

oscillations occur due to interaction and delayed feedback between vapor within the heated channel and upstream compressibility. These oscillations cause time-periodic oscillations in the wall temperature, pressure drop, and mass flux, and occur at a frequency higher than the flow regime transitions. Heat flux propagation is defined as identifiable thermal and flow fluctuations at the heating pulse frequency that result from the applied heat flux propagating through the microchannel wall and into the fluid.

Not all of these time-periodic fluctuations occur at each operating condition; Figure 7.2 provides three summary charts that describe which of the three time-periodic fluctuations were observed at each operating condition. Each chart is labelled to the left with the heating pulse levels corresponding to the three different operating scenarios; the applied heating pulse frequency is shown along the top horizontal axis. Within each chart, colored horizontal bars correspond to the range of frequencies over which each type of fluctuation was observed: a blue bar indicates flow regime transitions, a green bar indicates pressure drop oscillations, and a red bar indicates heating pulse propagation, as noted by labels to the right of each chart. Operating frequency ranges without a colored horizontal bar indicate that these time-periodic fluctuations were not observed; fading of the bar from colored to white indicates a gradual attenuation of the fluctuations. Dashed vertical lines in Figure 7.2 indicate the specific combinations of heating pulse levels and frequency that were tested in this study (Table 7.1), from which these charts were constructed.

In this study, flow regimes transitions only occurred when the heat flux was pulsed between 15 and 75 kW/m$^2$ (operating scenario 1) and the heating pulse frequency was greater than or equal to the intrinsic frequency of the flow regime transitions ($f \geq 1$ Hz), as shown in Figure 7.2. For heat flux pulse frequencies less than the intrinsic frequency of the flow regime

transitions ($f < 1$ Hz), boiling incipience would occur when switched to $q_{net} = 75$ kW/m$^2$ and stop

boiling when switched to $q_{net} = 15$ kW/m$^2$. Thus, the mechanism causing the flow to transition

between single-phase flow and two-phase under these heating conditions ($f < 1$ Hz) is different

than that for the flow regime transitions. Flow regime transitions were not observed for any

heating frequency where the heat flux was pulsed between 15 and 150 kW/m$^2$ or 75 to

150 kW/m$^2$ because the effective heat flux experienced by the channel is large enough to

continuously maintain boiling.

For all operating scenarios and heating pulse frequencies tested in this study, time-

periodic pressure drop oscillations resulting from the pressure drop instability were observed. At

intermediate heating pulse frequencies ($1 < f < 10$ Hz), the heating profile is heavily coupled to

the cooling performance and the pressure drop oscillation frequency exactly aligns with the

heating frequency. At relatively low ($< 1$ Hz) and high ($> 10$ Hz) heating pulse frequencies,

pressure drop oscillations occurred at the intrinsic frequency of the system.

Time-periodic heating of the microchannel resulted in thermal and flow fluctuations at

the heating frequency only when the heating frequency was less than approximately 25 Hz.

Above this cutoff frequency, the heating pulse frequency was too fast to propagate to the fluid

and was effectively damped by the microchannel wall.
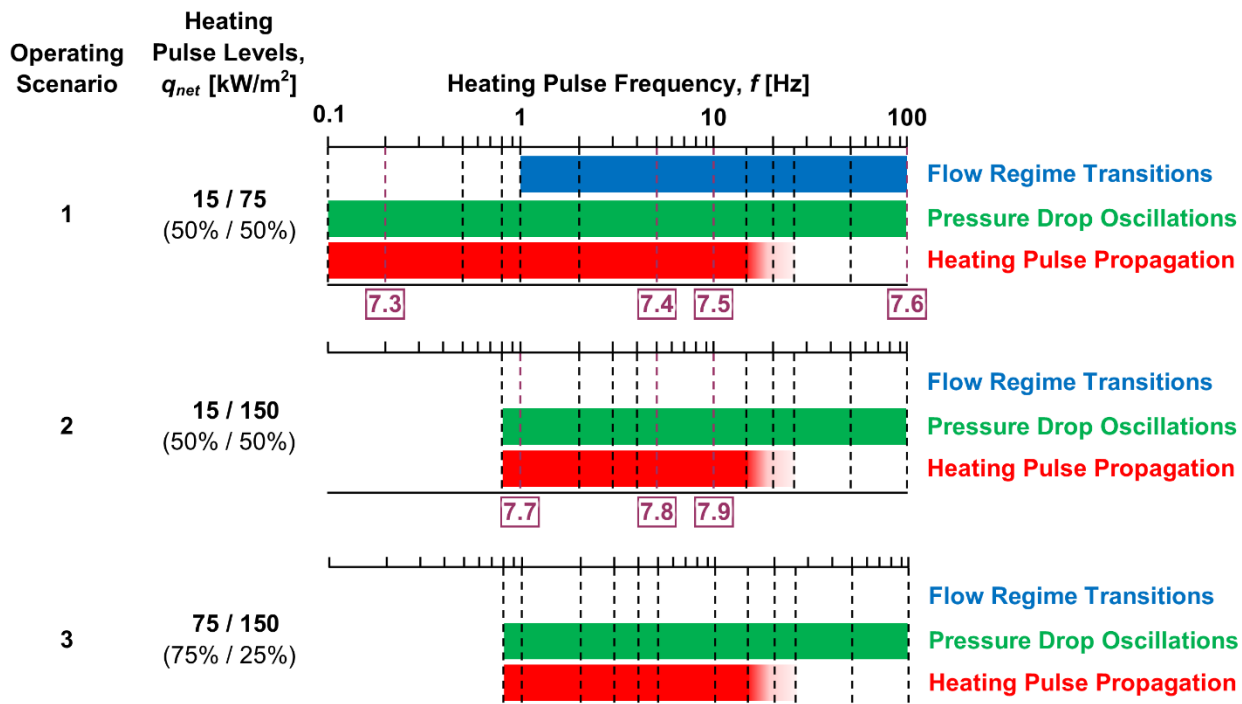
Figure 7.2. Summary charts for each operating scenario showing the range of heating pulse frequencies over which flow regime transitions and pressure drop oscillations are observed, as well as whether the heating pulses propagate to the fluid.  Colored horizontal bars indicate the frequency range associated with each charactersitc fluctuation labelled in the matching font color.  Dashed vertical lines indicate the specific combinations of heating pulse levels and frequencies that were tested (Table 7.1).  The numbers inscribed in the boxes (7.3 through 7.9) denote the selected operating conditions detailed in Section 7.2.2 and correspond to Figure 7.3 through Figure 7.9.

Analysis of the time and spectral domain for four heating pulse frequencies (0.2, 5, 10, and 100 Hz) for operating scenario 1 (15 / 75 kW/m$^2$) and three heating pulse frequencies (1, 5, and 10 Hz) for operating scenario 2 (75 / 150 kW/m$^2$) are provided in Section 7.2. to illustrate the effect of heating pulse frequency and time-periodic fluctuations that are summarized in Figure 7.2.  Because operating scenarios 2 and 3 resulted in continuous boiling for all heating pulse frequencies, the observed time-periodic fluctuations were similar for both cases, so analysis of the time and spectral domain for operating scenario 3 is not shown.  A summary of the primary observations and takeaways from each of these seven selected operating conditions

is shown in Table 7.2.  Figure 7.3-Figure 7.9 (one figure for each selected operating condition in Section 7.2.2) show (a) the sensor measurements in the time domain and (b) their corresponding normalized spectral density in the frequency domain as determined using a fast Fourier transform.

Table 7.2. Summary of the primary observations and takeaways from selected operating conditions corresponding to Figure 7.3-7.9.

| Operating Scenario | Low Heat Flux Level [kW/m²] | High Heat Flux Level [kW/m²] | Heating Pulse Frequency, $f$ [Hz] | Corresponding Figure | Flow Regime Transitions? | Pressure Drop Oscillations? | Heating Pulse Propagation? | Primary Observations and Takeaways |
|---|---|---|---|---|---|---|---|---|
| 1 | 15 | 75 | 0.2 | 7.3 | No | Yes | Yes | • Flow regime transitions resulting from compressibility effects do not occur because the mechanism causing boiling is switching of the heat flux level<br>• Pressure drop oscillations occur at 4 Hz during instances when $q_{net}$ = 75 kW/m²<br>• Individual heating pulses propagate through the microchannel wall to the fluid because the heating pulse frequency is low |
| | | | 5 | 7.4 | Yes | Yes | Yes | • Propagation of the heating pulse frequency forces the pressure drop oscillations to occur at exactly 5 Hz<br>• Flow regime transitions occur at 1 Hz and are superimposed with pressure drop oscillations |
| | | | 10 | 7.5 | Yes | Yes | Yes | • Flow regime transitions occur at 1 Hz and are superimposed with 4 Hz pressure drop oscillations<br>• Heating pulses propagate to the fluid at 10 Hz and appear in all sensor measurements |
| | | | 100 | 7.6 | Yes | Yes | No | • The high heating pulse frequency cannot propagate to the fluid, causing the channel to be essentially heated at a constant heat flux of $q_{net}$ = (15+75)/2 = 45 kW/m²<br>• Flow regime transitions occur at 1 Hz and are superimposed with 7 Hz pressure drop oscillations |
| 2 | 15 | 150 | 1 | 7.7 | No | Yes | Yes | • The fluid is boiling continuously for all heating pulse frequencies for operating scenario 2<br>• Pressure drop oscillations occur at 32 Hz during instances when $q_{net}$ = 150 kW/m² |
| | | | 5 | 7.8 | No | Yes | Yes | • The heating pulses are propagating and force the pressure drop oscillations to occur at exactly 5 Hz |
| | | | 10 | 7.9 | No | Yes | Yes | • The heating pulses are propagating to the fluid and appear in all sensor measurements<br>• Pressure drop oscillations are occurring at 5 Hz |

The primary observations and takeaways for operating scenario 3 are not listed because they are the same as operating scenario 2

### 7.2.2    Time and Spectral Domain Analysis

Shown in Figure 7.3 are the sensor measurements for heat flux pulses between 15 and

75 kW/m$^2$ at 0.2 Hz and the corresponding normalized spectral density of the signals as

determined using a fast Fourier transform.  The amplitude of the spectral density resulting from

the transformation is normalized relative to the maximum spectral density of each sensor

measurement.  For this case, the relatively low-frequency heat flux pulses are effectively isolated

from one another and the flow reaches a time-periodic boiling condition during each pulse to

75 kW/m$^2$ and returns to a steady single-phase flow regime between each pulse.  As shown in

Figure 7.3a, prior to the heat flux pulse, the sensor measurements are steady in time ($\Delta p = 2$ kPa,

$G = 410$ kg/m$^2$s, and $T_{wall} = 90$ °C) and the flow is in the single-phase regime.  Once the pulse

begins at $t = 0.5$ s, the wall temperature increases and boiling is initiated in the channel shortly

thereafter at $t = 0.62$ s.  At approximately $t = 1.7$ s, a time-periodic wall temperature oscillating

around a mean of ~115 °C is observed, in addition to corresponding time-periodic oscillations in

the pressure drop and mass flux.  These oscillations in the wall temperature, pressure drop, and

mass flux are caused by the pressure drop instability.  Spectral analysis of the sensor

measurements, as shown in Figure 7.3b, indicates that the primary frequency is 0.2 Hz,

corresponding to the heating frequency.  The smaller peaks that decay with increasing frequency

in the normalized spectral density at multiples of the 0.2 Hz heating pulse frequency are

harmonics of the spectral analysis.  If the spectral analysis is applied only to data during the heat

flux pulse, an intrinsic pressure drop oscillation frequency of 4 Hz is identified (not shown in

Figure 7.3).  Because boiling is being induced or ceased when the heat flux changes between $q_{net}$

$= 15$ kW/m$^2$ and $q_{net} = 75$ kW/m$^2$, and rather than occurring due to interaction with the upstream

compressible volume, the changes between single-phase flow and two-phase flow are *not* classified as flow regime transitions.
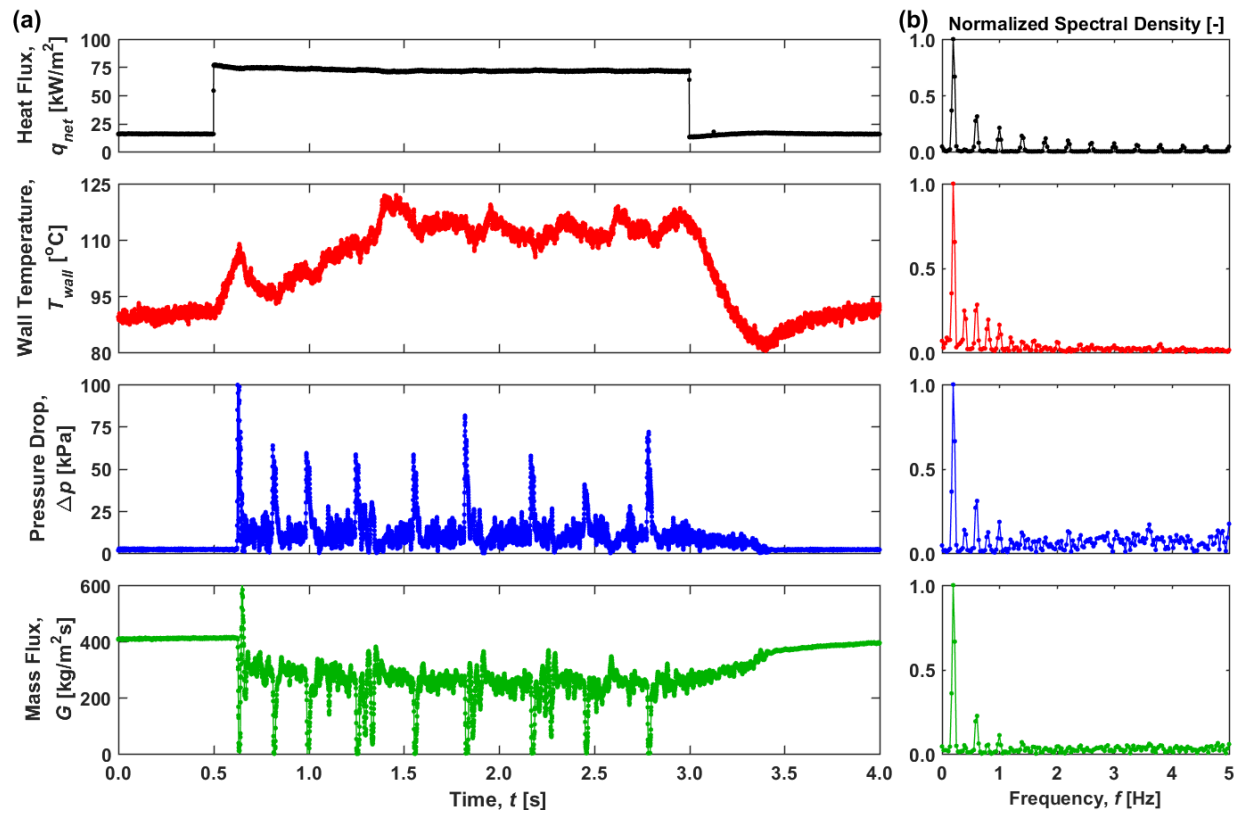


Figure 7.3. (a) Heat flux, wall temperature, pressure drop, and mass flux as a function of time for heat flux pulses between 15 and 75 kW/m$^2$ (operating scenario 2) at 0.2 Hz. (b) Normalized spectral density of the sensor measurements.

Shown in Figure 7.4 are the sensor measurements for heat flux pulses between 15 and 75 kW/m$^2$ at 5 Hz and the corresponding normalized spectral density of the signals. At this frequency, the fluid in the channel is always boiling. The close proximity of the heating pulse frequency (5 Hz) to the intrinsic pressure drop oscillation frequency under constant heating conditions (observed to be in the range of 4-7 Hz for this operating condition) causes the pressure drop oscillations to occur in exact alignment with the heating pulse frequency at 5 Hz, as indicated by the large, distinct spike in the normalized spectral density in Figure 7.4b. Meanwhile, time-periodic flow regime transitions are also occurring at 1 Hz, as indicated by the

second spike in the normalized spectral density for the wall temperature in Figure 7.4b. When the flow transitions to single-phase flow, a relatively large spike in the wall temperature occurs, as shown in Figure 7.4a at $t = 0.4$ and 1.4 s. These flow regimes transitions are caused by depressurization of the upstream compressible volume, which surges cooler liquid through the channel and suppresses nucleation, causing a transition to single-phase liquid flow. The wall temperature of the channel then increases until the fluid begins boiling, and the process repeats.
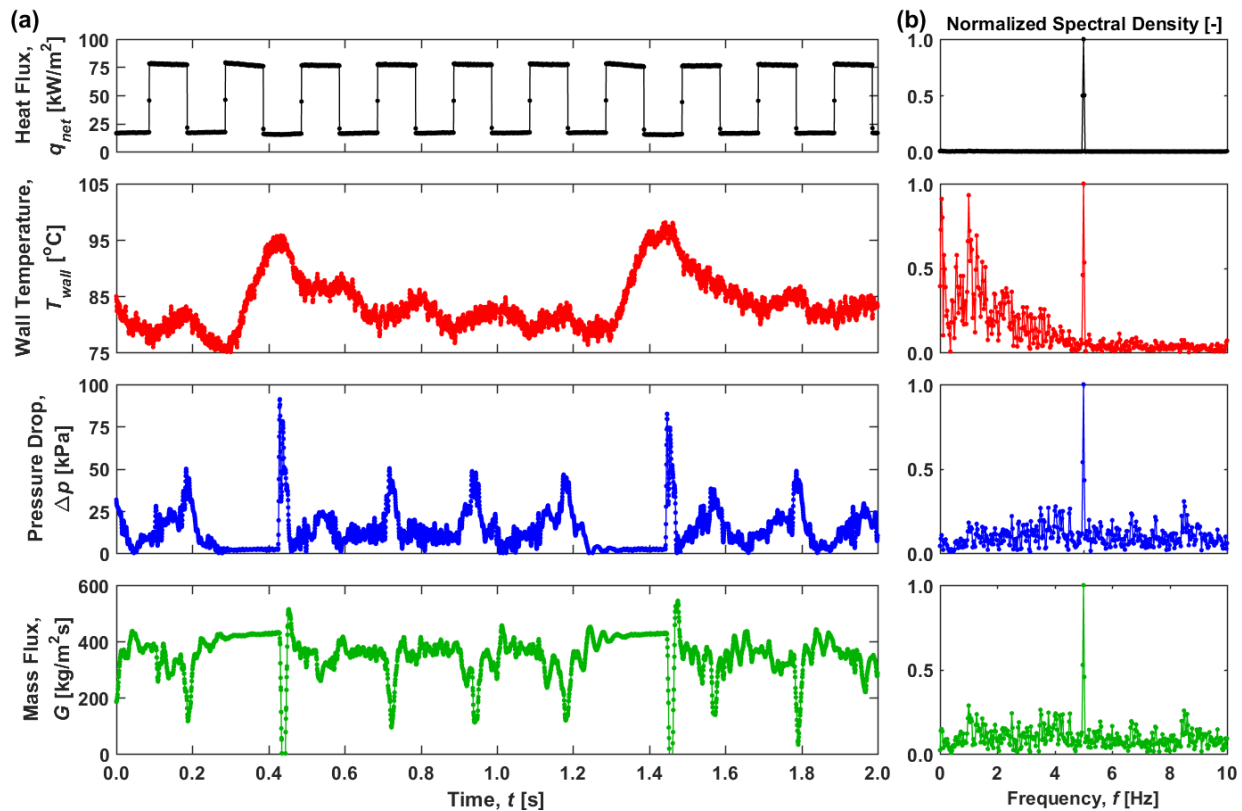


Figure 7.4. (a) Heat flux, wall temperature, pressure drop, and mass flux as a function of time for heat flux pulses between 15 and 75 kW/m$^2$ (operating scenario 1) at 5 Hz. (b) Normalized spectral density of the sensor measurements.

Shown in Figure 7.5 are the sensor measurements for heat flux pulses between 15 and 75 kW/m$^2$ at 10 Hz and the corresponding normalized spectral density of the signals. The heating pulse frequency is still able to propagate through the microchannel wall at this higher frequency; a spike in the normalized spectral density for each sensor appears at $f = 10$ Hz.

However, the heating pulse frequency is too fast to force the pressure drop oscillations to occur at this frequency. The pressure drop oscillations instead occur at the intrinsic frequency of ~4 Hz, as indicated by the small peak in Figure 7.5b at 4 Hz and confirmed by the flow visualizations. Meanwhile, flow regime transitions are also occurring, as indicated by the large periodic increases in the wall temperature Figure 7.5a and the large spike at 1 Hz in the wall temperature normalized spectral density in Figure 7.5b.
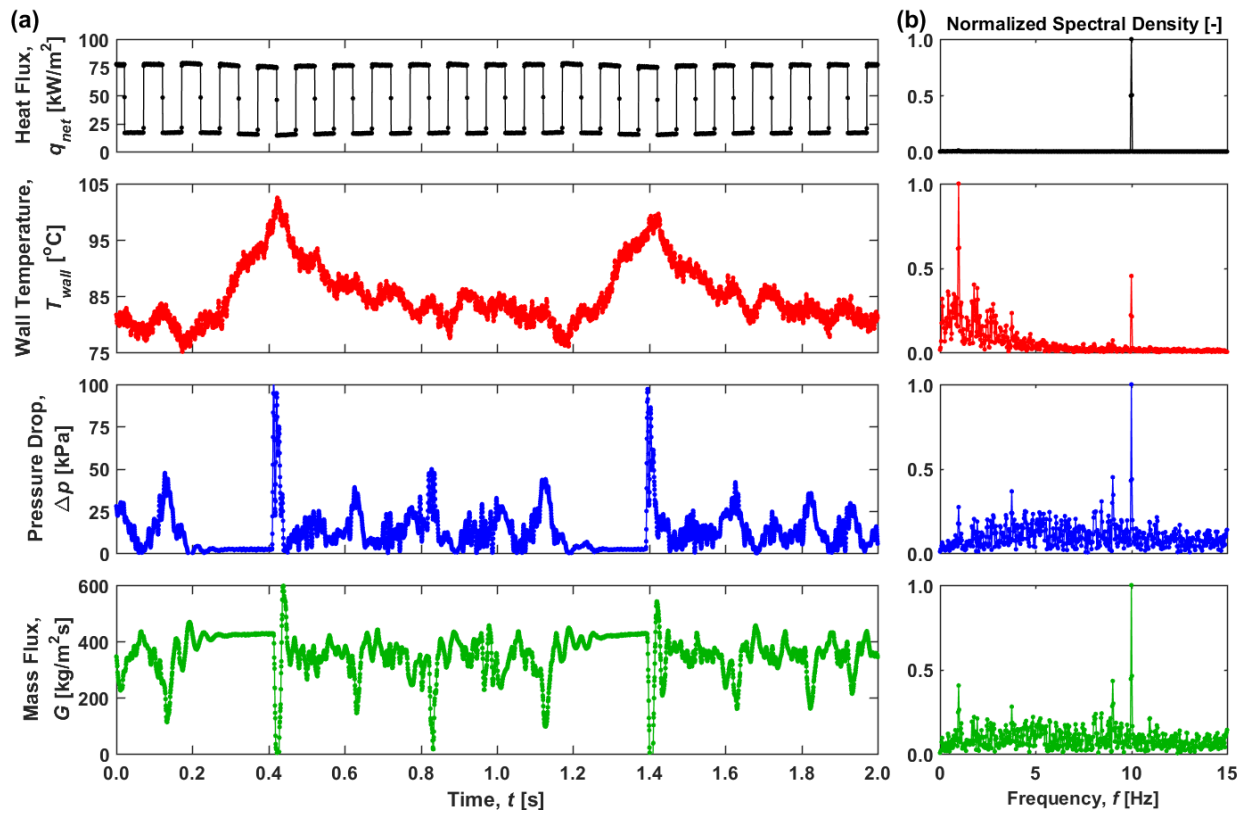


Figure 7.5. (a) Heat flux, wall temperature, pressure drop, and mass flux as a function of time for heat flux pulses between 15 and 75 kW/m$^2$ (operating scenario 1) at 10 Hz. (b) Normalized spectral density of the sensor measurements.

Shown in Figure 7.6 are the sensor measurements for heat flux pulses between 15 and 75 kW/m$^2$ at 100 Hz and the corresponding normalized spectral density of the signals. At this much higher frequency of $f = 100$ Hz, the heat flux profile changes so quickly that the microchannel wall entirely damps the heating transients and the channel behaves as if it were

effectively heated at a steady heat flux of $q_{net} = (15+75)/2 = 45$ kW/m$^2$. It was shown in Part 1 of this two-part study [70] that constant heating at 45 kW/m$^2$ results in time-periodic flow regimes transitions, which are indicated in Figure 7.6a by the large spikes in the wall temperature and pressure drop (and large dips in the mass flux) at $t = 0.47$ and 1.70 s. In between instances of single-phase flow, when the fluid is boiling, pressure drop oscillations are observed, as shown by the smaller magnitude, higher frequency fluctuations in the wall temperature, pressure drop, and mass flux in Figure 7.6a. Spectral analysis of the sensor measurements clearly shows that the heating pulse frequency of 100 Hz does not propagate to the fluid; the flow regime transitions and pressure drop oscillations are occurring at 1 Hz and 7 Hz, respectively.
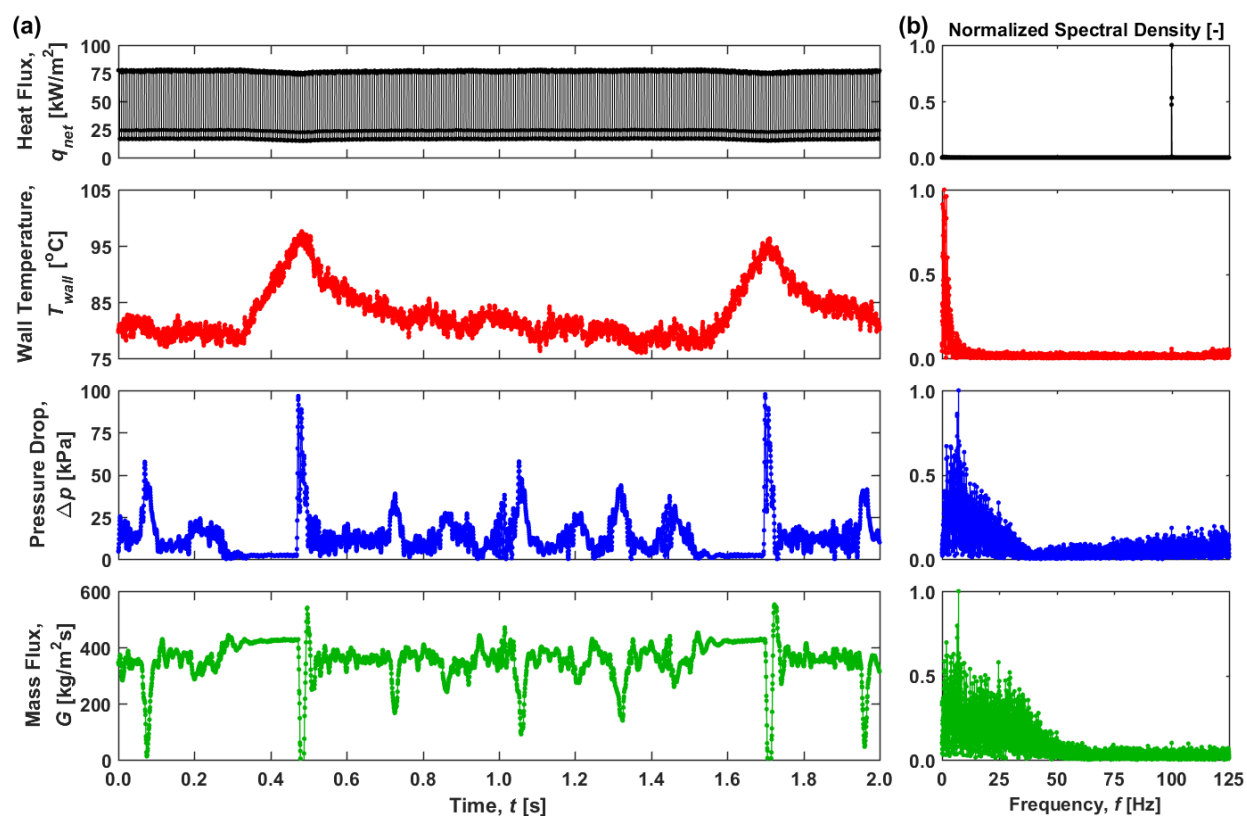


Figure 7.6. (a) Heat flux, wall temperature, pressure drop, and mass flux as a function of time for heat flux pulses between 15 and 75 kW/m$^2$ (operating scenario 1) at 100 Hz. (b) Normalized spectral density of the sensor measurements.

Shown in Figure 7.7 are the sensor measurements for heat flux pulses between 15 and 150 kW/m$^2$ at 1 Hz and the corresponding normalized spectral density of the signals. For operating scenario 2 (*i.e.*, pulses between 15 and 150 kW/m$^2$), the fluid in the microchannel boils continuously regardless of the heating pulse frequency. Spectral analysis of the sensor measurements indicates that heating pulses at 1 Hz are driving the thermal and hydrodynamic fluctuations at exactly the heating pulse frequency, as shown in Figure 7.7b. As shown in Figure 7.7a, during the pulses to 150 kW/m$^2$, the wall temperature increases continuously, and time-periodic oscillations in the pressure drop and mass flux are observed. Between pulses, the wall temperature reduces and the pressure drop and mass flux signals flatten out because the vapor in the channel moves downstream. During individual pulses to 150 kW/m$^2$, high-frequency pressure drop oscillations are occurring at 32 Hz, as shown by the peak in the normalized spectral density of the mass flux signal in Figure 7.7b. The large increase in the intrinsic pressure drop oscillation frequency at 150 kW/m$^2$, relative to those previously observed at lower heat flux levels, is due to vapor nucleating from the microchannel wall near the inlet of the channel. This reduces the length of the channel that vapor travels upstream when undergoing the pressure drop instability and thus increases the intrinsic frequency of the oscillations, as was discussed in Part 1 of this two-part study [70].
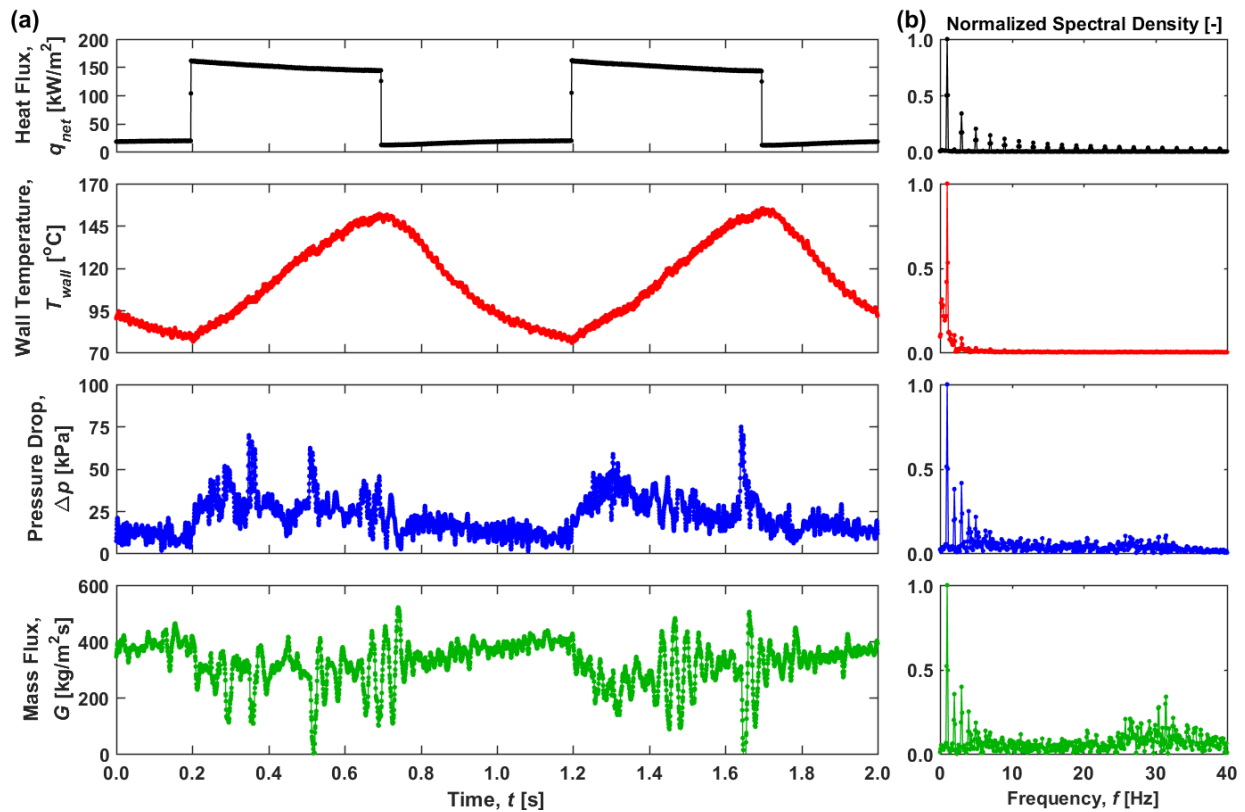
Figure 7.7. (a) Heat flux, wall temperature, pressure drop, and mass flux as a function of time for heat flux pulses between 15 and 150 kW/m$^2$ (operating scenario 2) at 1 Hz. (b) Normalized spectral density of the sensor measurements.

Shown in Figure 7.8 are the sensor measurements for heat flux pulses between 15 and 150 kW/m$^2$ at 5 Hz and the corresponding normalized spectral density of the signals. Like that of operating scenario 1, a heating pulse frequency of 5 Hz for operating scenario 2 forces the pressure drop instability to occur exactly at this frequency. Large fluctuations in the wall temperature, pressure drop, and mass flux exactly match the frequency of heat flux profile, as shown in Figure 7.8a. These fluctuations are so distinct that a single spike in the normalized spectral density for each sensor measurement appears in Figure 7.8b.
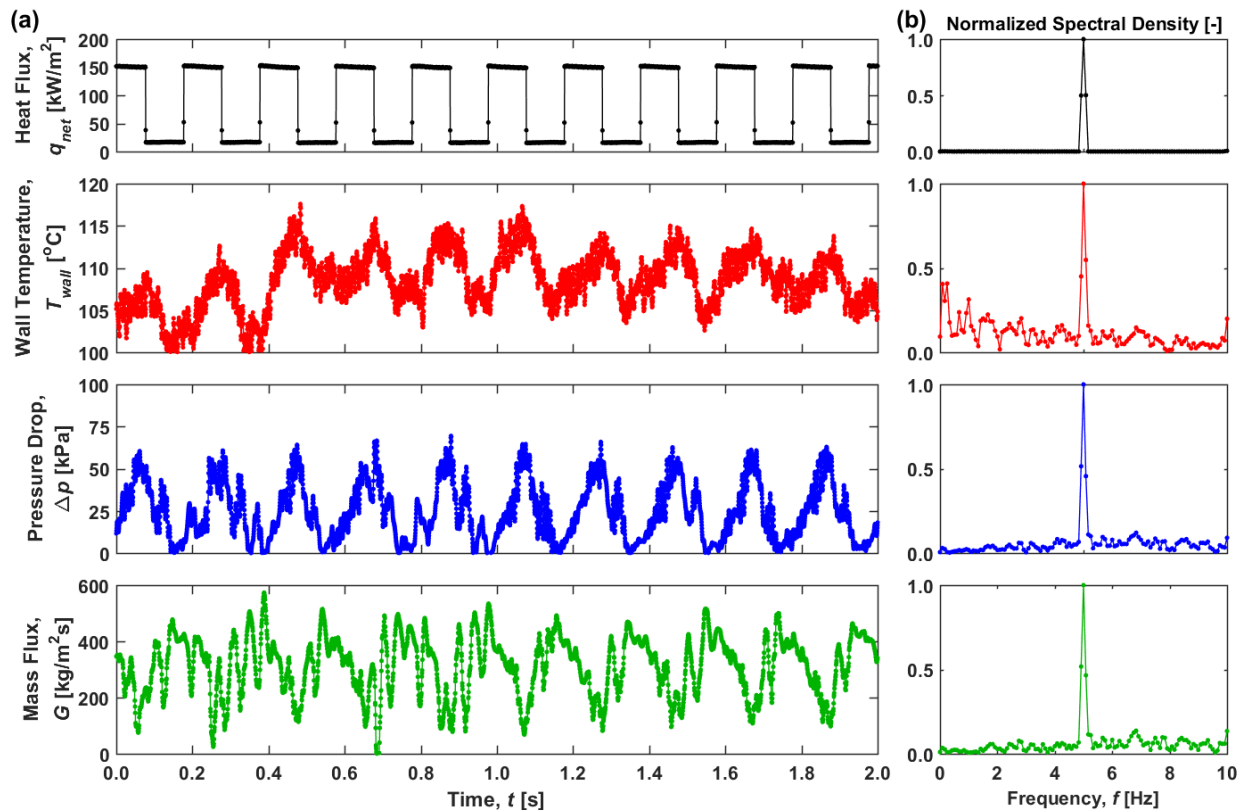
Figure 7.8. (a) Heat flux, wall temperature, pressure drop, and mass flux as a function of time for heat flux pulses between 15 and 150 kW/m$^2$ (operating scenario 2) at 5 Hz. (b) Normalized spectral density of the sensor measurements.

Shown in Figure 7.9 are the sensor measurements for heat flux pulses between 15 and 150 kW/m$^2$ at 10 Hz and the corresponding normalized spectral density of the signals. The wall temperature, pressure drop, and mass flux fluctuate at 10 Hz, corresponding to the heating pulse frequency. Superimposed on these small amplitude oscillations are much larger amplitude oscillations (most identifiable in the pressure drop and mass flux signal) at 5 Hz, which corresponds to the pressure drop instability, as indicated by the small peak in the normalized spectral density at this frequency in Figure 7.9b. This peak is much broader as compared to when the heating pulse frequency forces the pressure drop oscillations (*e.g.*, at 5 Hz in Figure 7.4 and Figure 7.8).
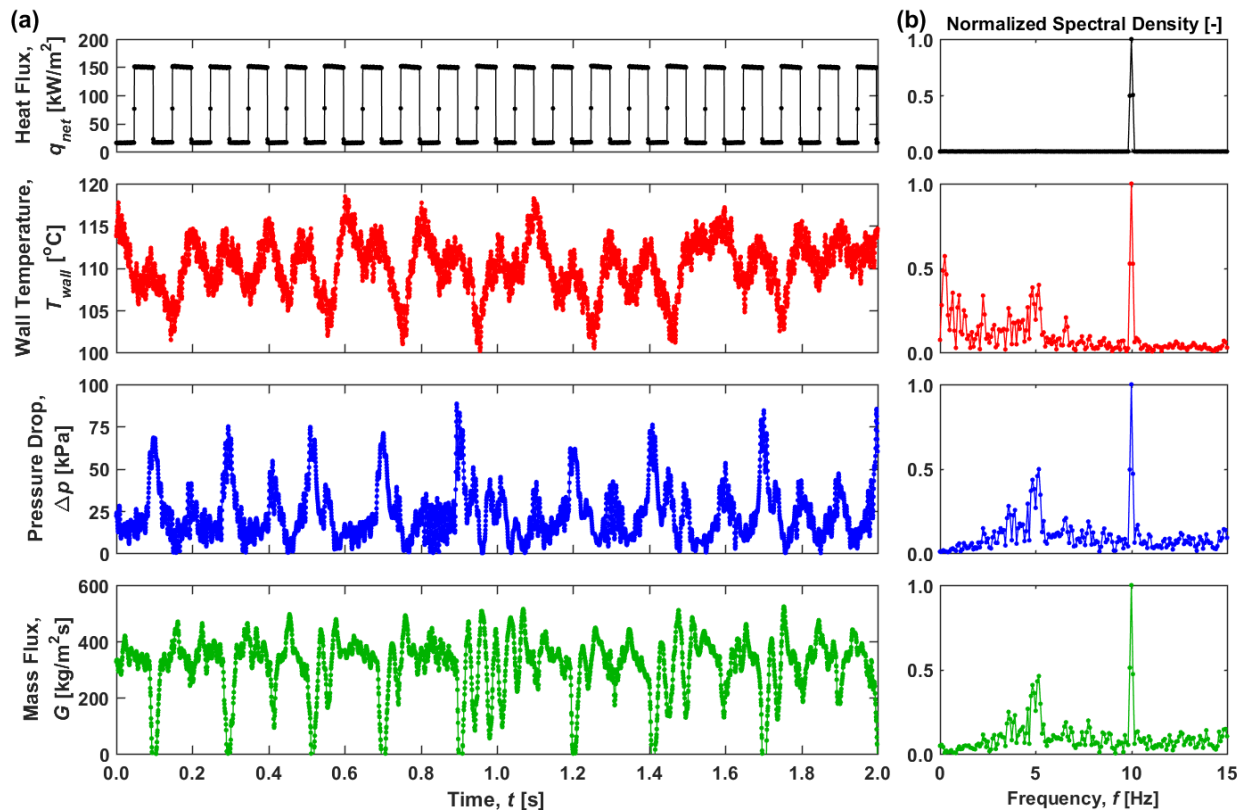
Figure 7.9. (a) Heat flux, wall temperature, pressure drop, and mass flux as a function of time for heat flux pulses between 15 and 150 kW/m$^2$ (operating scenario 2) at 10 Hz.  (b) Normalized spectral density of the sensor measurements.

## 7.3    Conclusions

The effects of heating pulse frequency on the resulting time-periodic fluctuations during microchannel flow boiling were experimentally investigated.  A time-periodic series of heat flux pulses applied to the microchannel via an ITO coating was varied between 15, 75, and 150 kW/m$^2$ for heating pulse frequencies ranging from 0.1 Hz to 100 Hz.  These three heat flux levels were selected because they exhibited highly contrasting flow conditions under constant heating conditions, namely single-phase flow, continuously two-phase flow, and what would be critical heat flux if heated continuously.  High-speed optical visualizations of the two-phase morphology were synchronized to high-frequency measurements of the heat flux, wall

temperature, pressure drop, and mass flux.  Spectral analysis was applied to the sensor

measurements to determine the characteristic fluctuation frequencies resulting from the transient

heating conditions.

Three different time-periodic flow boiling fluctuations were observed:  flow regime

transitions, pressure drop oscillations, and heating pulse propagation.  The range over which

these oscillations were observed were then mapped to the heating pulse frequency (Figure 7.2)

and key observations and takeaways were presented (Table 7.2).  In general, it was observed

that: (i) low heating frequencies ($f$ < 1 Hz) act as step changes between different heat flux levels,

(ii) at intermediate heating frequencies ($1 < f < 10$ Hz), the flow boiling instabilities and

performance are heavily coupled to the heating profile thus causing the pressure drop oscillation

frequency to exactly match the heating pulse frequency, and (iii) at high heating frequencies ($f >$

10 Hz), the transient heat flux profile is attenuated and becomes effectively a constant heat flux

above ~25 Hz.  The observed dependence of flow instabilities and thermal performance on time-

varying heating conditions indicates that flow boiling dynamics will significantly influence

overall performance in various applications.

# 8 AN EXPERIMENTAL METHOD FOR CONTROLLED GENERATION AND CHARACTERIZATION OF MICROCHANNEL SLUG FLOW BOILING

This chapter details a novel experimental method for controlled generation of an archetypal slug flow boiling regime that is free from commonly encountered for boiling instabilities. A high-speed imaging technique is used to quantify key hydrodynamic and heat transfer parameters and demonstrate a method suitable for the validation of physics-based flow boiling models. The material from this chapter was published in *International Journal of Heat and Mass Transfer* [66].

## 8.1 Experimental Methods

### 8.1.1 Test Facility

A constant-pressure reservoir is employed to deliver separate streams of degassed HFE-7100 vapor and liquid into a T-junction to create a microchannel slug flow. An open-loop system (Figure 8.1), driven by the pressure difference between a pressurized reservoir and the ambient, is used to generate the flow. This approach allows controlled, constant flow rates to be achieved even at low flow rates. Vapor is created inside the fixed-volume, stainless steel pressurized reservoir by continuously boiling fluid using a submerged, horizontally mounted cartridge heater. Electrical power is supplied to the cartridge heater using an adjustable direct current (DC) power supply (XG 150-5.6, Sorenson); the heater is connected to a temperature cut-off to detect a low fluid level. The vapor/liquid mixture inside the reservoir is stratified, as illustrated schematically in Figure 8.1, enabling vapor and liquid to be separately drawn out of the reservoir. The pressure in the reservoir is adjustable using a two-phase, back-pressure

regulator (EB1ULF1, Equilibar). The back-pressure regulator uses a pilot line to regulate the reservoir pressure by continuously relieving the reservoir of vapor in order to maintain the desired pressure.

Single-phase vapor and single-phase liquid are extracted from the reservoir through two separate lines. Condensation is prevented in the vapor lines using adjustable electrical heating jackets, thereby maintaining slightly superheated single-phase vapor. The local superheat is monitored along the vapor delivery line using pressure transducers and T-type thermocouples, including at a location immediately upstream of the T-junction, to an accuracy of $\pm$ 0.5 kPa and $\pm$ 1 °C, respectively. The vapor flow rate to the T-junction is controlled using an adjustable vapor control valve. The single-phase liquid flow is controlled and measured using a liquid flow controller (LC-10CCM-D-EPDM, Alicat) to an accuracy of $\pm$ 0.2 mL/min. The liquid mass flow rate is determined using the measured volumetric flow rate and density corresponding to the liquid temperature measured by the flow controller. An electrical heating jacket is used to preheat the liquid to the desired temperature immediately upstream of the T-junction; the subcooling at this location is monitored using a pressure transducer and thermocouple. A PEEK T-junction (MT1PK, Valco) with a 500 μm circular bore is used to combine the vapor and liquid fluid streams and create a two-phase flow in the downstream microchannel. The T-junction bore diameter and test section microchannel inside diameter are identical, yielding a smooth flow path for the two-phase flow. The periodic two-phase flow that forms downstream is a result of the oscillatory behavior that temporarily blocks the liquid and allows the vapor to flow before switching and allowing liquid to flow while blocking the vapor, an effect experimentally demonstrated by Miyabayashi *et al.* [71].

The circular cross-section test-section microchannel is made of borosilicate glass (CV5070, Vitrocom) with a nominal inside diameter of $D = 500$ μm and a wall thickness of $t_w = 100$ μm; this microchannel is mounted horizontally. The microchannel length, nondimensionalized by the channel inside diameter, is $L/D = 200$. The outside surface of the microchannel is custom-coated with a nominally 100 nm-thick layer of indium tin oxide (ITO) using atomic layer deposition (Ultratech Inc.). The ITO layer is optically transparent and electrically conductive, enabling flow visualization while the microchannel is subject to uniform Joule heating. Power is supplied to the ITO coating using an adjustable DC power supply (XG 300-2.8, Sorenson). Another PEEK T-junction is used to support the downstream end of the test section microchannel. The ITO layer is electrically isolated from the flow loop using non-conductive PTFE ferrules and PEEK nuts attached at both ends to the PEEK T-junctions. The pressure drop across the upstream and downstream T-junctions and microchannel is taken as the difference between the measured liquid/vapor pressure immediately upstream of the mixing T-junction and that measured at the downstream T-junction. Fluid leaving the test section (and also the fluid leaving the back-pressure regulator) is collected and passed through a fluid-to-air heat exchanger to condense any vapor before discharging the liquid to an open reservoir at ambient pressure.

All test facility sensor data are obtained at 0.33 Hz using a data acquisition unit (34970A, Agilent) with a 20-channel multiplexer module (34901A, Agilent) using a LabVIEW interface. Power supplied to the test section is quantified by measuring the voltage drop across and current through the ITO microchannel coating; the current is measured using a shunt resistor (6142-1-1000, Empro Shunts). The entire experimental facility is mounted on an isolated optical table

(VIS3672-PG2-325A, Newport) to ensure that external vibrations are not transmitted to the

components.
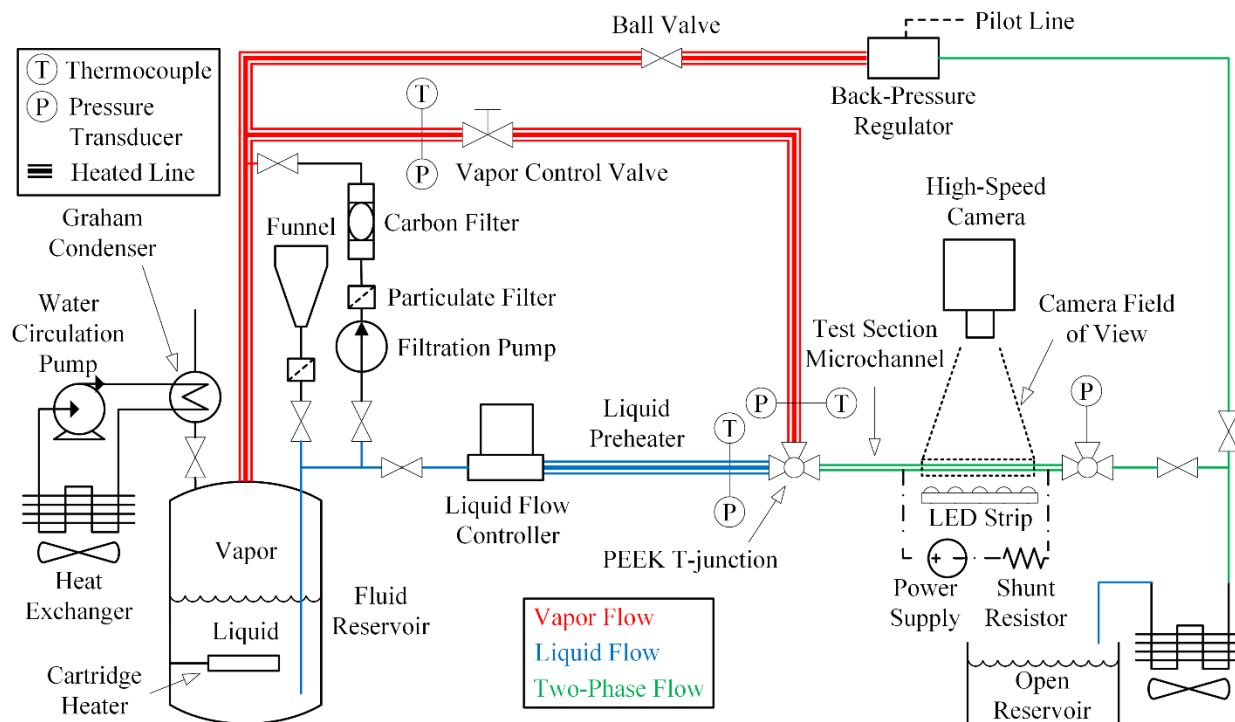


Figure 8.1. Schematic diagram of the experimental test facility.

### 8.1.2  Test Procedure

Immediately prior to testing, the HFE-7100 fluid is degassed by vigorously boiling the

liquid in the reservoir using the cartridge heater.  A Graham condenser (5977-12, Ace Glass Inc.)

condenses the vapor back into the reservoir while non-condensable gases are expelled from the

system.  An auxiliary pumped loop circulates water through the Graham condenser to promote

condensation of the vapor and rejects the heat to the ambient environment using a liquid-to-air

heat exchanger (4210G10SB-F9, Lytron).  While degassing, liquid in the reservoir is

continuously circulated through a 7 μm particulate filter (SS-4TF-7, Swagelok) and an organic

filter (12011, Pall Corporation) to remove any containments from the fluid.

Experiments were initiated by boiling the liquid in the reservoir with only the back-pressure regulator line open. Once the reservoir reaches the pilot line pressure, the back-pressure regulator continuously relieves fluid from the reservoir to maintain a constant reservoir pressure of $134.2 \pm 0.1$ kPa; this constant vapor pressure is required to maintain constant fluid flow rates. The reported uncertainties represent the standard deviation of the values measured over the duration of the test.

The liquid delivery line was then opened and the liquid flow controller was set to deliver a volumetric flow rate of $4.06 \pm 0.01$ mL/min (mass flow rate of $5.68 \pm 0.01$ kg/min) to the T-junction. The liquid preheater was turned on and adjusted to achieve a liquid inlet temperature of $60.1 \pm 0.1$ °C. This corresponds to a subcooling of 4.8 °C at the inlet absolute pressure $(113.1 \pm 0.6$ kPa), ensuring that purely single-phase liquid is delivered to the T-junction. After the liquid delivery line reached steady-state conditions, the vapor line heaters were turned on to preheat the vapor lines. Next, the vapor delivery line was opened. The vapor line heating power and vapor flow rate were iteratively adjusted until the desired downstream slug flow regime (vapor bubble lengths of approximately $L_b/D = 5$) were observed in the visualization images at steady-state conditions. These vapor flow conditions were then held fixed for all power inputs to the test section microchannel. In this study, the average temperature of the vapor being delivered to the T-junction was $71.1 \pm 0.2$ °C. This corresponds to a superheat of 6.9 °C at the inlet absolute pressure $(111.1 \pm 0.6$ kPa), ensuring that purely single-phase vapor is delivered to the T-junction. Note that when the subcooled liquid and superheated vapor combine at the T-junction, some developing length is required before equilibrium is reached and a saturated two-phase flow is established. The vapor superheat and liquid subcooling were each chosen to be small enough such that a saturated two-phase flow is observed to develop within a short distance downstream.

In this study, the two-phase flow is characterized at a fixed streamwise location for all test conditions, far enough downsteam to ensure that saturated flow boiling conditions exist in the region being visualized. While it would be ideal for the vapor and liquid inlet lines to be maintained exactly at saturation, practical operation of the facility requires some respective degrees of superheat and subcooling to ensure that only single-phase flows enter the T-junction; if the inlet encountered two-phase conditions, the flow periodicity in the test section would be entirely disrupted.

The power levels applied to the test section microchannel were chosen to yield an observable difference in the vapor bubble growth rate over the range. In this study, 13 different input power levels ($P_{total}$) ranging from 0.32 W to 0.84 W were tested. Two of the power levels (0.32 W and 0.35 W) resulted in condensing flows while the remaining levels (0.40 W to 0.84 W) were evaporating flows. Data were collected for the 13 power levels in a randomized order. The pressure at the outlet of the microchannel measured $105.2 \pm 0.8$ kPa, which is slightly elevated relative to the ambient pressure due to the flow resistance through the downstream tubing and heat exchanger. The higher power levels might be expected to result in a higher pressure drop across the microchannel (due to a higher evaporation-induced accelerational pressure drop); however, the range of power levels considered in this study is relatively small and thus minimal pressure drop increase was observed across the range. A steady-state condition was allowed to be reached at each successive power level before flow visualization images were obtained using the high-speed camera.

### 8.1.3 Flow Visualization

The flow was visualized using a high-speed camera (FASTCAM 1024 PCI, Photron) and two alternative lenses: a macro lens (AF Micro-Nikkor, Nikon) and a high-magnification zoom

lens (VH-Z50L, Keyence).  The camera and lens assembly was positioned using a three-axis stage and focused on the microchannel mid-plane.  The microchannel length was uniformly backlit using an adjustable, high-intensity LED strip with an integrated light diffuser (BL138, Advanced Illumination).

Images obtained using the macro lens were acquired at 27,000 frames per second with an exposure time of 0.037 ms for a duration of 0.74 s at each power level.  An image size of $1024 \times 32$ was used to visualize the high-aspect ratio microchannel geometry.  Images collected with the macro lens had an image resolution of 32 μm per pixel, as determined using a calibration target (59217, Edmund Optics).  The field of view observed with the macro lens was positioned at $98 < y/D < 162$; the beginning of the heated region was $y/D = 92$.  The entire vapor-liquid interface profile of several vapor bubbles could be visualized simultaneously within this field of view.

Images acquired using the high-magnification zoom lens were obtained at an image size of $1024 \times 512$ and resolution of 1.5 μm per pixel.  The frame rate was reduced to 2,000 frames per second (with an exposure time of 0.5 ms) to ensure adequate backlighting.  The high-magnification lens was used to measure the position of the vapor-liquid interface relative to the inside wall of the microchannel (*i.e.*, the liquid film thickness).

### 8.1.4   Image Analysis

Qualitative observations of the vapor-bubble interface were made using the images obtained with the macro lens.  The images were analyzed frame-by-frame to characterize the vapor bubble and liquid slug lengths.  These lengths were determined from the initial gray-scale images using a custom image-processing algorithm, as shown in Figure 8.2; the algorithm is shown in Appendix D.  The algorithm subtracts the original image (Figure 8.2a) from a

background image (Figure 8.2b) to generate an image of the vapor-liquid interface profile with enhanced contrast (Figure 8.2c). The gray-scale image was thresholded to yield a binary image (Figure 8.2d). Vapor bubbles featuring an incomplete vapor-liquid interface profile were then removed (Figure 8.2e). Finally, the interior of the vapor-liquid interface profiles are filled for easier visual study, resulting in a final image that can be used for extraction of the vapor bubble and liquid slug lengths (Figure 8.2f). Feature recognition was used to track each vapor bubble and liquid slug from frame to frame and identify new vapor bubbles entering the camera field of view.

The length of each vapor bubble was determined from the difference between the furthest downstream (*i.e.*, nose) and upstream (*i.e.*, tail) axial locations of the vapor-liquid interface. The liquid slug length was determined from the difference between the tail of a leading vapor bubble and the nose of a trailing vapor bubble. Optical distortions caused by the refraction of light passing through the liquid-solid interface and the gas-solid interface (*i.e.*, air-glass) need not be corrected when measuring the vapor bubble and liquid slug length because the liquid-solid and gas-solid interfaces at the centerline of the microchannel are normal to the camera.



Figure 8.2. Selected frame showing the (a) original image, (b) background image, (c) gray-scale image after background subtraction, (d) binary image after thresholding, (e) binary image after removing partial bubble interfaces, and (f) final binary image with vapor bubbles filled in white. The flow direction is from left to right.

### 8.1.5   Liquid Film Thickness

Liquid film thickness is an important parameter in the characterization of two-phase flows, resulting in significant effort having been directed toward predictive correlations and improved measurement techniques [72, 73].  While sophisticated experimental techniques involving laser focus displacement meters [74, 75] and optical microscopes paired with pulsed-laser illumination [76] have been used for high-fidelity characterization of the liquid film interface profile, the flow visualizations obtained via high-speed imaging herein can also yield a film thickness measurement.  The thickness of the liquid film separating the vapor bubble from the inside microchannel wall was quantified using the images obtained with the high-magnification zoom lens.  The measurement of this liquid film thickness accounts for the optical distortions in the images; a schematic diagram illustrating the optical distortions caused by the liquid-solid and gas-solid interfaces is shown in Figure 8.3.  To illustrate the relationship between the image and physical interface locations, a quarter section of the microchannel cross-section is shown side-by-side with an image obtained using high-speed imaging, aligned at the channel centerline.  Key locations along the interfaces are marked with dots; outward pointing arrows indicate the direction normal to the interfaces at these locations.  The dotted lines represent the pathlines of light collected by the high-speed camera from the points of interest at the microchannel $y$-$z$ mid-plane; the dashed lines show the $x$- and $z$-positions where the light is refracted along these pathlines.

A ray-tracing procedure was used to transform the imaged $z$-positions of the microchannel inside diameter ($z_5$) and the vapor-liquid interface ($z_6$) to the actual physical positions of these two interfaces ($z_2$ and $z_1$, respectively).  The analysis assumes the liquid film thickness to be uniform around the microchannel circumference.  The dominance of surface

tension forces relative to body forces, as indicated by a Bond number of Bo = 0.24 < 1, justifies this assumption.

The vapor-liquid interface intersects the microchannel *x-y* mid-plane at the top of a dark band in the image shown Figure 8.3; this vapor-liquid interface was used for the ray-tracing procedure. This dark region observed below the mid-plane vapor-liquid interface location is a result of the light being refracted by a region of the foreground/background interface. The location of the microchannel inside diameter is difficult to observe, but is made detectable using image-enhancement techniques. The relationship between the angle of incidence and refraction of the light traversing through the liquid-solid and gas-solid interfaces is given by Snell's Law: $n_a\sin\theta_a = n_b\sin\theta_b$, where *n* is the index of refraction of the medium and $\theta$ is the angle between the normal and the incident/refracted light. The refractive indices of HFE-7100 liquid, borosilicate glass, and air are 1.27, 1.47, and 1.00, respectively.
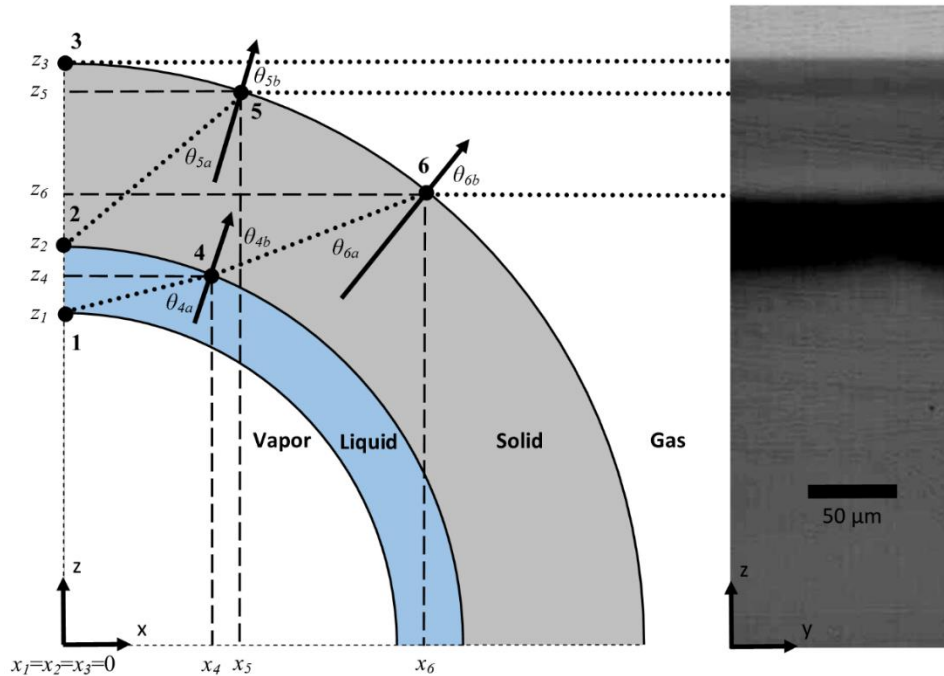
Figure 8.3. Schematic diagram illustrating optical distortions caused by the liquid-solid and gas-solid interfaces; the relationship between the image obtained and key physical interface locations is shown.

## 8.2    Results and Discussion

### 8.2.1    Heat Loss Analysis

A portion of the total power supplied to the ITO coating on the microchannel outer surface is lost to the ambient (*i.e.*, not transferred to the flow through the microchannel wall). Any energy supplied to (removed from) a saturated two-phase flow would change the vapor quality and thus be observed as a streamwise increase (decrease) in the vapor bubble size. Under adiabatic conditions, the size of the vapor bubbles would remain constant. The heat loss to the ambient was quantified by measuring the nondimensional change in vapor bubble length, $\Delta L_b/D$, over a given period of time, for each of the 13 power levels, to identify the power level at which no net evaporation or condensation was occurring. The nondimensional change in vapor bubble length for the 13 different power levels is plotted in Figure 8.4 with error bars indicating one

standard deviation. A zero net change in nondimensional vapor bubble length, as determined from the linear regression line, occurs at a power input of $0.39 \pm 0.01$ W. Because this power input level results in no change in the vapor bubble length, it is deemed to be all lost to the ambient. Hence, the power loss to the ambient, $P_{loss} = 0.39 \pm 0.01$ W; the uncertainty in $P_{loss}$ was quantified based on the uncertainty in the linear regression [77]. For the range of power levels considered in this study, a linear relationship between total power and nondimensional change in vapor bubble length was observed ($R^2 = 0.98$); hence, the power input to the microchannel, $P_{in}$, in each case was determined by subtracting the power loss from the total power.

The heat flux into the fluid is $q_{in} = P_{in}/A_s$, where $A_s$ is the internal surface area of the microchannel. The uncertainty in $P_{in}$ has contributions from uncertainties in the heat loss determined via linear regression and the total power measurement. The uncertainty in $A_s$ has contributions from the uncertainties in the microchannel inside diameter ($\pm 4$ μm) and the distance between the electrical connections on the ITO layer ($\pm 1$ mm). The resultant propagated uncertainty in the heat flux increases slightly from 150 to 190 W/m$^2$ over the range of evaporating heat fluxes from 30 to 5160 W/m$^2$. The large relative uncertainty at $q_{in} = 30$ W/m$^2$ is attributed to the small difference between the total power and the heat loss at this test condition.
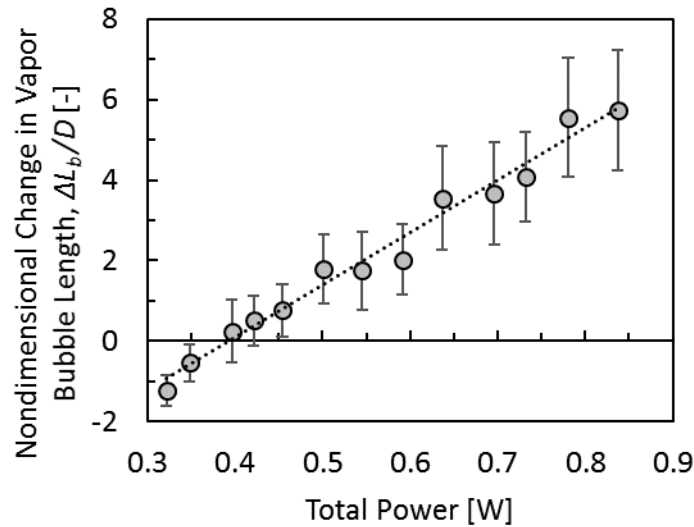
Figure 8.4. The nondimensional change in vapor bubble length at varying input powers to the ITO microchannel coating; heat loss to the ambient is quantified as the intercept with the horizontal axis.

### 8.2.2    Qualitative Flow Visualizations

Selected images from high-speed visualization of the test section microchannel at heat fluxes of $q_{in} = 30$ W/m$^2$ and $q_{in} = 3520$ W/m$^2$ are shown in Figure 8.5.  The sequence of frames at each heat flux shows the left-most vapor bubble (in the first frame) traverse the length of the microchannel until it almost begins to exit the camera field-of-view.  Visualization of the evaporating two-phase slug flow allows several important qualitative features to be identified for the inlet conditions of this study:

  i.   the vapor bubble nose is hemispherical while the tail is much flatter;

 ii.   the liquid film between the vapor bubble and the microchannel wall slightly reduces along the length of the vapor bubbles beginning at the nose and progressing toward the tail;

iii.   the interface at the trailing edge of the vapor bubble fluctuates in time as a result of the recirculation in the wake of the vapor bubble;

iv.  capillary waves are observed on the vapor-liquid interface where the liquid film is thinnest;

v.  vapor bubbles elongate in time as they evaporate due to the uniform heat flux condition;

vi.  longer vapor bubbles elongate at a faster rate than shorter ones as a result of their increased vapor-liquid interfacial surface area;

vii.  vapor bubble growth only occurs in the streamwise direction because the vapor bubbles are confined in circumferential extent by the microchannel wall;

viii.  the variation in length between successive vapor bubbles is small, as it is for the liquid slugs;

ix.  the initial length of the liquid slugs is slightly larger than the initial length of the vapor bubbles;

x.  the length of the liquid slugs does not noticeably change as a function of axial position along the microchannel;

xi.  flow-regime transitions (*e.g.*, slug to annular) and flow instabilities (*e.g.*, flow reversal) are not observed;

xii.  there are no instances of vapor bubble coalescence; and

xiii.  there is no nucleation of vapor bubbles from the microchannel wall.
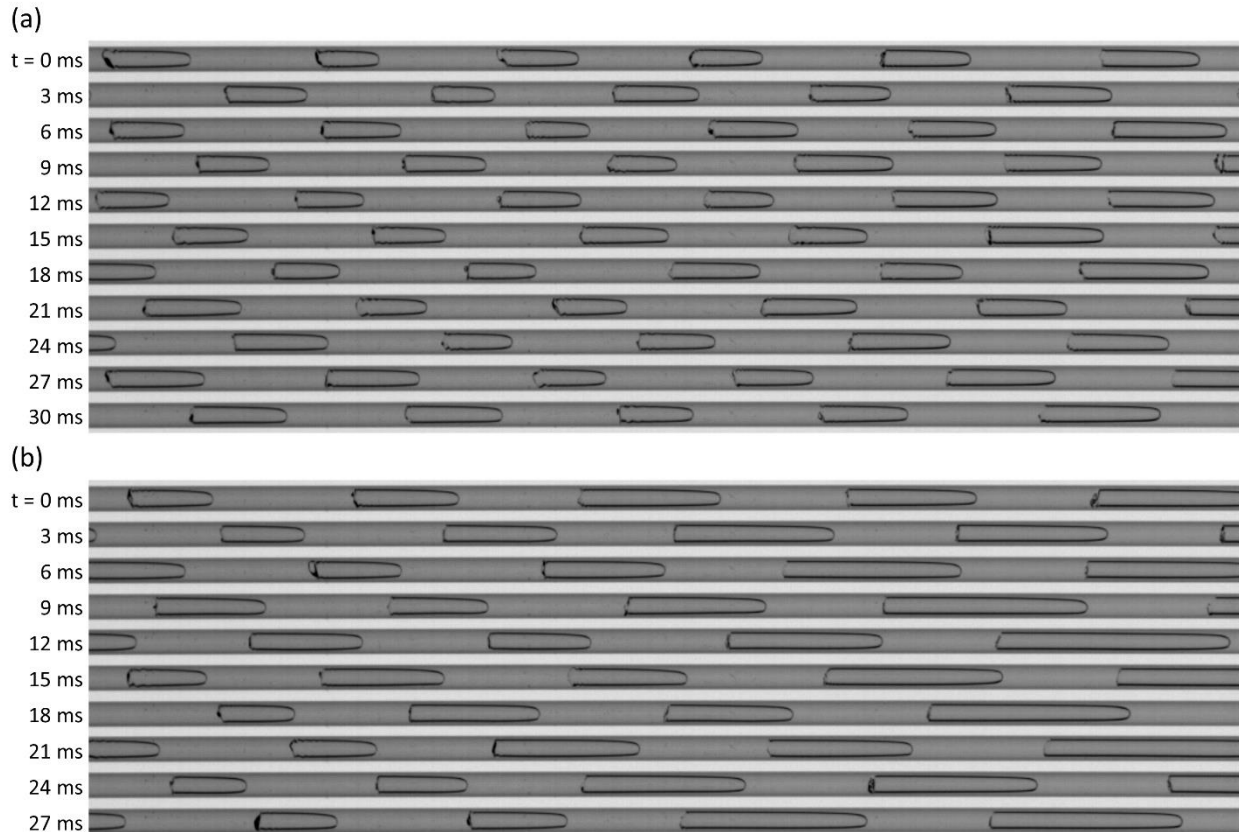
Figure 8.5. Selected images at 3 ms increments obtained from high-speed imaging at heat fluxes of (a) $q_{in} = 30$ W/m$^2$ and (b) $q_{in} = 3520$ W/m$^2$. The flow direction is from left to right.

Qualitative differences between Figure 8.5a and 20b due to the different heat fluxes applied can also be observed. The vapor bubbles in Figure 8.5a elongate at a much slower rate than those in Figure 8.5b as a result of the reduced heat flux and the lower associated rate of evaporation. Also, the time required for a vapor bubble in Figure 8.5a to translate a given distance downstream is longer than in Figure 8.5b (note the additional frame in Figure 8.5a). An increased evaporation rate results in an increased acceleration of the flow due to volumetric expansion associated with phase change from liquid to vapor.

To further illustrate the controlled nature of the slug flow generation methodology developed in this work, alternative images from high-speed visualization of vapor bubbles being generated by nucleation from the wall within a heated microchannel and the downstream slug

flow regime in this case are shown in Figure 8.6. Vast differences in the hydrodynamics are observed for this flow regime generated using an approach where preheated single-phase liquid entered the heated channel and was allowed to nucleate.
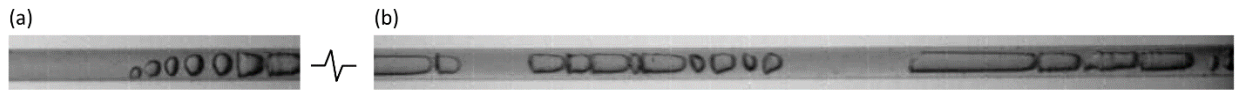


Figure 8.6. High-speed visualization of (a) vapor bubbles nucleating from a heated microchannel wall and (b) the resulting downstream slug flow.

### 8.2.3 Quantitative Characterization

#### 8.2.3.1 Vapor Bubble and Liquid Slug Uniformity

The uniformity of the vapor bubble and liquid slug lengths was quantitatively assessed from the images obtained for the evaporating flow test cases (*i.e.*, a positive net heat flux to the microchannel). The initial lengths of the vapor bubbles were measured when the entire vapor-liquid interface profile first comes into view. This occurs at a fixed vapor bubble tail location of $y'/D = 0.06$, where $y'$ is the axial position along the microchannel beginning at the upstream end of the camera field-of-view; this ensured that a liquid region could be clearly observed at $y'/D = 0$. Similarly, the initial liquid slug length was measured once the entire liquid slug could be observed. The average initial vapor bubble and liquid slug lengths for each heat flux are shown in Figure 8.7a. The error bars represent one standard deviation for all of the vapor bubbles and liquid slugs that were analyzed. Histograms illustrating the lengths of each vapor bubble and liquid slug that were observed at a heat flux of $q_{in} = 3520$ W/m$^2$ are shown in Figure 8.7b and 8.7c, respectively. The histograms indicate a generally normal distribution with no outliers. The average initial length of the liquid slugs ($L_0/D = 6.8$) is longer than the average initial length of the vapor bubbles ($L_0/D = 4.6$). An average of 113 vapor bubbles was observed over the 0.74 s acquisition period. The average standard deviation in the length of the liquid

slugs ($L_0/D = 0.9$) is smaller than the average standard deviation in the length of the vapor

bubbles ($L_0/D = 1.1$). This less consistent vapor bubble length results from minuscule variations

in flow conditions (*e.g.*, inlet temperatures) that preferentially magnify vapor bubble

characteristics relative to the liquid slugs because of the high liquid to vapor density and specific

heat ratios.

An ideal slug flow regime for the purpose of validating mechanistic models should

feature liquid slug lengths that are large enough to prevent vapor bubble coalescence and a

subsequent transition from slug to annular flow. Likewise, the liquid slug length must not be so

long that the flow regime is essentially that of single-phase liquid flow with isolated vapor

bubbles present. The ability to produce a slug flow regime that resembles archetypal

microchannel slug flow by independently injecting vapor and liquid thereby removing a reliance

on nucleation from the microchannel wall is unique to this test facility and, to the authors'

knowledge, is the only such demonstration in the literature for a single-component, two-phase

diabatic flow.

The range in the average initial vapor bubble length across the different heat fluxes is

relatively small ($L_0/D = 0.9$), being less than one standard deviation in the average vapor bubble

length. This small variation confirms that the slightly increased pressure drop across the

microchannel at the higher heat fluxes does not result in significant changes in the vapor flow

rate through the vapor flow control valve. The vapor flow control valve relies on a pressure

difference upstream and downstream of the control valve, unlike the liquid flow controller,

which employs active feedback to regulate the flow rate.
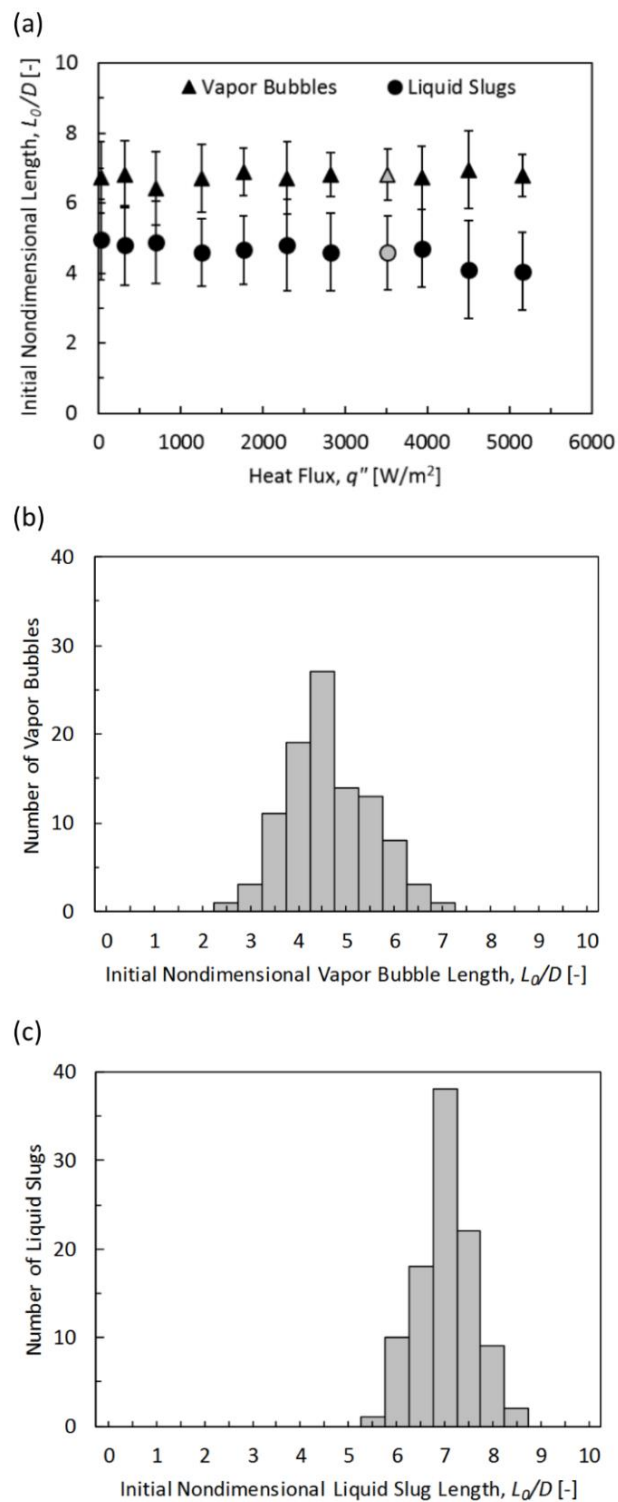
Figure 8.7. The (a) average vapor bubble and liquid slug length for each heat flux and histograms of all (b) vapor bubble and (c) liquid slug lengths observed at a heat flux of $q_{in} = 3520$ W/m$^2$ (gray symbols in Figure 8.7a).

**8.2.3.2   Local Velocity Evaluation**

The accelerating flow resulting from evaporation yields a unique velocity at each axial

location and requires the flow characteristics to be quantified locally.  The average vapor bubble

velocity was computed by determining the velocity of each vapor bubble and then averaging

across all vapor bubbles at a given heat flux.  The velocity was measured by determining the

time between the first and last detection point of the vapor bubble in the camera field of view;

the midpoint between the vapor bubble nose and tail was used as the detection point.  A

corresponding average Reynolds number, $Re_D = \overline{V_b}D/\nu_l$, was calculated using the vapor bubble

velocity, following prior practice for microchannel slug flow in the literature [75].  The average

vapor bubble velocity and Reynolds number for four selected heat fluxes are shown in Table 8.1.

Table 8.1. Average vapor bubble velocity and corresponding average Reynolds number.

| Heat Flux, $q_{in}$ [W/m$^2$] | Average Vapor Bubble Velocity, $\overline{V_b}$ [m/s] | Average Reynolds Number, $Re_D$ [-] |
|---|---|---|
| 30 | 0.89 | 1650 |
| 1250 | 0.91 | 1690 |
| 3520 | 0.93 | 1720 |
| 5160 | 0.94 | 1740 |

**8.2.3.3   Film Thickness Quantification**

The liquid film thickness was measured using the high-magnification zoom lens at the

heat flux of 3520 W/m$^2$ as described in Section 8.1.3.  While the thickness of the liquid film is

known to depend on the vapor bubble velocity, only minor changes in velocity were observed for

the different heat fluxes; thus, only one heat flux condition was analyzed.  The ray-tracing

procedure described in Section 8.1.5 yielded the physical $z$-positions of the microchannel inside

wall and the vapor-liquid interface to be $z/D = 0.490 \pm 0.008$ and $z/D = 0.416 \pm 0.016$,

respectively; the uncertainties represent a propagation of the image resolution and interface

location uncertainty (interfaces can be located in the image within ± 1 pixel). A dimensionless

liquid film thickness of $\delta/D = 0.074 \pm 0.018$ resulted.

The current approach does not capture the precise axial location at which the film

thickness is measured along the vapor bubble relative to its nose or tail. Due to the relatively

low frame rate used with the high-magnification zoom lens, the nose and tail of the vapor bubble

blur in the images due to rapid translation of the interface across the field of view in the axial

direction. For the average vapor bubble velocity of 0.93 m/s, the vapor-liquid interface translates

0.93D (30% of the image width) during the 0.5 ms exposure time. The interface is therefore

visualized in the middle region of the bubble over which the film thickness is approximately

constant (along the axial direction); image blur is not observed because the interface appears

stationary within the exposure time.

### 8.2.3.4  Vapor Bubble Growth

The growth of individual vapor bubbles provides a measure of the evaporation rate. A

Lagrangian approach which tracks the growth of individual vapor bubbles with time was chosen.

The average nondimensional vapor bubble length versus time is shown in Figure 8.8 for four

selected heat fluxes considered in this study. The minimum and maximum heat flux levels

($q_{in} = 30$ W/m$^2$ and $q_{in} = 5160$ W/m$^2$, respectively) and two intermediate heat flux levels

($q_{in} = 1250$ W/m$^2$ and $q_{in} = 3520$ W/m$^2$) are included; the other intermediate heat fluxes have

been left out of Figure 8.8 for clarity. The error bars represent one standard deviation in the

nondimensional vapor bubble length for all of the vapor bubbles analyzed at a given heat flux.

The lengths were measured in each frame (at 0.037 ms increments); these high-resolution data

are shown as lines in Figure 8.8. A nondimensional vapor bubble length of $L_b/D = 5$ was chosen

as a common starting length in Figure 8.8 because it enabled the most vapor bubbles to be

analyzed given that the average initial vapor bubble length was slightly less than $L_b/D = 5$. For a heat flux of $q_{in} = 30$ W/m$^2$, a small rate of evaporation results in an average elongation of the vapor bubbles from $L_b/D = 5$ to $L_b/D = 5.2$ in 18 ms. At the highest heat flux of $q_{in} = 5160$ W/m$^2$, a much larger evaporation rate elongates the vapor bubble to $L_b/D = 10.7$ over this same period. The intermediate heat flux levels of $q_{in} = 1250$ W/m$^2$ and $q_{in} = 3520$ W/m$^2$ resulted in vapor bubble lengths elongating to $L_b/D = 6.8$ and $L_b/D = 8.7$, respectively. The vapor bubble growth is monotonic with heat flux for all test cases.
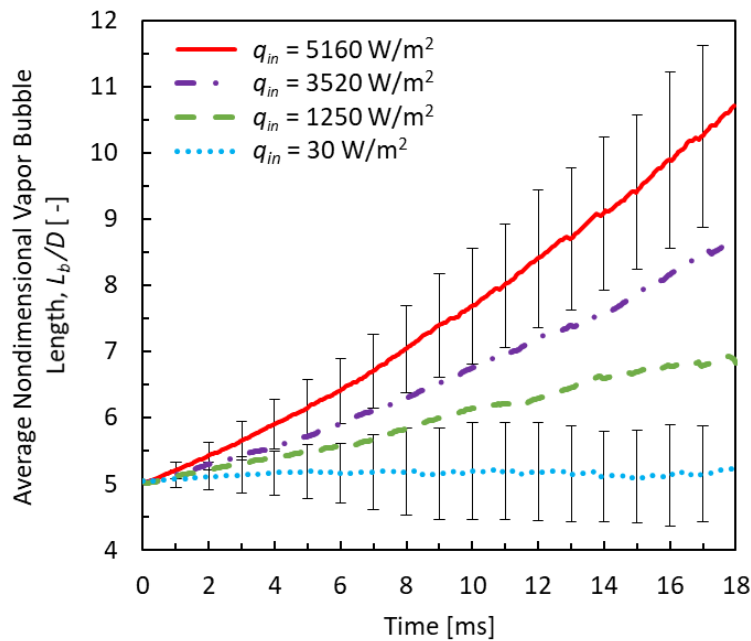


Figure 8.8. The average growth of vapor bubbles, as indicated by the nondimensional vapor bubble length as a function of time, for four heat flux levels. The growth is shown from a common starting bubble length of $L_b/D = 5$.

To evaluate the dependence of the growth rate on the vapor bubble length, a second-order polynomial trendline was first fit to the vapor bubble length versus time data for each heat flux; all trendlines had $R^2 > 0.99$. The polynomial was differentiated with respect to time to yield the time rate of change of the average nondimensional vapor bubble length and then plotted against

the average nondimensional vapor bubble length (Figure 8.9).  As shown, the time rate of change

in length is higher for higher heat fluxes and increases with increasing vapor bubble length (*i.e.*,

evaporation rate increases with a larger interfacial area).
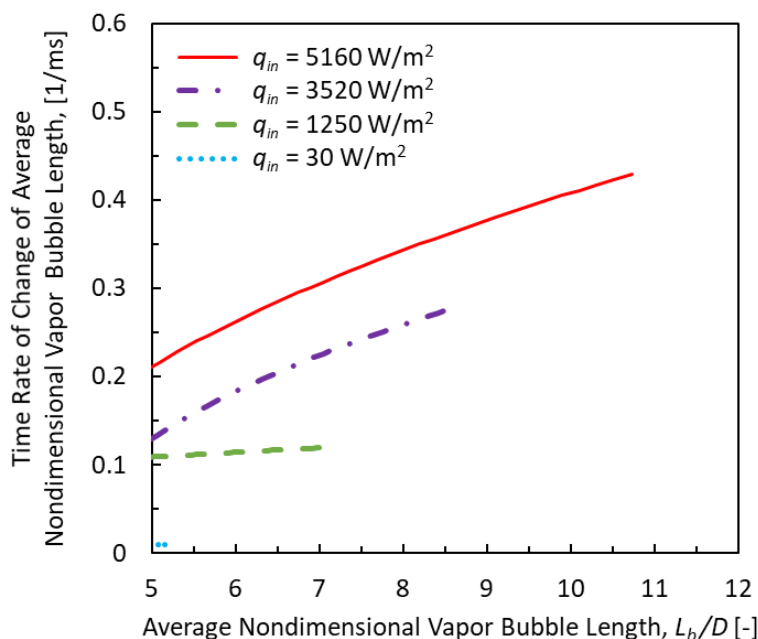


Figure 8.9. The time rate of change of the vapor bubble length as a function of the vapor bubble
length for four heat flux levels.

## 8.3    Conclusions

An archetypal microchannel slug flow boiling regime was generated by independently

injecting HFE-7100 vapor and liquid into a T-junction using a novel experimental test facility.

This approach does not rely on nucleation from the microchannel wall to generate the vapor

phase, thereby eliminating flow instabilities, flow-regime transitions, and undesirably close

proximity of successive vapor bubbles to each other.  The two-phase flow was subjected to a

constant heat flux ranging from 30 W/m$^2$ to 5160 W/m$^2$.  High-speed flow visualization was used

to quantitatively characterize the vapor bubble and liquid slug uniformity and vapor bubble

growth.  High-magnification imaging was demonstrated for quantifying the liquid film thickness

using a ray-tracing procedure to account for optical distortions. This study provides a foundation for experimental investigation of microchannel slug flow boiling under conditions suitable for model validation.

# 9   CONCLUSIONS AND FUTURE WORK

The overall goal of this work was to advance the state of the art of microchannel flow boiling technologies for the thermal management of electronic devices.  Specifically, this work furthered our understanding of flow boiling instabilities and their implications on the operating characteristics of electronic devices, particularly when subjected to transient and non-uniform heating conditions.  The primary conclusions from this work are summarized in this chapter, followed by suggestions for future work.

## 9.1   Conclusions

In Chapter 3, the effect of flow inertia and inlet liquid subcooling on the rapid-bubble-growth instability at the onset of boiling is assessed and the following conclusions are drawn:

- The mechanisms underlying the rapid-bubble-growth instability are large liquid superheat and a large pressure spike.

- Low flow inertia exacerbates the rapid-bubble-growth instability by starving the heated channel of liquid replenishment for longer durations than conditions with higher flow inertia and results in severe temperature increases.

- For high flow inertia or high inlet liquid subcooling, flow reversal is still observed at the onset of boiling, but results in a minimal wall temperature rise because liquid quickly replenishes the heated channel.

In Chapter 4, the effect of operating conditions, specifically flow inertia, inlet liquid subcooling, and heat flux, on the instability type and the resulting time-periodic hydrodynamic and thermal oscillations are studied, enabling the following conclusions to be drawn:

- Two predominant dynamic instabilities are observed: a time-periodic series of rapid-bubble-growth instabilities and the pressure drop instability.

- High inlet liquid subcoolings and low heat fluxes result in time-periodic transitions between single-phase flow and flow boiling, and a series of rapid-bubble-growth instabilities, which induce large-amplitude wall temperature oscillations.

- Low inlet liquid subcoolings result in small-amplitude thermal-fluidic oscillations and the pressure drop instability.

- Low flow inertia exacerbates the pressure drop instability and results in large-amplitude thermal-fluidic oscillations whereas high flow inertia reduces the severity of the oscillations.

Chapter 5 investigates the Ledinegg instability in two thermally isolated, heated parallel channels and draws the following conclusions:

- Boiling incipience in one of the channels triggers the Ledinegg instability which induces a temperature difference between the two channels due to flow maldistribution.

- The temperature difference between the two channels grows with increasing power until boiling incipience occurs in the second channel, at which point the wall temperatures of both channels reduce significantly as the flow becomes more evenly distributed.

In Chapters 6 and 7, time-resolved characterization of the dynamic flow boiling response in a single microchannel was performed. Three different heat flux levels that exhibit highly contrasting flow behavior during constant heating conditions were selected to perform transient

heating tests: a low heat flux corresponding to single-phase flow (15 kW/m$^2$), an intermediate heat flux corresponding to continuous flow boiling (75 kW/m$^2$), and a very high heat flux which would cause critical heat flux if operated at this heat flux continuously (150 kW/m$^2$). In Chapter 6, the response to a single heat flux pulse was investigated and the following conclusions were drawn:

- Any step up/down in the heat flux level that induces/ceases boiling causes the temperature to temporarily over/under-shoot the eventual steady temperature.

- When initially in the single-phase flow regime, a high-heat-flux pulse induces boiling and leads to rapid evaporation of the liquid in the microchannel, which significantly reduces the flow rate of incoming liquid, and results in a large temperature spike.

- When initially under time-periodic boiling conditions, a high-heat-flux pulse significantly increases the frequency of a pressure drop instability due to vapor nucleating near the channel inlet.

- A longer duration high-heat-flux pulse can be sustained when time-periodic boiling is initially occurring in the microchannel, relative to initially being single-phase flow, despite being at an initially higher heat flux and wall temperature prior to the pulse.

In Chapter 7, the dynamic flow boiling response to a time-periodic series of heat flux pulses is investigated and the following conclusions were drawn:

- Three different time-periodic flow boiling fluctuations were observed:  flow regime transitions, pressure drop oscillations, and heating pulse propagation.

- For heat flux pulses between 15 and 75 kW/m$^2$ and heating pulse frequencies above 1 Hz, time-periodic flow regime transitions between single-phase and two-phase flow were reported.

- For heating pulse frequencies between approximately 1 and 10 Hz, the thermal and flow fluctuations are heavily coupled to the heating characteristics, forcing the pressure drop instability frequency to match the heating frequency.

- For heating pulse frequencies above 25 Hz, the microchannel wall attenuates the transient heating profile and the fluid essentially experiences a constant heat flux.

- The observed dependence of flow instabilities and thermal performance on time-varying heating conditions indicates that flow boiling dynamics significantly influence overall performance.

Chapter 8 details the use of a novel experimental test facility that generates an archetypal slug flow regime, devoid of flow instabilities, to perform high-fidelity characterization of key hydrodynamic and heat transfer parameters and draw the following conclusions:

- High-speed flow visualization can be used to quantify vapor bubble growth under varying heat flux boundary conditions.

- The liquid film thickness can be accurately measured using high-magnification imaging and a ray-tracing procedure to correct for optical distortions.

- The novel slug flow generation facility has the capability to provide high-fidelity experimental data that can be used to validate mechanistic flow boiling models.

**9.2    Suggested Future Work**

Opportunities to further build upon the present work include:

- Most if not all of the previous flow boiling studies involving transient heating conditions utilize idealized heating profiles.  More interesting and applicable would be to investigate the effects of application-specific transient heating conditions, such as those encountered in Naval radar systems or automotive power electronics, on flow boiling instabilities and performance.  Efforts are currently being directed to this topic in collaobration with Naval Surface Warfare Center Crane Divison.

- While the effect of flow boiling instabilities on wall temperature and the resulting heat transfer coefficient has been to investigate, it is relatively unknown how these instabilities affect critical heat flux beyond speculation.  Future studies should aim to quantify the reduction in critical heat flux resulting from flow instabilities and develop means to mitigate these effects.

- As embedded cooling become more attractive to cooling high-heat-flux electronic devices, the coupling between device operating characteristics and the cooling system become important.  Studies that minimize the thermal resistance between active electrical devices and next-generation thermal management systems and characterize this coupling will certain provide new, interesting insight.

- Predicting the onset and severity of flow boiling instabilities remains a challenge.  Further experimental investigations that probe the mechanisms governing these instabilities will aid in developing mechanistic modeling capabilities that can assess the impact of flow boiling instabilities on thermal performance.

- Flow boiling modeling capabilities currently lack experimental validation. The unique ability to generate an archetypal slug flow boiling regime using the test facility developed in this work provides the ability to experimentally characterize and tabulate high-fidelity hydrodynamic and heat transfer data for a range of operating conditions. Experimentally-obtained operating conditions can then be extracted and fed into mechanistic flow boiling models to experimentally them. Experimental data obtained using the test facility and methods described in this work are currently be used to validate a state-of-the-art phase change model in collaboration with Prof. Zhenhai Pan at Shanghai Jiao Tong University.

# APPENDIX A.  EFFECT OF INLET LIQUID SUBCOOLING ON OSCILLATION AMPLITUDE AND FREQUENCY

The normalized pressure drop oscillation amplitude ($\Delta\tilde{p}_{osc,amp}/\Delta p_{avg}$), mass flux oscillation amplitude ($\Delta\widetilde{G}_{osc,amp}/\Delta G_{avg}$), wall temperature oscillation amplitude ($\tilde{T}_{wall,osc,amp}$), and their corresponding oscillation frequency($f$) (defined in Section 4.1) in the measured thermal-fluidic signatures for the three inlet liquid subcoolings and all heat fluxes resulting in two-phase flow are shown in Figure A.1 for a fixed $G_{1\phi} = 400$ kg/m$^2$s.  Data points corresponding to single-phase flow are omitted because the oscillation amplitudes are negligible and oscillation frequencies are random.

The most significant effects are in the wall temperature oscillation amplitude (Figure A.1c).  At $q_{in,avg} \leq 59.7$ kW/m$^2$ for $\Delta T_{sub} = 15$ °C (purple circles in Figure A.1c), the wall temperature oscillation amplitude ($\tilde{T}_{wall,osc,amp}$) is significantly larger (19-54 °C), due to the time-periodic series of rapid-bubble-growth instabilities.  At $q_{in,avg} \geq 67.5$ kW/m$^2$, the wall temperature oscillation amplitude is less than 3 °C (similar to cases for $\Delta T_{sub} = 5$ °C) because the instability type changes to the pressure drop instability.  Similarly, for $q_{in,avg} \leq 67.9$ kW/m$^2$ at $\Delta T_{sub} = 35$ °C (orange circles in Figure A.1c), the wall temperature oscillation amplitude is significantly larger (16-55 °C).  At $q_{in,avg} \geq 73.5$ kW/m$^2$, the wall temperature oscillation amplitude reduces to less than 4 °C because, again, the instability type changes to the pressure drop instability.

The wall temperature oscillation frequency (Figure A.1f) exactly matches that of the hydrodynamic oscillations frequencies for $q_{in,avg} \leq 55.5$ kW/m$^2$ (corresponding to $f \leq 13$ Hz), above which the thermal capacitance of the wall likely damps the thermal oscillations resulting in low-frequency oscillations ($f < 2$ Hz).

The normalized pressure drop oscillation amplitude (Figure A.1a) is significantly larger

for $\Delta T_{sub}$ = 15 °C and 35 °C, relative to $\Delta T_{sub}$ = 5 °C.  These large values for $\Delta T_{sub}$ = 15 °C and

35 °C stem from (i) larger pressure drop oscillation amplitudes, and (ii) lower time-averaged

pressure drops (as shown in Figure 4.2c) because of the lower flow resistance resulting from a

shorter length of the channel being occupied by vapor in these cases (as more sensible heating is

needed to bring the liquid to the saturation temperature) thereby reducing the flow resistance.

For all inlet liquid subcoolings, the normalized pressure drop oscillation amplitude decreases

slowly with increasing heat flux.  The corresponding pressure drop oscillation frequency (Figure

A.1d) is much smaller for $\Delta T_{sub}$ = 15 °C and 35 °C than $\Delta T_{sub}$ = 5 °C, particularly at low heat

fluxes where the time-periodic series of rapid-bubble-growth instabilities is observed (circles in

Figure A.1).

For all inlet liquid subcoolings, the pressure drop oscillation frequency increases with

increasing heat flux, with a jump from very low-frequency oscillations to higher-frequency

oscillations when the instability changes from a time-periodic series of rapid-bubble-growth

instabilities to the pressure drop instability for $\Delta T_{sub}$ = 15 °C and 35 °C.

Despite differences in the pressure drop oscillation characteristics, the normalized mass

flux oscillation amplitudes (Figure A.1b) are similar for all three inlet liquid subcoolings.  All

three cases show a slight increase in normalized oscillation amplitude with increasing heat flux

because of a continual increase in the mass flux oscillation amplitude and a continual decrease in

the time-average mass flux (as shown in Figure 4.2d).

The characteristic frequencies of the mass flux oscillations (Figure A.1e) are nearly

identical to those of the pressure drop (Figure A.1d), and are significantly lower for the larger

$\Delta T_{sub}$ = 15 °C and 35 °C than at $\Delta T_{sub}$ = 5 °C.  The time-averaged increase in void fraction within

the channel for $\Delta T_{sub} = 5$ °C relative to $\Delta T_{sub} = 15$ °C and 35 °C likely causes the increase in the hydrodynamic (pressure drop and mass flux) oscillation frequency when the pressure drop instability is observed.
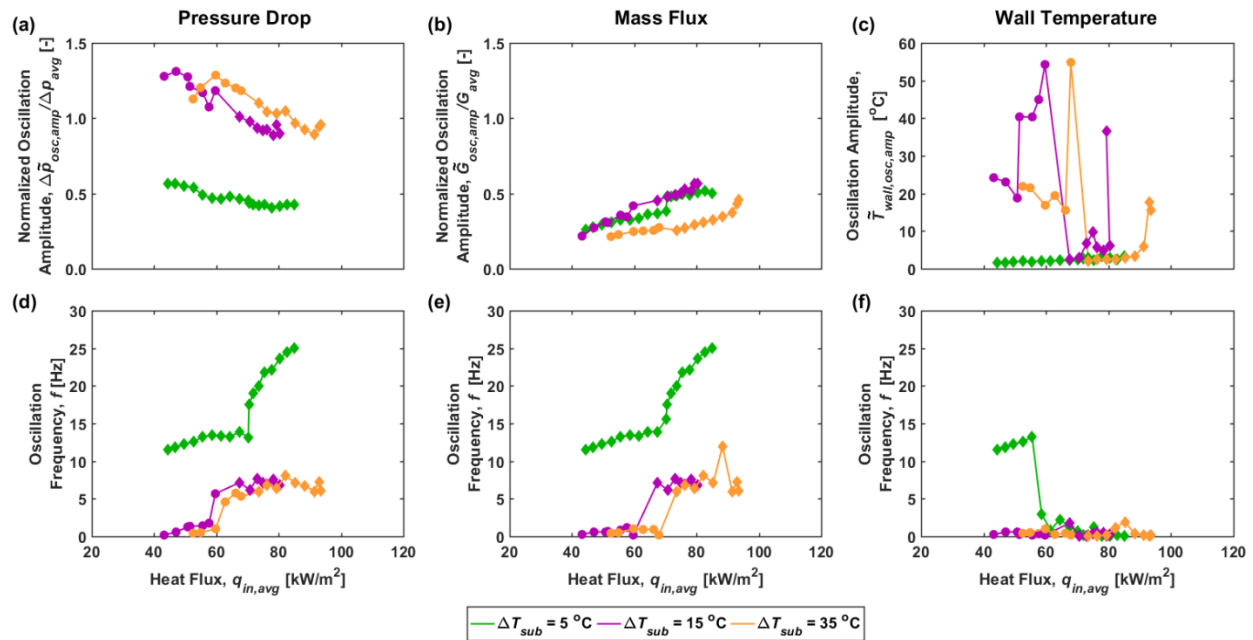


Figure A.1.  The (a) normalized pressure drop oscillation amplitude, (b) normalized mass flux oscillation amplitude, (c) thermal oscillation amplitude, and (d-f) characteristic oscillation frequency in the measured signals of pressure drop, mass flux, and wall temperature, are shown as a function of heat flux for $\Delta T_{sub} = 5$, 15, and 35 °C at a fixed $G_{1\phi} = 400$ kg/m$^2$s.  Diamond symbols (♦) denote flow-boiling operating conditions where the pressure drop instability was observed.  Circles (●) denote flow-boiling operating conditions where a time-periodic series of rapid-bubble-growth instabilities was observed.

# APPENDIX B.    EFFECT OF FLOW INERTIA ON OSCILLATION AMPLITUDE AND FREQUENCY

The level of flow inertia significantly affects the amplitude of the hydrodynamic oscillations but has less effect on the thermal oscillations during flow boiling.  The normalized pressure drop oscillation amplitude ($\Delta \tilde{p}_{osc,amp}/ \Delta p_{avg}$), mass flux oscillation amplitude ($\Delta \widetilde{G}_{osc,amp}/ \Delta G_{avg}$), wall temperature oscillation amplitude ($\tilde{T}_{wall,osc}$), and their corresponding characteristic oscillation frequency ($f$) (defined in Section 4.1) in the measured thermal-fluidic signatures are shown in Figure B.1 at the three nominal single-phase mass fluxes and all heat fluxes resulting in two-phase flow for a fixed $\Delta T_{sub} = 5$ °C.  Figures B.1a - B.1c and the insets in Figures B.1d – B.1f are plotted on the same axes as Figure A.1 to enable a quantitative comparison of the oscillation amplitude and frequencies.  Data corresponding to single-phase flow are again omitted as before.

The lowest level of flow inertia (*i.e.*, $G_{1\phi} = 200$ kg/m$^2$s) exacerbates the pressure drop instability and results in large normalized pressure drop and mass flux oscillation amplitudes for all heat flux levels (as shown in Figures B.1a and B.1b), compared to $G_{1\phi} = 400$ and $800$ kg/m$^2$s. The wall temperature oscillations are also slightly larger for all heat flux levels for $G_{1\phi} = 200$ kg/m$^2$s, compared to $G_{1\phi} = 400$ and $800$ kg/m$^2$s, particularly for $q_{in,avg} = 41.2 - 51.0$ kW/m$^2$.

The pressure drop (Figure B.1d) and mass flux (Figure B.1e) characteristic oscillation frequencies are identical to each other for all operating conditions featuring the pressure drop instability (diamond symbols in Figure B.1).  A gradual increase in the hydrodynamic characteristic oscillation frequency with increasing heat flux is observed for $G_{1\phi} = 200$ and $400$ kg/m$^2$s.  The wall temperature oscillation frequency (Figure B.1f) increases with increasing heat flux for $G_{1\phi} = 200$ and $400$ kg/m$^2$s and exactly matches the hydrodynamic oscillation

frequencies for $q_{in,avg} \leq 37.7$ kW/m$^2$ and $q_{in,avg} \leq 55.5$ kW/m$^2$ (corresponding to $f \leq 9$ and 13 Hz, respectively). Above these heat flux levels, the characteristic wall temperature oscillation frequency switches to lower frequencies, likely due to damping by the thermal capacitance of the wall.

The two lowest heat fluxes at $G_{1\phi} = 800$ kg/m$^2$s that yield two-phase flow ($q_{in,avg} = 38.1$ kW/m$^2$ and 40.5 kW/m$^2$) have significantly lower pressure drop and mass flux oscillation amplitudes (Figures B.1a and B.1b) compared to all other operating conditions. Additionally, their pressure drop characteristic frequencies are extremely high (142.1 Hz and 126.2 Hz, respectively), while the mass flux oscillation frequencies are extremely low (essentially zero). This behavior is due to the suppression of the pressure drop instability (as shown in Figure 4.8a) at high levels of flow inertia and low heat fluxes.
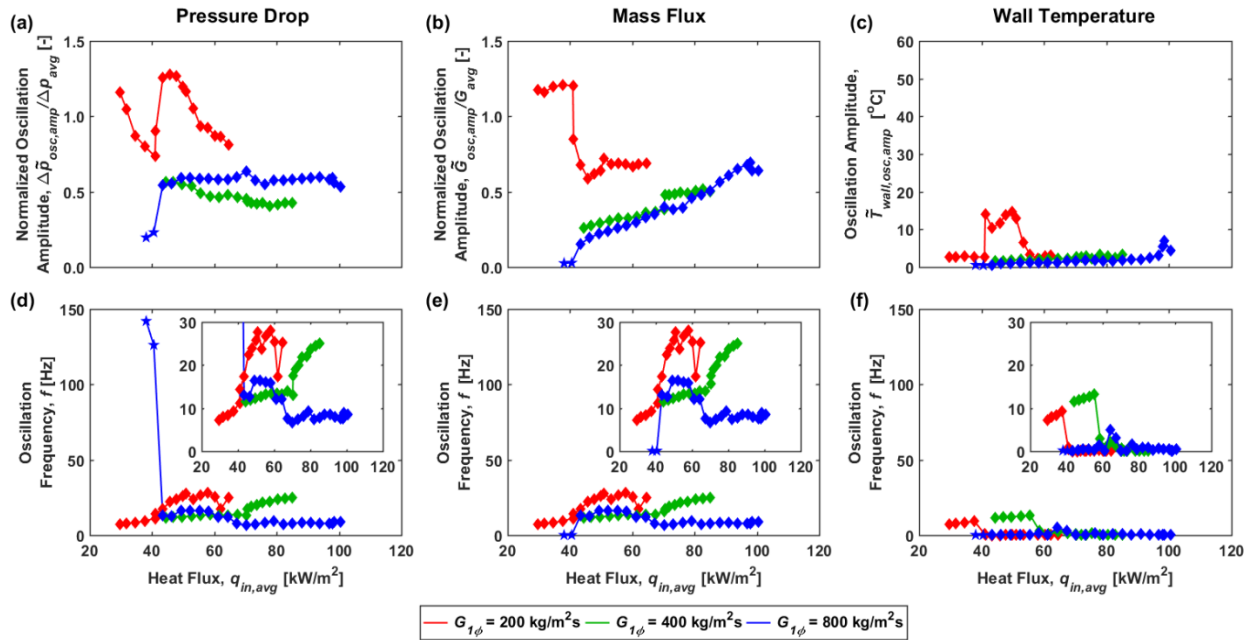
Figure B.1  The (a) normalized pressure drop oscillation amplitude, (b) normalized mass flux oscillation amplitude, (c) thermal oscillation amplitude, and (d-f) characteristic oscillation frequency in the measured signals of pressure drop, mass flux, and wall temperature, are shown as a function of heat flux for $G_{1\phi}$ = 200, 400, and 800 kg/m$^2$s at a fixed $\Delta T_{sub}$ = 5 °C.  Diamond symbols (♦) denote flow-boiling operating conditions where the pressure drop instability was observed.  Star symbols (★) denote flow-boiling operating conditions where the pressure drop instability was suppressed and no other flow instabilities were observed.

# APPENDIX C.    TRANSIENT DATA FOR SELECTED SINGLE HEAT FLUX PULSE CONDITIONS

This section contains transient data for additional single heat flux pulses than those reported in Chapter 6.
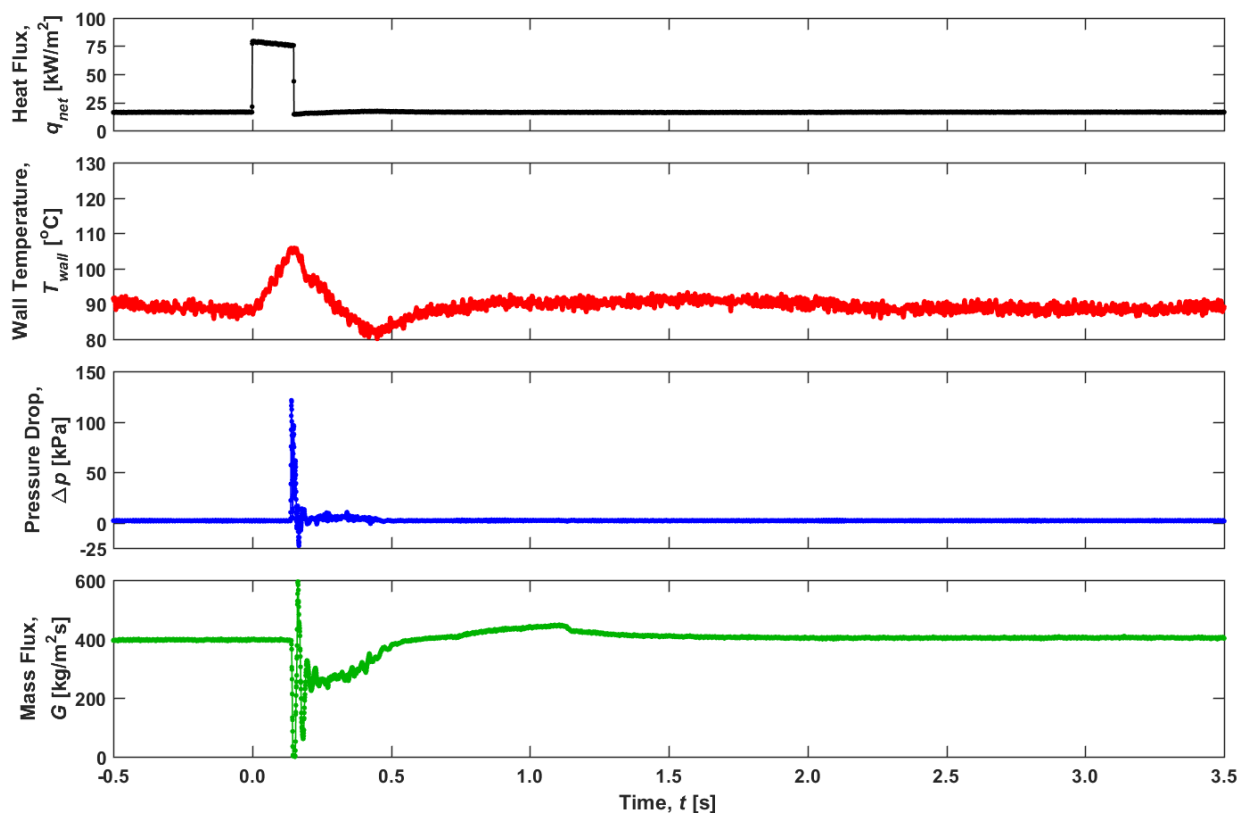


Figure C.1.  Measurements of heat flux, wall temperature, pressure drop, and mass flux as a function of time for -0.5 to 3.5 s relative to the start of a 0.15 s heat flux pulse from 15 to 75 kW/m$^2$ (operating scenario 1).
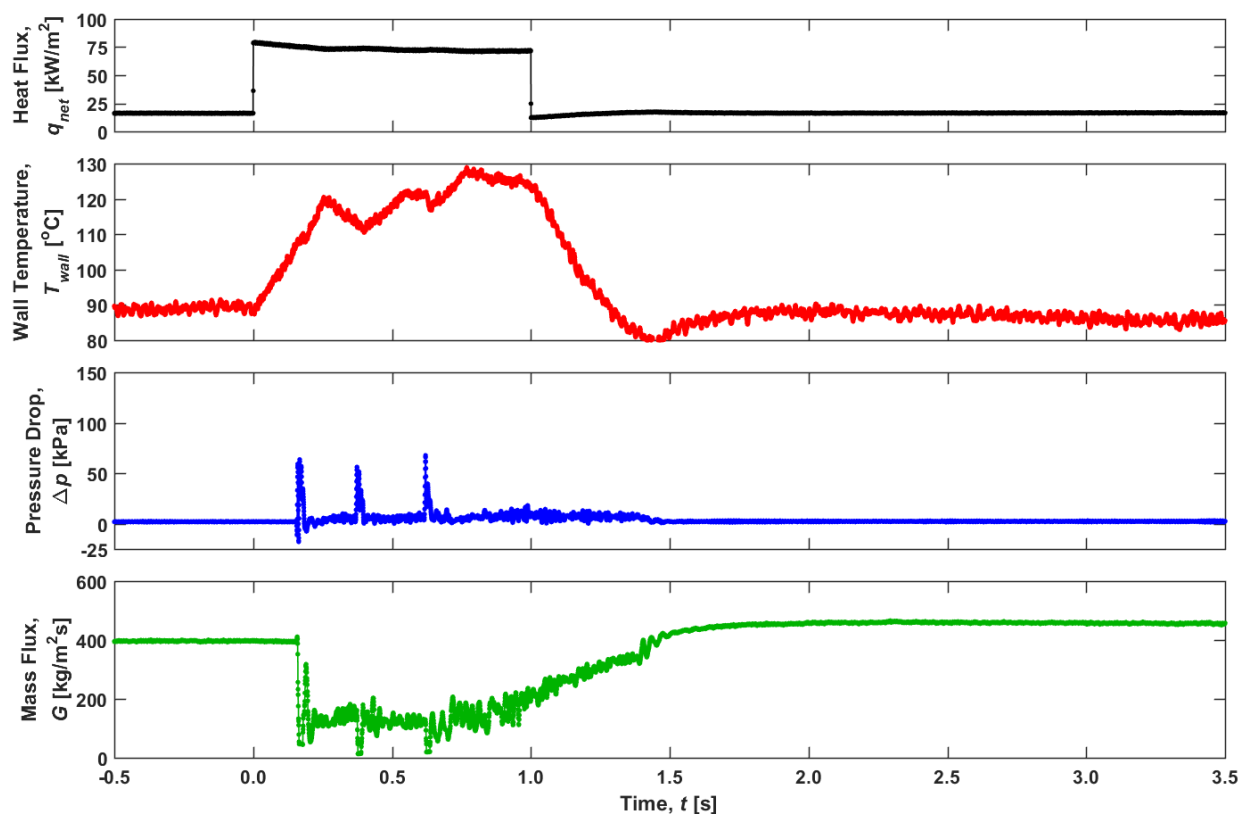
Figure C.2.  Measurements of heat flux, wall temperature, pressure drop, and mass flux as a function of time for -0.5 to 3.5 s relative to the start of a 1 s heat flux pulse from 15 to 75 kW/m$^2$ (operating scenario 1).
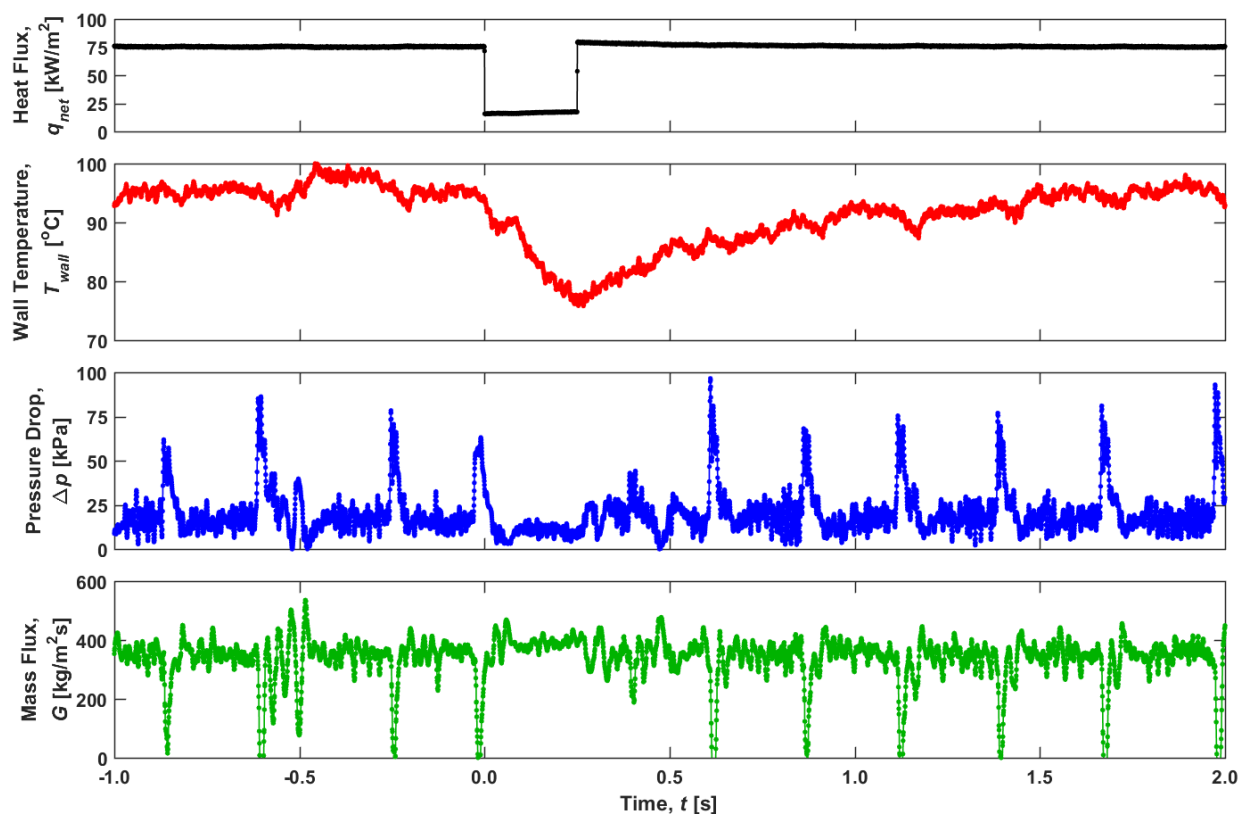
Figure C.3.  Measurements of heat flux, wall temperature, pressure drop, and mass flux as a function of time for -1 to 2 s relative to the start of a 0.25 s heat flux pulse from 75 to 15 kW/m$^2$ (operating scenario 2).
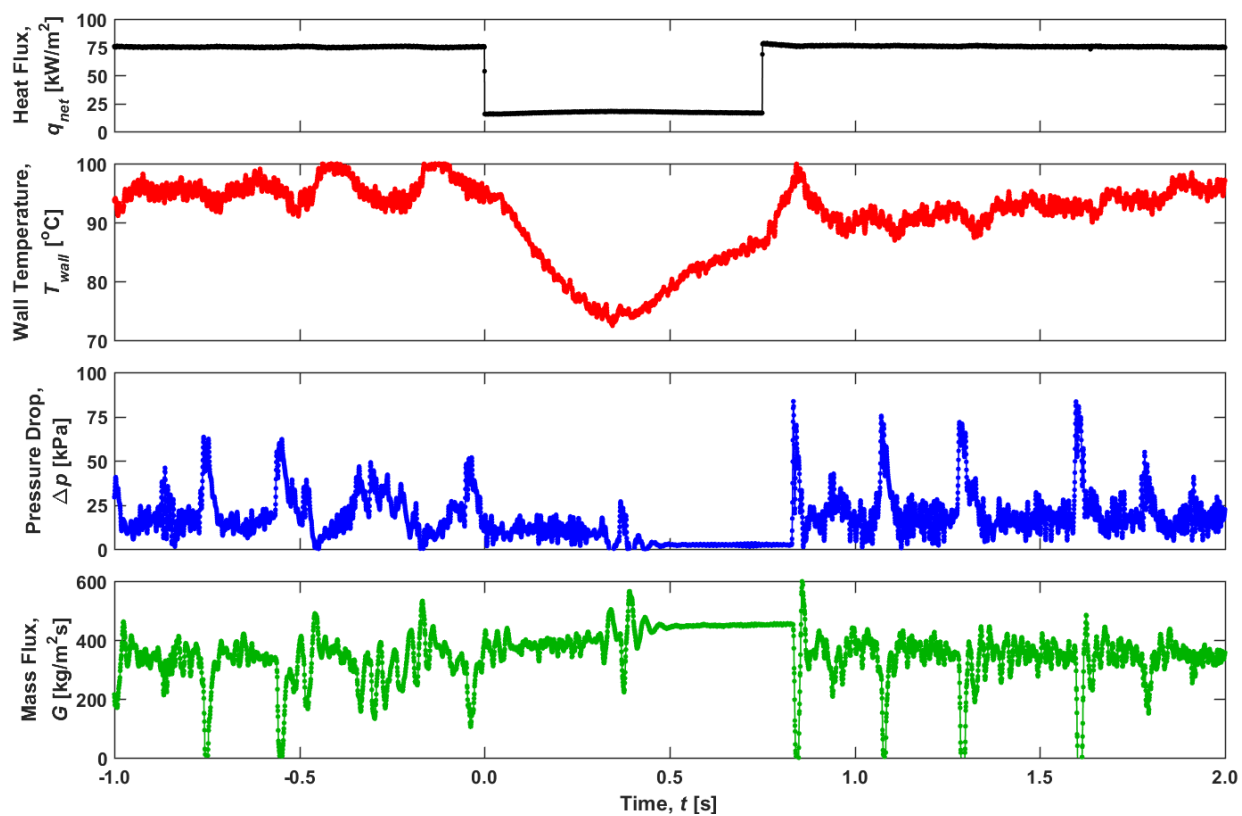
Figure C.4. Measurements of heat flux, wall temperature, pressure drop, and mass flux as a function of time for -1 to 2 s relative to the start of a 0.75 s heat flux pulse from 75 to 15 kW/m$^2$ (operating scenario 2).
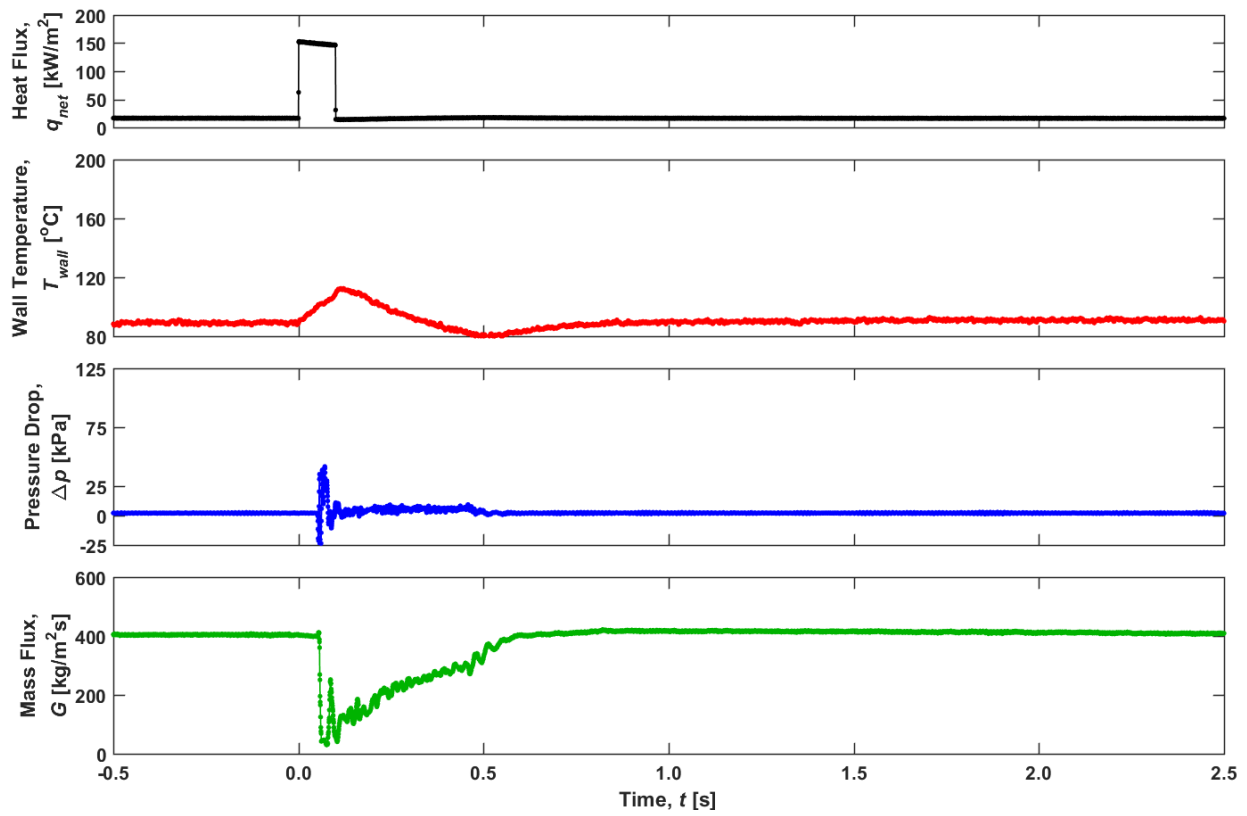
Figure C.5.  Measurements of heat flux, wall temperature, pressure drop, and mass flux as a function of time for -0.5 to 2.5 s relative to the start of a 0.1 s heat flux pulse from 15 to 150 kW/m$^2$ (operating scenario 3).
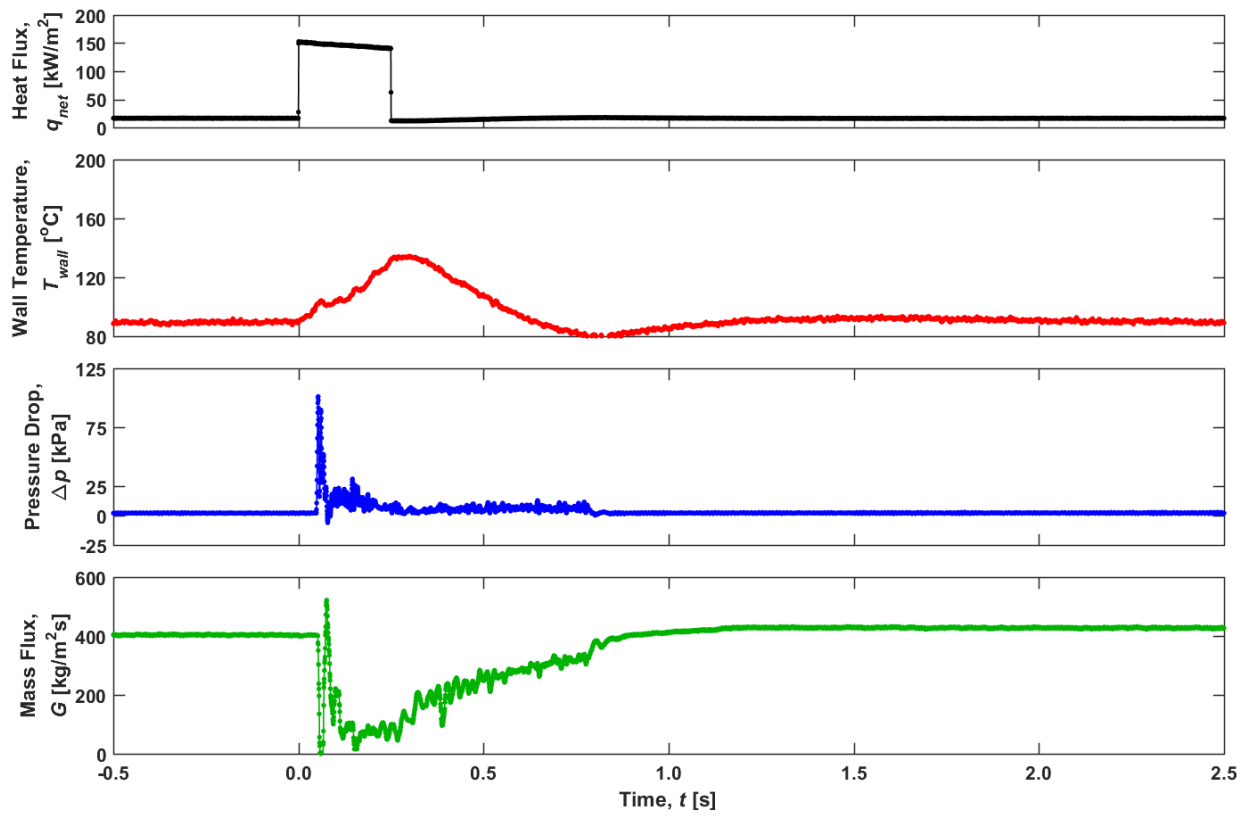
Figure C.6. Measurements of heat flux, wall temperature, pressure drop, and mass flux as a function of time for -0.5 to 2.5 s relative to the start of a 0.25 s heat flux pulse from 15 to 150 kW/m$^2$ (operating scenario 3).
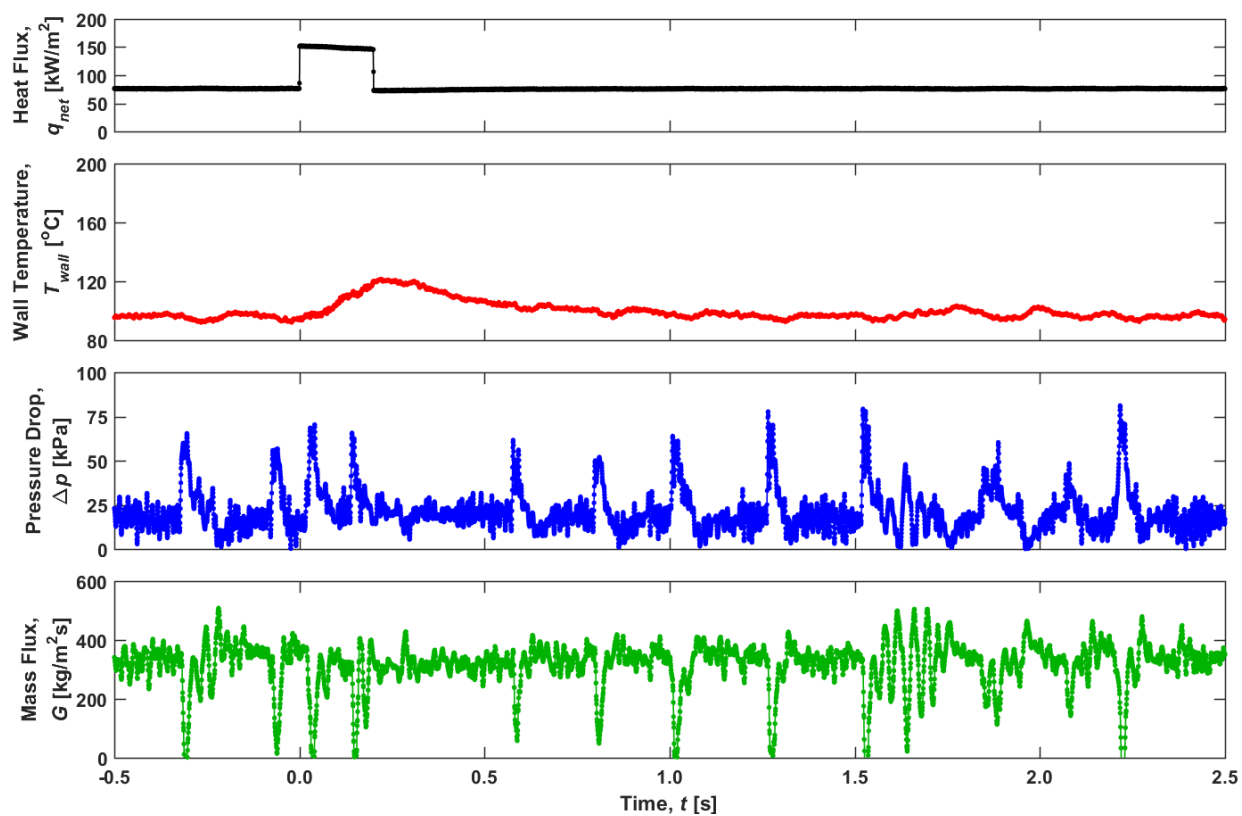
Figure C.7. Measurements of heat flux, wall temperature, pressure drop, and mass flux as a function of time for -0.5 to 2.5 s relative to the start of a 0.2 s heat flux pulse from 75 to 150 kW/m$^2$ (operating scenario 3).
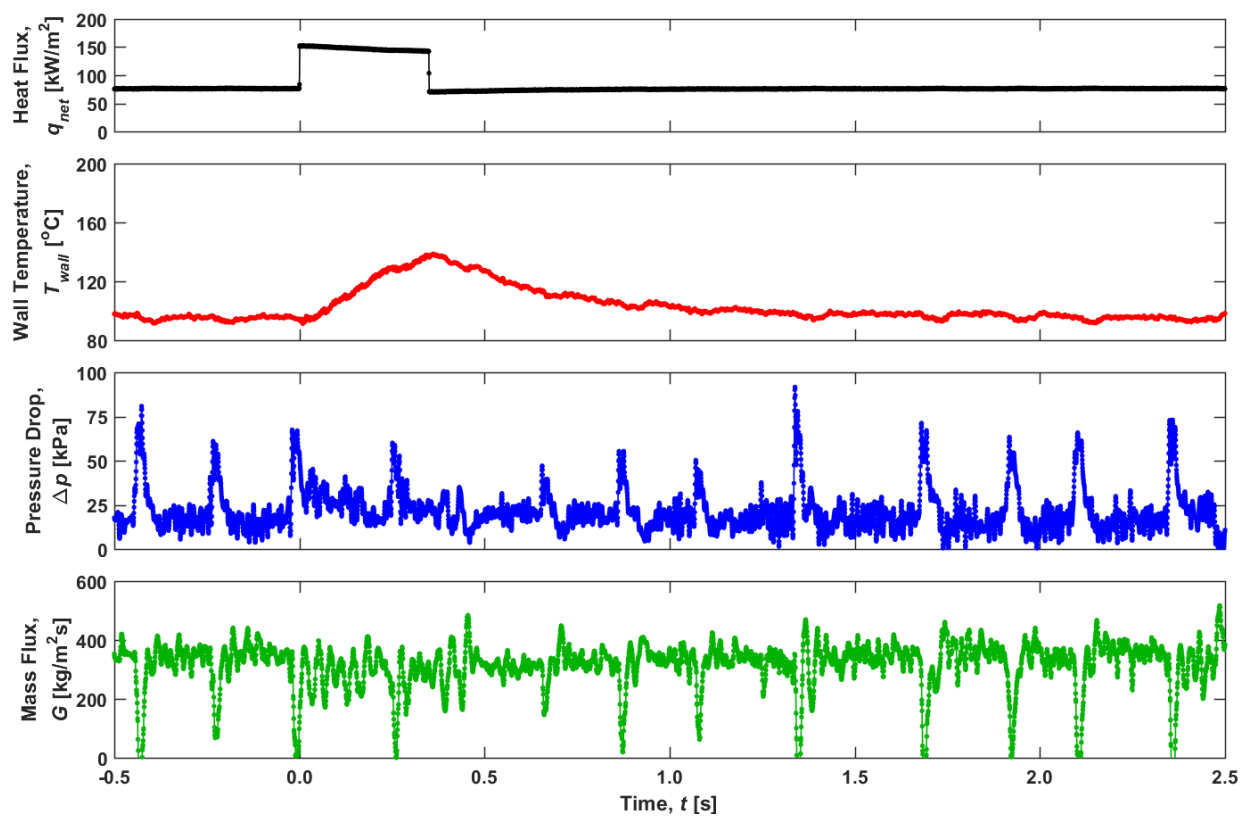
Figure C.8.  Measurements of heat flux, wall temperature, pressure drop, and mass flux as a function of time for -0.5 to 2.5 s relative to the start of a 0.35 s heat flux pulse from 75 to 150 kW/m$^2$ (operating scenario 3).

# APPENDIX D.    MATLAB CODE FOR DIGITAL IMAGE ANALYSIS OF SLUG FLOW BOILING

This section contains the MATLAB code used for qualitative analysis of slug flow boiling images.

```matlab
close all; clear all; clc

addpath(sprintf('%s%s',pwd,'\VEO_images\'));
load('background_image.mat')

LeftEdge = 1;
RightEdge = 1280-0;
TopEdge = 1;
BottomEdge = 32;

outputvideo = VideoWriter('binaryvideo.avi');
outputvideo.FrameRate = 15;
open(outputvideo);

N_rows_subplots = 4;
p=0;
i_initial = 1;
i_final=10;
for i=i_initial:1:i_final
    i
    filename = sprintf('test1_%0.6d.tif',i);
    I1=imread(filename);
    I1_scaled_to_16bit=I1*(2^16/2^12);
    I3=background_image;
    I3_scaled_to_16bit=I3*(2^16/2^12);
    I3 = I3(TopEdge:BottomEdge,LeftEdge:RightEdge);
    I4 = I3-I1;
    I4_scaled_to_16bit=I4*(2^16/2^12);

    grayscalethresholdvalue = 250;
    normalizedthresholdvalue = grayscalethresholdvalue / 2^16;
    I5 = im2bw(I4,normalizedthresholdvalue);
    I5 = bwareaopen(I5, 25, 4);

    [boundaries,L,N,A]= bwboundaries(I5);
    data_frame_centroid=[];
    data_frame_nose=[];
    data_frame_tail=[];
    data_frame_length=[];
    data_frame_sluglength=[];

    for j=1:N
```

```matlab
        b=boundaries{N-j+1};
        bubblenose(j)=max(b(:,2));
        bubbletail(j)=min(b(:,2));
        bubblelength(j)=bubblenose(j)-bubbletail(j);
        bubblecentroid(j)=min(b(:,2))+((max(b(:,2))-min(b(:,2)))/2);
        data_frame_centroid(j)=bubblecentroid(j);
        data_frame_nose(j)=bubblenose(j);
        data_frame_tail(j)=bubbletail(j);
        data_frame_length(j)=bubblelength(j);
    end

    centroid_current=data_frame_centroid(1);
    if i==i_initial
            centroid_previous=centroid_current;
    end

    if abs(centroid_current-centroid_previous)>50
        p=p+1;
    end

    data_centroid(i-i_initial+1,p+1:p+N)=data_frame_centroid;
    data_nose(i-i_initial+1,p+1:p+N)=data_frame_nose;
    data_tail(i-i_initial+1,p+1:p+N)=data_frame_tail;
    data_length(i-i_initial+1,p+1:p+N)=data_frame_length;
    centroid_previous=centroid_current;
    n = 1:N;
    I10=uint8(255*I5);
    D = bwdist(I10);
    writeVideo(outputvideo,I10)
end

n_slugs = size(data_nose,2);
data_slug_length = (data_tail(:,1:n_slugs-1)-
data_nose(:,2:n_slugs)).*sign(data_nose(:,2:n_slugs));
data_slug_head = data_tail(:,1:n_slugs-1).*sign(data_nose(:,2:n_slugs));;
close(outputvideo);

subplot(N_rows_subplots, 1, 1);
imshow(I1_scaled_to_16bit);
subplot(N_rows_subplots, 1, 2);
imshow(I3_scaled_to_16bit);
subplot(N_rows_subplots, 1, 3);
imshow(I4_scaled_to_16bit);
subplot(N_rows_subplots, 1, 4);
imshow(I5);
```

# APPENDIX E.    LIST OF MAJOR COMPONENTS AND EQUIPMENT

This section contains a list of the major components and equipment used in this work.

Table E.1 List of major components and equipment.

| Part | Manufacturer | Part Number |
|---|---|---|
| High-speed camera | Phantom | VEO710L |
| High-speed camera | Phantom | V1212 |
| High-speed camera | Photron | FASTCAM 1024 PCI |
| Low-magnification optical lens | Nikon | AF Micro-Nikkor |
| High-magnification optical lens | Keyence | VH-Z50L |
| High-magnification optical lens | Keyence | VH-Z100R |
| Optical calibration target | Edmund Optics | 59217 |
| Infrared camera | Flir | SC7000 |
| Infrared lens | Janos Technology, Inc. | ASIO 4× |
| 5 VDC power supply | TDK-Lambda Americas, Inc. | LS50-5 |
| 12 VDC power supply | TDK-Lambda Americas, Inc. | LS25-12 |
| 24 VDC power supply | TDK-Lambda Americas, Inc. | LS50-24 |
| 24 VDC power supply | TDK-Lambda Americas, Inc. | LS25-24 |
| Variable power supply | Sorensen | XG 150-5.6 |
| Variable power supply | Sorensen | XG 300-2.8 |
| Variable power supply | Sorensen | DCS80-13E |
| Variable power supply | Electro Industries | 3002A |
| Liquid flow meter | McMillian Co. | 114-6 |
| Liquid flow meter | Alicat | LC-10CCM-D-EPDM |
| Pump | Micromotion | 415A |
| Pump | March Manufacturing Inc. | AC-3C-MD |
| Graham condenser | Ace Glass | 5977-12 |
| Liquid-to-air heat exchanger | Lytron | 4210G10SB-F9 |
| Circulating bath | Thermo Electron Corp. | NESLAB ES 17 |
| Inline carbon filter | Pall Corp. | 12011 |
| Particulate filter | Swagelok | SS-4TF-2 |
| Data acquisition system | National Instruments | USB-6259 |
| Data acquisition system | Agilent | 34970A |
| Pyrometer | Optris | CTfast LT25F |
| Multiplexer | Agilent | 34901A |
| Focusing lens | Optris | ACCTCF |

| Part | Manufacturer | Part Number |
|------|--------------|-------------|
| Pulse generator | Berkeley Nucleonics Corp. | 565 |
| Variac | Starco Energy Products Corp. | 3PN1010B |
| Heating tape | HTS Amptek | AWH051020DLMP |
| Cartridge heater | Watlow | G6A-15568 |
| Working fluid | 3M | HFE-7100 |
| Back-pressure regulator | Equilibar | EB1ULF1-SS316L |
| LED Backlight | Advanced Illumination | BL138 |
| LED Backlight | Advanced Illumination | BL168 |
| Solid state switch | IXYS Corp. | PAA140 |
| Potentiometer | Ohmite | RJS10KE |
| Potentiometer | Ohmite | RHS1K0E |
| Potentiometer | Ohmite | RES100E |
| Shunt Resistor | Empro Shunts | 6142-1-1000 |
| Pressure transducer | Omega | PX309-030G5V |
| Pressure transducer | Omega | PX309-015G5V |
| Pressure transducer | Omega | PX309-030A5V |
| Microchannel | Vitrocom | CV5070 |
| Three-dimensional stage | Thorlabs | T12XYZ |
| One-dimensional stage | Thorlabs | XR25C |
| One-dimensional stage | Thorlabs | XR25P |
| One-dimensional stage | Parker Hannifin | 4410-DM |
| One-dimensional stage | Newport | TSX-1D |
| PEEK T-junction | Valco Instruments | MT1PK |
| PEEK 4-way junction | Valco Instruments | ZX2LPK |
| PTFE ferrule | Professional Plastics, Inc. | TF-16008 |
| PTFE ferrule | Professional Plastics, Inc. | TF-18008 |
| PTFE ferrule | Professional Plastics, Inc. | TF-1828H |
| Needle valve | OMEGA Engineering | FVL-404-SS |
| Needle valve | OMEGA Engineering | FVL-405-SS |
| Metering valve | Swagelok | SS-4BMW |
| Metering valve | Swagelok | SS-SS4-VH |
| Quarter turn valve | Swagelok | SS-42S4 |
| Ice point reference block | Omega | TRCIII |
| Resistance temperature detector | Omega | PR-11-2-100-1/8-12-E |
| Thermocouple | OMEGA Engineering | TMTSS-020E-6 |
| Thermocouple | OMEGA Engineering | TMTSS-062U-6 |
| Optical table | Newport | VIS3672-PG2-325A |

# REFERENCES

[1]   B. Agostini, M. Fabbri, J.E. Park, L. Wojtan, J.R. Thome, B. Michel, State of the art of high heat flux cooling technologies, *Heat Transfer Engineering*, 28(4) (2007) 258-281.

[2]   S.V. Garimella, T. Harirchian, Microchannel heat sinks for electronics cooling, in: A. Bar-Cohen (Ed.), Encyclopedia of thermal packaging - thermal packaging techniques, 2013, World Scientific Publishing Company.

[3]   A. Bar-Cohen, M. Arik, M. Ohadi, Direct liquid cooling of high flux micro and nano electronic components, *Proceedings of the Institute of Electrical and Electronics Engineers*, 94(8) (2006) 1549-1570.

[4]   S.G. Kandlikar, S. Colin, Y. Peles, S. Garimella, R.F. Pease, J.J. Brandner, D.B. Tuckerman, Heat transfer in microchannels - 2012 status and research needs, *Journal of Heat Transfer*, 135(9) (2013) 091001.

[5]   D.B. Tuckerman, R.F.W. Pease, High-performance heat sinking for VLSI, *Electron Device Letters*, 2(5) (1981) 126-129.

[6]   T.L. Bergman, A.S. Lavine, F.P. Incropera, Fundamentals of Heat and Mass Transfer, 7th Edition, John Wiley & Sons, 2011.

[7]   C.T. Crowe, J.D. Schwarzkopf, M. Sommerfeld, Y. Tsuji, Multiphase flows with droplets and particles, Taylor & Francis Group, 2011.

[8]   A.E. Bergles, S.G. Kandlikar, On the nature of critical heat flux in microchannels, *Journal of Heat Transfer*, 127(1) (2005) 101-107.

[9]   J.A. Boure, A.E. Bergles, L.S. Tong, Review of two-phase flow instability, *Nuclear Engineering and Design*, 25(2) (1973) 165-192.

[10] S. Kakac, B. Bon, A review of two-phase flow dynamic instabilities in tube boiling systems, *International Journal of Heat and Mass Transfer*, 51(3-4) (2008) 399-433.

[11] L.C. Ruspini, C.P. Marcel, A. Clausse, Two-phase flow instabilities: A review, *International Journal of Heat and Mass Transfer*, 71 (2014) 521-548.

[12] Y.K. Prajapati, P. Bhandari, Flow boiling instabilities in microchannels and their promising solutions - A review, *Experimental Thermal and Fluid Science*, 88 (2017) 576-593.

[13]  A. Koşar, C.J. Kuo, Y. Peles, Suppression of boiling flow oscillations in parallel microchannels by inlet restrictors, *Journal of Heat Transfer*, 128(3) (2006) 251-260.

[14]  C.J. Kuo, Y. Peles, Flow boiling instabilities in microchannels and means for mitigation by reentrant cavities, *Journal of Heat Transfer*, 130(7) (2008) 072402.

[15]  J. Barber, D. Brutin, K. Sefiane, J.L. Gardarein, L. Tadrist, Unsteady-state fluctuations analysis during bubble growth in a "rectangular" microchannel, *International Journal of Heat and Mass Transfer*, 54(23–24) (2011) 4784-4795.

[16]  T.A. Kingston, J.A. Weibel, S.V. Garimella, High-frequency thermal-fluidic characterization of dynamic microchannel flow boiling instabilities: Part 1 – Rapid-bubble-growth instability at the onset of boiling, *International Journal of Multiphase Flow*, 106 (2018) 179-188.

[17]  W. Qu, I. Mudawar, Measurement and prediction of pressure drop in two-phase micro-channel heat sinks, *International Journal of Heat and Mass Transfer*, 46(15) (2003) 2737-2753.

[18]  T. Van Oevelen, J.A. Weibel, S.V. Garimella, Predicting two-phase flow distribution and stability in systems with many parallel heated channels, *International Journal of Heat and Mass Transfer*, 107 (2017) 557-571.

[19]  K. Akagawa, M. Kono, T. Sakaguchi, M. Nishimura, Study on distribution of flow rates and flow stabilities in parallel long evaporators, *Bulletin of Japan Society of Mechanical Engineers*, 14(74) (1971) 837-848.

[20]  M. Ledinegg, Instability of flow during natural and forced circulation, *Die Warme*, 61(8) (1938) 891-898.

[21]  C.J. Kuo, Y. Peles, Pressure effects on flow boiling instabilities in parallel microchannels, *International Journal of Heat and Mass Transfer*, 52(1–2) (2009) 271-280.

[22]  C. Huh, J. Kim, M.H. Kim, Flow pattern transition instability during flow boiling in a single microchannel, *International Journal of Heat and Mass Transfer*, 50(5–6) (2007) 1049-1060.

[23]  G. Wang, P. Cheng, An experimental study of flow boiling instability in a single microchannel, *International Communications in Heat and Mass Transfer*, 35(10) (2008) 1229-1234.

[24] J. Barber, K. Sefiane, D. Brutin, L. Tadrist, Hydrodynamics and heat transfer during flow boiling instabilities in a single microchannel, *Applied Thermal Engineering*, 29(7) (2009) 1299-1308.

[25] T. Harirchian, S.V. Garimella, Microchannel size effects on local flow boiling heat transfer to a dielectric fluid, *International Journal of Heat and Mass Transfer*, 51(15-16) (2008) 3724-3735.

[26] T. Harirchian, S.V. Garimella, A comprehensive flow regime map for microchannel flow boiling with quantitative transition criteria, *International Journal of Heat and Mass Transfer*, 53(13-14) (2010) 2694-2702.

[27] T. Harirchian, S.V. Garimella, Flow regime-based modeling of heat transfer and pressure drop in microchannel flow boiling, *International Journal of Heat and Mass Transfer*, 55(4) (2012) 1246-1260.

[28] T. Harirchian, S.V. Garimella, Effects of channel dimension, heat flux, and mass flux on flow boiling regimes in microchannels, *International Journal of Multiphase Flow*, 35(4) (2009) 349-362.

[29] T. Harirchian, S.V. Garimella, The critical role of channel cross-sectional area in microchannel flow boiling heat transfer, *International Journal of Multiphase Flow*, 35(10) (2009) 904-913.

[30] J.R. Thome, V. Dupont, A.M. Jacobi, Heat transfer model for evaporation in microchannels. Part I: Presentation of the model, *International Journal of Heat and Mass Transfer*, 47 (2004) 3375-3385.

[31] W.L. Qu, I. Mudawar, Flow boiling heat transfer in two-phase micro-channel heat sinks - II. Annular two-phase flow model, *International Journal of Heat and Mass Transfer*, 46(15) (2003) 2773-2784.

[32] S. Jesseela, C.B. Sobhan, Numerical modeling of annular flow with phase change in a microchannel, *International Journal of Thermal Sciences*, 89 (2015) 87-99.

[33] R.S. Patel, J.A. Weibel, S.V. Garimella, Mechanistic modeling of the liquid film shape and heat transfer coefficient in annular-regime microchannel flow boiling, *International Journal of Heat and Mass Transfer*, 114 (2017) 841-851.

[34] Y.P. Peles, L.P. Yarin, G. Hetsroni, Steady and unsteady flow in a heated capillary, *International Journal of Multiphase Flow*, 27(4) (2001) 577-598.

[35] A.M. Jacobi, J.R. Thome, Heat transfer model for evaporation of elongated bubble flows in microchannels, *Journal of Heat Transfer*, 124(6) (2002) 1131-1136.

[36] G. Wang, L. Hao, P. Cheng, A four-zone model for saturated flow boiling in a microchannel of rectangular cross-section, *International Journal of Heat and Mass Transfer*, 53 (2010) 3439-3448.

[37] A. Esmaeeli, G. Tryggvason, Computations of film boiling. Part I: Numerical method, *International Journal of Heat and Mass Transfer*, 47(25) (2004) 5451-5461.

[38] D. Sun, J. Xu, Q. Chen, Modeling of the evaporation and condensation phase-change problems with FLUENT, *Numerical Heat Transfer, Part B: Fundamentals*, 66(4) (2014) 326-342.

[39] M. Magnini, B. Pulvirenti, J.R. Thome, Numerical investigation of hydrodynamics and heat transfer of elongated bubbles during flow boiling in a microchannel, *International Journal of Heat and Mass Transfer*, 59 (2013) 451-471.

[40] Z. Pan, J.A. Weibel, S.V. Garimella, A saturated-interface-volume phase change model for simulating flow boiling, *International Journal of Heat and Mass Transfer*, 93 (2016) 945-956.

[41] Y. Tsui, S. Lin, Y. Lai, F. Wu, Phase change calculations for film boiling flows, *International Journal of Heat and Mass Transfer*, 70 (2014) 745-757.

[42] Z. Pan, J.A. Weibel, S.V. Garimella, Spurious current suppression in VOF-CSF simulation of slug flow through small channels, *Numerical Heat Transfer, Part A: Applications*, 67(1) (2015) 1-12.

[43] M. Magnini, B. Pulvirenti, J.R. Thome, Numerical investigation of the influence of leading and sequential bubbles on slug flow boiling within a microchannel, *International Journal of Thermal Sciences*, 71 (2013) 36-52.

[44] M. Magnini, J.R. Thome, Computational study of saturated flow boiling within a microchannel in the slug flow regime, *Journal of Heat Transfer*, 138(2) (2015) 021502.

[45] C. Kunkelmann, P. Stephan, CFD simulation of boiling flows using the volume-of-fluid method within OpenFOAM, *Numerical Heat Transfer, Part A: Applications*, 56(8) (2009) 631-646.

[46] S. Hardt, F. Wondra, Evaporation model for interfacial flows based on a continuum-field representation of the source terms, *Journal of Computational Physics*, 227(11) (2008) 5871-5895.

[47] S. Bigham, S. Moghaddam, Microscale study of mechanisms of heat transfer during flow boiling in a microchannel, *International Journal of Heat and Mass Transfer*, 88 (2015) 111-121.

[48] A. Scammell, J. Kim, Heat transfer and flow characteristics of rising Taylor bubbles, *International Journal of Heat and Mass Transfer*, 89 (2015) 379-389.

[49] S.R. Rao, F. Houshmand, Y. Peles, Transient flow boiling heat-transfer measurements in microdomains, *International Journal of Heat and Mass Transfer*, 76 (2014) 317-329.

[50] Y. Zhu, D.S. Antao, D.W. Bian, S.R. Rao, J.D. Sircar, T. Zhang, E.N. Wang, Suppressing high-frequency temperature oscillations in microchannels with surface structures, *Applied Physics Letters*, 110(3) (2017) 033501.

[51] T. David, D. Mendler, A. Mosyak, A. Bar-Cohen, G. Hetsroni, Thermal management of time-varying high heat flux electronic devices, *Journal of Electronic Packaging*, 136(2) (2014) 021003.

[52] C.G. Tua, T. Pratt, A.I. Zaghloul, A study of interpulse instability in gallium nitride power amplifiers in multifunction radars, *IEEE Transactions on Microwave Theory and Techniques*, 64(11) (2016) 3732-3747.

[53] A. Bar-Cohen, Gen-3 thermal management technology: role of microchannels and nanostructures in an embedded cooling paradigm, *Journal of Nanotechnology in Engineering and Medicine*, 4(2) (2013) 020907.

[54] L.J. Guo, Z.P. Feng, X.J. Chen, Transient convective heat transfer of steam-water two-phase flow in a helical tube under pressure drop type oscillations, *International Journal of Heat and Mass Transfer*, 45(3) (2002) 533-542.

[55] I.W. Park, J. Ryu, M. Fernandino, C.A. Dorao, Can flow oscillations during flow boiling deteriorate the heat transfer coefficient?, *Applied Physics Letters*, 113(15) (2018).

[56] M. Sorum, C.A. Dorao, Experimental study of the heat transfer coefficient deterioration during density wave oscillations, *Chemical Engineering Science*, 132 (2015) 194-201.

[57] M. Ozawa, H. Umekawa, K. Mishima, T. Hibiki, Y. Saito, CHF in oscillatory flow boiling channels, *Chemical Engineering Research and Design*, 79(A4) (2001) 389-401.

[58] S. Basu, B. Werneke, Y. Peles, M.K. Jensen, Transient microscale flow boiling heat transfer characteristics of HFE-7000, *International Journal of Heat and Mass Transfer*, 90 (2015) 396-405.

[59] H. Huang, N. Borhani, J. Thome, Thermal response of multi-microchannel evaporators during flow boiling of refrigerants under transient heat loads with flow visualization, *Journal of Electronic Packaging*, 138(3) (2016) 031004.

[60] G. Chen, P. Cheng, Nucleate and film boiling on a microheater under pulse heating in a microchannel, *International Communications in Heat and Mass Transfer*, 36(5) (2009) 391-396.

[61] J.L. Miler, R. Flynn, G. Refai-Ahmed, M. Touzelbaev, M. David, J. Steinbrenner, K.E. Goodson, Effects of transient heating on two-phase flow response in microchannel heat exchangers, *Proceedings of ASME InterPACK*, 2 (2010) 563-569.

[62] G.M. Aguiar, G. Ribatski, The effect of transient power hotspots on the heat transfer coefficient during flow boiling inside single microscale channels, *Heat Transfer Engineering*, (2018) 1-12.

[63] 3M, 3M Novec Engineered Fluid HFE-7100 for Heat Transfer, in, 3M, St. Paul, MN, 2002, pp. 1-8.

[64] T.A. Kingston, J.A. Weibel, S.V. Garimella, High-frequency thermal-fluidic characterization of dynamic microchannel flow boiling instabilities: Part 2 – Impact of operating conditions on instability type and severity, *International Journal of Multiphase Flow*, 106 (2018) 189-201.

[65] W. Qu, I. Mudawar, Flow boiling heat transfer in two-phase micro-channel heat sinks - I. Experimental investigation and assessment of correlation methods, *International Journal of Heat and Mass Transfer*, 46(15) (2003) 2755-2771.

[66] T.A. Kingston, J.A. Weibel, S.V. Garimella, Ledinegg instability-induced temperature excursion between thermally isolated, heated parallel microchannels, *International Journal of Heat and Mass Transfer*, 132 (2019) 550-556.

[67] R. Flynn, C.-H. Cheng, K. Goodson, Decoupled thermal and fluidic effects on hotspot cooling in a boiling flow microchannel heat sink, in: Proceedings of ASME InterPACK, Vancouver, British Columbia, Canada, 2007, pp. 179-184.

[68] K.P. Drummond, D. Back, M.D. Sinanis, D.B. Janes, D. Peroulis, J.A. Weibel, S.V. Garimella, A hierarchical manifold microchannel heat sink array for high-heat-flux two-phase cooling of electronics, *International Journal of Heat and Mass Transfer*, 117 (2018) 319-330.

[69]  K.P. Drummond, D. Back, M.D. Sinanis, D.B. Janes, D. Peroulis, J.A. Weibel, S.V. Garimella, Characterization of hierarchical manifold microchannel heat sink arrays under simultaneous background and hotspot heating conditions, *International Journal of Heat and Mass Transfer*, 126 (2018) 1289-1301.

[70]  T.A. Kingston, J.A. Weibel, S.V. Garimella, Time-resolved characterization of microchannel flow boiling during transient heating: Part 1 - Dynamic response to a single heat flux pulse, (2019) (in preparation).

[71]  K. Miyabayashi, O. Tonomura, S. Hasebe, Estimation of gas and liquid slug lengths for T-shaped microreactors, *Chemical Engineering Journal*, 262 (2015) 1137-1143.

[72]  R. Gupta, D. Fletcher, B. Haynes, Taylor flow in microchannels: A review of experimental and computational work, *The Journal of Computational Multiphase Flows*, 2(1) (2010) 1-32.

[73]  C.B. Tibiriçá, F.J. do Nascimento, G. Ribatski, Film thickness measurement techniques applied to micro-scale two-phase flow systems, *Experimental Thermal and Fluid Science*, 34(4) (2010) 463-473.

[74]  Y. Han, N. Shikazono, Measurement of liquid film thickness in micro square channel, *International Journal of Multiphase Flow*, 35(10) (2009) 896-903.

[75]  Y. Han, N. Shikazono, Measurement of the liquid film thickness in micro tube slug flow, *International Journal of Heat and Fluid Flow*, 30(5) (2009) 842-853.

[76]  R.S. Patel, J.A. Weibel, S.V. Garimella, An optical approach for quantitative characterization of slug bubble interface profiles in a two-phase microchannel flow, *International Journal of Heat and Mass Transfer*, 86 (2015) 31-38.

[77]  K.K. Brown, H.W. Coleman, W.G. Steele, A methodology for determining experimental uncertainties in regressions, *Journal of Fluids Engineering*, 120(3) (1998) 445-456.

# VITA

Todd A. Kingston was born in Fremont, Nebraska in 1988. He received a Bachelor of Science in 2011 and a Master of Science in 2013, both in Mechanical Engineering from Iowa State University. His master's research investigated granular mixing visualization and quantification in a double screw mixer and was conducted under the advisement of Prof. Theodore J. Heindel. Todd joined the School of Mechanical Engineering at Purdue University to pursue a Doctor of Philosophy in Mechanical Engineering in 2014. Todd's doctoral research was conducted in the Cooling Technologies Research Center (CTRC) under the advisement of Prof. Suresh V. Garimella and Prof. Justin A. Weibel. Todd collaborated with the Naval Surface Warfare Center Crane Division (NSWC Crane) in Crane, Indiana for part of his doctoral research. Todd was also a Pathways Program Intern at NSWC Crane in the summer of 2017, where he worked in the Solid State and Power Engineering Branch within the Radar Technologies Division under the advisement of Dr. Brian D. Olson and Mr. Charles Walker.

Todd was awarded the National Research Council Postdoctoral Fellowship in 2019 to conduct research at the Naval Research Laboratory in Washington D.C. for one year beginning in June 2019. After which, Todd will be joining the Department of Mechanical Engineering at Iowa State University as a tenure-track Assistant Professor in August 2020. Todd's primary research interests are in energy transport and conversion processes, specifically those involving multiphase flow and heat transfer phenomena.

Todd has received several honors from Purdue University, including the School of Mechanical Engineering Outstanding Research Award in 2019 and the Laura Winkelman Davidson Fellowship in 2014. Todd was the recipient of the 2018 ASNE Tidewater Section James Pitt Scholarship, 2018 AOC Crane Roost Chapter Scholarship, ASHRAE Iowa Chapter Student Scholarship in 2011, 2012, and 2013, and Iowa State University's Roderick Seward, Flossie Ratcliffe, and Helen M. Galloway Foundation Scholarship in 2011. Todd has also received several awards from professional conferences including the IEEE ITherm Outstanding Student Poster Award in 2017, ASME InterPACK/ICNMM Graduate Student Best Poster Award in 2015, and the ASME FEDSM Graduate Student Paper Competition Award in 2013. Todd was inducted into Tau Beta Pi in 2010 and Pi Tau Sigma in 2009.

# PUBLICATIONS

## Journal Papers

1. Kingston, T.A., Weibel, J.A., and Garimella, S.V. (2019) Ledinegg Instability-Induced Temperature Excursion Between Thermally Isolated, Heated Parallel Microchannels. *International Journal of Heat and Mass Transfer,* 132, pp. 550-556 (doi.org/10.1016/j.ijheatmasstransfer.2018.12.017).

2. Kingston, T.A., Weibel, J.A., and Garimella, S.V. (2018) High-Frequency Thermal-Fluidic Characterization of Dynamic Microchannel Flow Boiling Instabilities: Part 2 – Impact of Operating Conditions on Instability Type and Severity, *International Journal of Multiphase Flow,* 106, pp. 189-201 (doi.org/10.1016/j.ijmultiphaseflow.2018.05.001).

3. Kingston, T.A., Weibel, J.A., and Garimella, S.V. (2018) High-Frequency Thermal-Fluidic Characterization of Dynamic Microchannel Flow Boiling Instabilities: Part 1 - Rapid-Bubble-Growth Instability at the Onset of Boiling, *International Journal of Multiphase Flow,* 106, pp. 179-188 (doi.org/10.1016/j.ijmultiphaseflow.2018.05.007).

4. Kingston, T.A., Weibel, J.A., and Garimella, S.V. (2017) An experimental method for controlled generation and characterization of microchannel slug flow boiling, *International Journal of Heat and Mass Transfer,* 106, pp. 619-628 (doi.org/10.1016/j.ijheatmasstransfer.2016.09.036).

5. Kingston, T.A., Geick, T.A., Robinson, T.R., and Heindel, T.J. (2015). Characterizing 3D granular flow structures in a double screw mixer using X-ray particle tracking velocimetry, *Powder Technology*, 278, pp. 211-222 (doi.org/10.1016/j.powtec.2015.02.061).

6. Kingston, T.A., Morgan. T.B., Geick, T.A., Robinson, T.R., and Heindel, T.J. (2014) A cone-beam compensated back-projection algorithm for X-ray particle tracking velocimetry, *Flow Measurement and Instrumentation*, 39, pp. 64-75 (doi.org/10.1016/j.flowmeasinst.2014.06.002).

7. Kingston, T.A. and Heindel, T.J. (2014). Granular mixing optimization and the influence of operating conditions in a double screw mixer. *Powder Technology*, 266, pp.144-155 (doi.org/10.1016/j.powtec.2014.06.016).

8. Kingston, T.A. and Heindel, T.J. (2014). Optical visualization and composition analysis to quantify continuous granular mixing processes, *Powder Technology*, 262, pp. 257-264 (doi.org/10.1016/j.powtec.2014.04.071).

**Conference Papers**

1. Kingston, T.A., Moskalenko, A.E., Weibel, J.A., and Garimella, S.V. (2017). Rapid-bubble-growth instability at the onset of microchannel flow boiling. IEEE ITherm, Lake Buena Vista, Florida (doi.org/10.1109/ITHERM.2017.7992471).

2. Kingston, T.A., Weibel, J.A., and Garimella, S.V. (2015). Quantitative visualization of vapor bubble growth in diabatic vapor-liquid microchannel slug flow. ASME InterPACK, San Francisco, California (doi.org/10.1115/IPACK2015-48177).

3. Kingston, T.A. and Heindel, T.J. (2014). Characterizing granular mixing homogeneity at various dimensionless mixing lengths in a double screw mixer. ASME 2014 FEDSM, Chicago, Illinois (doi.org/10.1115/FEDSM2014-21048).

4. Kingston, T.A. and Heindel, T.J. (2013). Visualization and composition analysis to quantify mixing in a screw pyrolyzer. ASME FEDSM, Incline Village, Nevada (doi.org/10.1115/FEDSM2013-16054).